AUGMENTATION OF POWER CONVERSION EFFICIENCY OF PHOTOVOLTAIC CELL UTILIZING POLY(METHYL METHACRYLATE-*CO*-ACRYLIC ACID) NANOSPHERES ENCAPSULATED WITH SILVER OR GOLD NANOPARTICLES

GOH WEE SHENG

MASTER OF SCIENCE

FACULTY OF SCIENCE
UNIVERSITI TUNKU ABDUL RAHMAN
JANUARY 2019

AUGMENTATION OF POWER CONVERSION EFFICIENCY OF SILICON PHOTOVOLTAIC CELL UTILIZING POLY(METHYL METHACRYLATE-*CO*-ACRYLIC ACID) NANOSPHERES ENCAPSULATED WITH SILVER OR GOLD NANOPARTICLES

By

GOH WEE SHENG

A dissertation submitted to the Department of Chemical Science,
Faculty of Science,
Universiti Tunku Abdul Rahman,
in partial fulfillment of the requirements for the degree of
Master of Science
January 2019

ABSTRACT

AUGMENTATION OF POWER CONVERSION EFFICIENCY OF SILICON PHOTOVOLTAIC CELL UTILIZING POLY(METHYL METHACRYLATE-*CO*-ACRYLIC ACID) NANOSPHERES ENCAPSULATED WITH SILVER OR GOLD NANOPARTICLES

GOH WEE SHENG

Silicon solar cell is a promising candidate for the mass implementation of photovoltaic cell due to its well-developed fabrication processes, and the abundant availability as well as the non-toxicity nature of the raw material. Nevertheless, the high refractive index of silicon results in reflection losses of incident sunlight. Hence, efficient light trapping schemes must be implemented to suppress the optical losses. In this study, we demonstrate a novel approach by utilizing self-assembled poly(methyl methacrylate-*co*-acrylic acid), P(MMA-*co*-AA), polymer nanosphere arrays in addition to the incorporation of gold or silver nanoparticles as a light trapping layer to enhance the power conversion efficiency of the solar cells. The P(MMA-*co*-AA) nanospheres with diameters ranging between 100-160 nm were synthesized via emulsion polymerization. The particle size of the P(MMA-*co*-AA) nanospheres were determined by laser diffraction technique. The P(MMA-*co*-AA) nanospheres were characterized using infrared spectroscopy and exhaustive thermal analyses, namely differential scanning calorimetry and thermogravimetric analysis. The P(MMA-*co*-AA) copolymer exhibits a relatively high glass transition temperature which is in the range of 110-115°C and it has the main decomposition temperature at 395°C. The presence of the metallic nanoparticles

in the polymer nanospheres was confirmed through transmission electron microscopy and energy dispersive X-ray technique. The surface morphology and topology of the arrays of polymer nanospheres on silicon substrates were characterized via field emission scanning electron microscopy and atomic force microscopy. By introducing the polymer nanospheres with an average diameter of 101 nm on silicon solar cells, a relative enhancement of 57% was observed under a AM 1.5 solar simulator, as compared to the bare solar cell with the efficiency of 2%. By incorporating gold nanoparticles (i.e. 3.75×10^{-3} wt%) and silver nanoparticles (i.e. 2.5×10^{-3} wt%) into the polymer nanospheres, the solar cells show further enhancement of 166% and 179% respectively.

ACKNOWLEDGEMENT

This research is not individual achievement instead is the results of help and support from many people all of this while. I would like to express sincere gratitude and appreciation to my supervisors Assistant Professor Dr Chee Swee Yong and Ms Yik Lai Kuan as well as my external co-supervisor Associate Professor Dr Lee Chee Leong for their encouraging and giving me invaluable advice throughout the period of completion on this project. They are also willing to sacrifice their precious time to provide teaching and guidance which I valued greatly.

Other than that, I would like to thank my university, Universiti Tunku Abdul Rahman (UTAR), for the good environment and facilities as well as the research funding (UTARRF Grant No. IPSR/RMC/UTARRF/2014-C1/L03) to complete this project. I am grateful to all the laboratory officers in UTAR for their cooperation and help throughout the project. Moreover, I am grateful to Wawasan Open University [IRI Grant No. WOU/IRI/2016(0016)] for the research funding. I would also like to express my gratitude to Mr Mohd Norizam Md Daud from Universiti Kebangsaan Malaysia for the use of the equipment in Advanced Silicon Solar Cells Laboratory.

I am thankful to my course mates and seniors for providing support, guidance and encouragement. They are willing to help when the need arises. Finally yet importantly, an honourable mention goes to my family and friends for their understanding, support and constant encouragement in completing the project.

APPROVAL SHEET

This dissertation/thesis entitled "**AUGMENTATION OF POWER CONVERSION EFFICIENCY OF SILICON PHOTOVOLTAIC CELL UTILIZING POLY(METHYL METHACRYLATE-*CO*-ACRYLIC ACID) NANOSPHERES ENCAPSULATED WITH SILVER OR GOLD NANOPARTICLES"** was prepared by GOH WEE SHENG and submitted as partial fulfillment of the requirements for the degree of Master of Science at Universiti Tunku Abdul Rahman.

Approved by:

_____
(Asst. Prof. Dr CHEE SWEE YONG)
Date:……..
Assistant Professor/Supervisor
Department of Chemical Science
Faculty of Science
Universiti Tunku Abdul Rahman

_____
(Ms YIK LAI KUAN)
Date:……..
Co-supervisor
Department of Physical and Mathematical Science
Faculty of Science
Universiti Tunku Abdul Rahman

FACULTY OF SCIENCE

UNIVERSITI TUNKU ABDUL RAHMAN

Date: 2 January 2019

SUBMISSION OF DISSERTATION

It is hereby certified that ***Goh Wee Sheng*** (ID No: ***1407969***) has completed this dissertation entitled "*Augmentation of Power Conversion Efficiency of Silicon Photovoltaic Cell Utilizing Poly(Methyl Methacrylate-co-Acrylic Acid) Nanospheres Encapsulated with Silver or Gold Nanoparticles*" under the supervision of Dr Chee Swee Yong (Supervisor) from the Department of Chemical Science, Faculty of Science , and Ms Yik Lai Kuan (Co-Supervisor) from the Department of Physical and Mathematical Science, Faculty of Science.

I understand that University will upload softcopy of dissertation in pdf format into UTAR Institutional Repository, which may be made accessible to UTAR community and public.

Yours truly,

_____

(*Goh Wee Sheng*)

DECLARATION

I hereby declare that the dissertation is based on my original work except for quotations and citations which have been duly acknowledged. I also declare that it has not been previously or concurrently submitted for any other degree at UTAR or other institutions.

Name _____

Date _____

TABLE OF CONTENTS

LIST OF TABLES

LIST OF FIGURES

LIST OF ABBREVIATIONS

Air Mass 1.5	AM 1.5
Atomic Force Microscope	AFM
Amorphous silicon	*a*-Si
Anti-Reflective Coating	ARC
Cadmium Sulfide	CdS
Cadmium Telluride	CdTe
Copper Indium Gallium Selenide	CIGS
Crystalline Silicon	*c*-Si
Current-Voltage	*I-V*
Current Density-Voltage	*J-V*
Decomposition Temperature	T_d
Differential Scanning Calorimetry	DSC
Differential Thermogravimetry	DTG
Dye Sensitized Solar Cell	DSSC
Energy Dispersive X-ray	EDX
Field Emission Scanning Electron Microscope	FESEM
Fill Factor	*FF*
Fourier Transform Infrared	FTIR
Gallium Arsenide	GaAs
Glass Transition Temperature	T_g
Gold	Au
Gold Nanoparticles	AuNPs
Hydrogenated Amorphous Silicon	*a*-Si:H
Indium Tin Oxide	ITO

Localized Surface Plasmon Resonance	LSPR
Nanospheres	NSs
One-Dimensional	1-D
Open Circuit Voltage	V_{OC}
Poly(3,4-Ethylenedioxythiophene): Polystyrenesulfonate	PEDOT:PSS
Poly(Methyl Methacrylate)	PMMA
Poly(Methyl-Methacrylate-*co*-Acrylic Acid)	P(MMA-*co*AA)
Polystyrene	PS
Potassium Bromide	KBr
Power Conversion Efficiency	PCE
Silica	SiO_2
Silicon	Si
Silver	Ag
Silver Nanoparticles	AgNPs
Short Circuit Current	I_{SC}
Short Circuit Current Density	J_{SC}
Sodium Dodecyl Sulfate	SDS
Transmission Electron Microscope	TEM
Thermogravimetric Analysis	TGA
Three-Dimensional	3-D
Titanium Dioxide	TiO_2
Transparent Conductive Oxide	TCO
Two-Dimensional	2-D
Ultraviolet-Visible	UV-Vis

X-Ray Diffraction	XRD
Zinc Oxide	ZnO
Zinc Selenide	ZnSe

CHAPTER 1

INTRODUCTION

1.1 Problem Statement

Solar energy has emerged as one of the most popular candidates to replace fossil fuel due to the unique properties such as clean and sustainable energy resources. In contrast to other energy resources like, hydroelectric power, biofuel, wind and geothermal energy, solar energy has been drawn widespread attention due to its abundance, stability and environmental friendliness. Solar energy can be converted to electrical energy through the photovoltaic effect of solar cell. (Gjessing, 2011) In the last few years, the usage of solar energy as a renewable energy resource has increased intensely compared to the conventional fossil fuels.

Among the materials used for photovoltaic applications, silicon is the most widely used material due to its abundance on earth, nontoxicity to the environment, and well-established fabrication processes (Pillai, et al., 2007). Hence, silicon photovoltaic cells have contributed more than 70% of the solar panels in the global market nowadays (Lin, et al., 2014). Although silicon solar cells are the most widely used, the high refractive index of silicon (n = 3.8) causes almost 40% of the incident light being wasted through surface reflection without absorbed by the solar cells (Fang, et al., 2013). Therefore, less light is absorbed and converted to photocurrent, and finally resulting in low efficiency of silicon solar cells. The photocurrent is also known as the light-generated

current, which is proportional to the amount of light absorbed by the solar cell. Based on the intrinsic properties of silicon, the theoretical limit of power conversion efficiency is 29% at air mass 1.5 (AM 1.5) irradiation (Haugan, 2011). Furthermore, photovoltaic industry has now moved to a new trend of mass-producing the silicon solar cells with thinner active layer, as the manufacturing of solar cell utilizing silicon is a costly and energy-intensive process. However, this may suppress the interaction of the incident photons with the photoactive layer. The photons could pass through the entire structure without being absorbed, resulting in the decrease of power conversion efficiency in thin film silicon solar cells. The active layer of the solar cells consists of *P* type and *N* type semiconductors at where the photovoltaic effect takes place. Figure 1 illustrates the possible interactions of electromagnetic radiation on a solar cell.

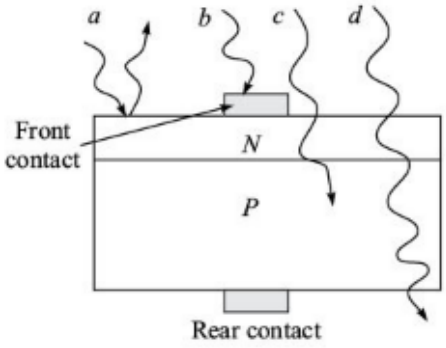

Figure 1.1: The incident solar radiation interacts with a solar cell in several mechanisms including (a) reflection of a radiation from the solar cell surface; (b) reflection or absorption of a radiation by the metal contact; (c) absorption of a radiation by the active layer; (d) transmission of a radiation without absorbed by the solar cell (Solanki, 2015)

In order to increase the power conversion efficiency of solar cell and hence its cost-effectiveness, a variety of approaches have been applied to the solar cells

to reduce the optical losses which are illustrated in Figure 1.1. Anti-reflective coating (ARC) is the most well-known technique used to reduce the optical losses owing to its simplicity, time-effectiveness and low cost in fabrication processes (Lin, et al., 2014). ARC is a thin layer of dielectric material coated on the solar cell, which suppresses the reflection losses by destructive interference (Solanki, 2015). However, this strategy has its limitations such as poor adhesion, limited operating wavelength range (500-600 nm) and limited angle-of-incident radiation. In order to minimize the reflection, the materials should have similar refractive indices with air and the thickness of ARC should be almost equivalent to the optical thickness which is a quarter of the incident wavelength (Solanki, 2015). Nevertheless, the main challenge of this technique is the lack of materials with refractive indices similar to the air (Lin, et al., 2014).

To overcome the drawbacks due to the issues mentioned above, several light trapping techniques have been explored such as to apply nanostructures by coating the solar cell surface with an additional light trapping layer. Among the nanostructures which may involve the need for vacuum systems, lithography and etching processes, nanospheres such as polystyrene (PS) nanospheres and silica (SiO_2) nanospheres, have been proved to have an advantage of cost reduction since the nanostructures can be coated onto large area solar cell with various self-assembly techniques (Wang, Gao and Leu, 2016; Grandidier, et al., 2012).

In this study, we demonstrate a novel approach by utilizing self-assembled poly(methyl-methacrylate-*co*-acrylic acid), P(MMA-*co*-AA), nanosphere

arrays as a light trapping layer to enhance the power conversion efficiency of the solar cell. PS nanosphere or microsphere arrays have been reported to provide promising results in the enhancement of efficiency in various types of solar cells such as crystalline silicon (*c*-Si) solar cells and gallium arsenide (GaAs) solar cells (Lin, et al., 2014; Chang, et al., 2009). In contrast to PS, poly(methyl methacrylate) (PMMA) is relatively stable and high weather resistant. In fact, PMMA is resistant to direct exposure under sunlight and its properties show only small degradation under ultraviolet radiation. Other than that, PMMA possesses superior optical properties due to its optical clarity (i.e. 92% of light transmission). With the presence of the acrylic acid segments, the nanospheres may exhibit a better hydrophilic characteristic which facilitates the formation of a large area of nanosphere array on the solar cell surface. Besides that, the light harvesting efficiency of solar cells can be greatly improved by integrating metallic nanoparticles such as gold and silver nanoparticles. The metallic nanostructures introduce plasmonic effects to scatter incoming sunlight, leading to the increase in path length of the incident light (Lin, et al., 2014). Hence, metallic nanostructures have been used to improve light absorption in amorphous silicon and organic solar cells (Derkacs, et al., 2016; Qiao, et al., 2011). Other metallic structures such as metal gratings and nanoparticle arrays have also been shown to be effective in trapping the sunlight (Ferry, et al., 2010; Kanade, et al., 2015).

1.2 Literature Review

The light trapping techniques currently used to enhance the power conversion efficiency of solar cells are achieved by integration of various nanostructures onto the photoactive region of the solar cells. The nanostructures that have been introduced onto the solar cells to increase the light absorption including nanospheres, nanodomes, nanorods, nanowires and nanopillars. Other approach involves the use of metallic nanostructures for plasmonic light trapping via surface plasmon polaritons, high near-fields or plasmonic scattering (Wang and Leu, 2015). The literature review will cover the adoption of nanostructures which have been utilized to minimize the optical losses and enhance the efficiency of solar cells.

1.2.1 Nanospheres

As mentioned previously, nanosphere arrays have been demonstrated to be more applicable compared to other nanostructures due to their scalability, simplicity and low cost. Recently, a new approach to light trapping was reported using PS nanospheres coated on the ultrathin film or bulk *c*-Si solar cell. (Wang, Gao and Leu, 2016; Lin, et al., 2014). Wang and co-workers (2014) demonstrated an enhancement of power conversion efficiency (PCE) in the ultrathin *c*-Si solar cell by coating with a monolayer of PS nanospheres of 800 nm in diameter. The nanospheres could work as an anti-reflection layer to enhance the PCE by 26.5%. Lin et al. (2014) also reported that an increment in PCE of 21.6% of the bulk *c*-Si solar cell could be achieved via the coating of PS nanospheres. In their work,

they demonstrated that the sub-wavelength PS nanosphere array with diameter of 450 nm could significantly reduce the surface reflection over a broadband spectral region (i.e. 600-900 nm) at the incident angles up to 85°. In addition, the PS colloidal particles with size of 300 nm have also been applied to enhance the PCE of the GaAs photovoltaic cell (Chang, et al., 2009). Chang et al. (2009) reported that the photovoltaic cell achieved the PCE of 13.12 % when coated with the PS nanospheres of 300 nm in size, corresponding to an improvement factor of 8.43% compared to the case without the nanosphere array.

Besides that, Grandidier group has performed a simulation to predict the light absorption improvement of GaAs or thin-film hydrogenated amorphous silicon (*a*-Si:H) solar cell using the periodic SiO_2 nanosphere array (Grandidier, et al., 2012; Grandidier, et al., 2011). The simulation results showed that the short circuit current density (J_{SC}) of the *a*-Si:H solar cell could be enhanced by 12% compared to the case without the presence of SiO_2 nanosphere array with the diameter of 600 nm. Besides, a relative enhancement of 1.8% in PCE of the *a*-Si:H solar cells coated with SiO_2 nanospheres with diameters varying between 650 nm and 750 nm has also been reported (Grandidier, et al., 2013).

1.2.2 Nanodomes

In 2010, Zhu et al has demonstrated novel nanodome *a*-Si:H solar cell as shown in Figure 1.2. The nanodome solar cell consists of periodic structure in the nanoscale for all the layers beginning from the bottom substrate and progressing towards the absorbing layer until to the top layer. The nanodome structure

efficiently suppressed reflection and improved optical absorption over a broad spectral range (i.e. 400-800 nm) and a wide range of incident angle from 0 to 60° (Zhu, et al., 2010). As a result, the nanodome solar cell was able to absorb 94% of the light with wavelengths of 400 to 800 nm compared to 65% absorption of the flat *a*-Si:H solar cell (Zhu, et al., 2010). The nanodome solar cell achieved a very high J_{SC} of 17.5 mA cm^{-2} in contrast to the flat film device with J_{SC} of 11.4 mA cm^{-2} due to the approximately full absorption of light. Moreover, they reported the nanodome solar cell with a PCE of 5.9%, which was 25% higher than the control device.

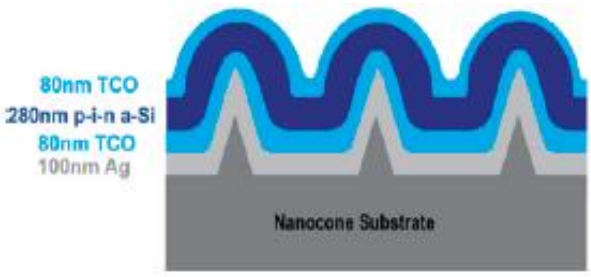

Figure 1.2: Schematic of the cross-sectional structure of nanodome solar cell (Zhu, et al., 2010)

1.2.3 Nanorods

Intensive research works have been carried out to investigate the synthesis of nanorod arrays using numerous metal oxides, such as titanium dioxide (TiO_2), zinc oxide (ZnO) and indium tin oxide (ITO) due to their anti-reflective and light trapping properties. For example, the dye-sensitized solar cell with the integration of TiO_2 nanorods exhibited superior light absorption ability and light harvesting efficiency (Marco, et al., 2010). Moreover, ZnO nanorod film deposited on silicon solar cell has showed a broadband anti-reflection

characteristic which spans from 400 to 1200 nm (Lee, et al., 2008). Pu et al. showed that the performance of ZnO nanorod anti-reflection coating could be further improved by depositing a layer of cadmium sulfide (CdS) nanoparticles onto the ZnO nanorod array as illustrated in Figure 1.3 (Pu, et al., 2014). In this case, the CdS nanoparticles were used to capture the light reflected from the void spaces of the ZnO nanorod array. The light was reflected back by the CdS nanoparticles at the interface between CdS nanoparticles and ZnO nanorods, which would be eventually absorbed by the active layer.

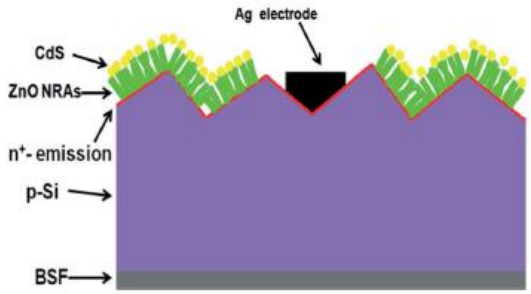

Figure 1.3: Configuration of a *c*-Si with CdS/ZnO nanorod array antireflection coating (Pu, et al., 2014)

In 2014, Chao, Zhan and Li reported a method to develop ITO nanorods from the ITO film in polymer solar cell using wet chemical etching method (Chao, Zhan and Li, 2014). Due to the light tapping effect of ITO nanorods, which increased incident light intensity as well as trapped light in the active layer, the ITO nanorod based polymer solar cell showed 67% and 46% enhancement in J_{SC} and PCE respectively compared to the polymer solar cell with flat ITO electrode.

Furthermore, the use of silicon (Si) nanorods due to its superior light harvesting and carrier collection competency has received much attention for the

application of high efficiency solar cell. He et al. reported a high efficient silicon-based organic hybrid solar cell with the integration of well-organized Si nanorods fabricated using chemical etching (He, et al., 2011). They demonstrated that the reflectance of the solar cell has been reduced after the deposition of Si nanorods due to the light trapping by the nanorods. Compared to the solar cell with planar Si, the PCE of the solar cell with silicon nanorods has increased significantly from 5.6% to 10.3% (He, et al., 2011). Moreover, Si nanorods had been applied to *c*-Si solar cell as an anti-reflection layer (Tsai, et al., 2011). They reported that the *c*-Si solar cell with Si nanorods enhanced the light generated current and PCE by almost 16% and 30% in contrast to a conventional microtextured reference solar cell, respectively. The improvement of light absorption was mainly attributed to the ominidirectional anti-reflection characteristics with wide wavelength range from 400 nm to 1000 nm of the nanostructure.

1.2.4 Nanowires and Nanopillars

Semiconductor nanowires, such as Si nanowires and CdS nanowires, have recently been employed to increase the efficiency of solar cells. The efficiency of a solar cell is greatly dependent on the probability of an incoming photon being absorbed, and then the collection of the produced carriers. Nanowire arrays can potentially offer a unique benefit owing to their anti-reflective and light trapping characteristics. The nanowires, which are vertically orientated, also known as nanopillars. CdS nanopillar array was used to reduce the optical reflection by increasing the exposure length of CdS nanopillars out of the anodic

aluminum membrane (Fan, et al., 2009). Si nanowires are the important nano-scale building blocks particularly for the application of the highly efficient photovoltaic devices due to their unique characteristic of broadband optical absorption and the compatibility feature with the present silicon-based solar cells. In addition, Si nanowires also provide larger surface area with less usage of silicon materials for light harvesting purposes. In 2010, Garnett and Yang demonstrated a simple and scalable method to fabricate radial *p-n* junction silicon solar cell with large area of periodic vertical Si nanowire array via the ion etching technique (Garnett and Yang, 2010). The periodic vertical Si nanowire array showed a strong light trapping effect, resulting in the increase of both J_{SC} and PCE. By applying 5 µm Si nanowires to the 8 µm silicon absorber, the nanowire solar cell showed a 4% higher in J_{SC} compared to the planar control solar cells. Furthermore, the average PCE of 4.83% for the 8 µm-absorber Si nanowire array solar cell was nearly 20% better than the equivalent silicon solar cell. In 2011, Fan et al. presented the use of Si nanowires in the graphene/*n*-type silicon Schottky junction solar cell (Fan, et al., 2011). The Si nanowires created a significant suppression of the light reflectance compared to the solar cell with planar Si as illustrated in Figure 1.4 (Fan, et al., 2011).

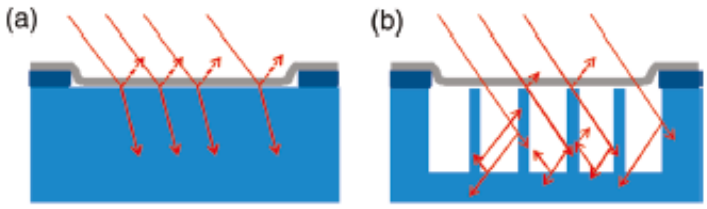

Figure 1.4: Schematics of (a) graphene/ planar Si and (b) graphene/ Si nanowire junctions (Fan, et al., 2011)

1.2.5 Metallic Nanostructures

Metallic nanostructures have shown promising results in effective light trapping for various types of solar cells. Numerous particle shapes and periodic nanostructures have been successfully demonstrated to enhance the absorption properties of solar cells (Chou and Chen, 2014). Three device configurations have been designed using metallic nanostructures to improve the performance of solar cells as shown Figure 1.5 (Tang, Tress and Inganäs, 2014).

The first design involves the deposition of metallic nanostructures on the surface of the active layer. In 2006, Derkacs et al. deposited gold nanoparticles with diameter of 100 nm on the surface of ITO contact of *a*-Si:H solar cell to induce forward light scattering via surface plasmon polaritons (Derkacs, et al., 2006). At optimum gold nanoparticles concentration of 3.7×10^8 cm^{-2} on the solar cell surface, the device PCE has been enhanced from 2.77% to 3% with a relative increment of 8.3%. Besides that, gold nanoparticles had also been employed to improve the PCE of organic solar cell (Qiao, et al., 2011). Qiao et al. blended gold nanoparticles with diameter of 15 nm into the buffer solution of poly(3,4-ethylenedioxythiophene): polystyrenesulfonate (PEDOT:PSS) and then it was spin-coated onto the indium-tin-oxide (ITO) glass to trigger localized surface plasmon resonance (LSPR) (Qiao, et al., 2011). This plasmon-enhancing anodic buffer layer improved the device PCE from 1.99% to 2.36%. Apart from utilizing only spherical gold nanoparticles, Hsiao et al. blended gold nanospheres with gold nanorods in PEDOT:PSS film of organic solar cell and found improved light trapping efficiency (Hsiao, et al., 2012). The embedded

gold nanospheres with diameter of 50 nm had enhanced the PCE from 3.5% to 4.1% with an enhancement factor of 17%. This was attributed to the LSPR effect of the gold nanospheres at 540 nm. When incoporating the gold nanospheres of 49 nm in length and nanorods of 12 nm in diameter into the anodic buffer layer, their device PCE was further increased to 4.3% with a relative improvement of 24% to the existing PCE. The increased device performance was resulted from the extra LSPR excitation at 850 nm which was induced by the nanorods.

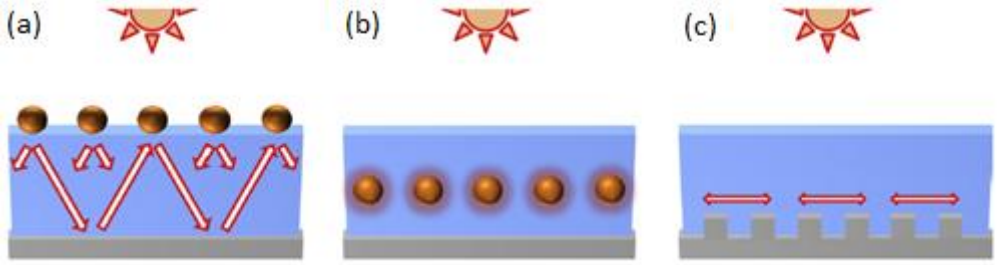

Figure 1.5: Structure designs of plasmonic-enhanced solar cells (a) Incorporation of metallic nanostructures on the surface of the active layer; (b) Integration of metallic nanostructures in the photoactive layer; (c) Fabrication of periodic metallic nanostructures at the interface between the active layer and the metal contact (Tang, Tress and Inganäs, 2014; Chou and Chen, 2014)

Another noble metal, silver, has been shown to exhibit LSPR characteristic. Kim and co-researchers have reported on the incorporation of silver nanoparticles into the organic solar cell via electrochemical deposition (Kim, et al., 2008). The PCE of the solar cell has increased from 3.05% to 3.69% after the deposition of the silver nanoparticles on the transparent electrodes. In 2013, Baek et al. has studied the influence of silver nanoparticles with different diameters which ranges from 10 nm to 100 nm to be incorporated into polymer solar cell (Baek, et al., 2013). The optimum devices reached the ultimate PCE of 7.6% by incorporating silver nanoparticles of 67 nm in size into the polymer solar cell, thereby attaining an enhanced PCE of the photovoltaic cell by 18.8%

compared to the control sample. Additionally, Temple et al has deposited compact layers of silver nanoparticles on the surface of silicon solar cell utilizing electron beam evaporation and followed by thermal annealing (Temple, et al., 2009). The assembled solar cell with the original PCE of 8.51% has risen to 9.06% after the introduction of silver nanoparticles with various sizes ranging from 25 nm to 95 nm. In 2015, Kanade et al minimized the reflection losses and enhanced the device PCE of the silicon photovoltaic cell by coupling the plasmonic oscillations of silver nanoparticles with graphene plasmonics (Kanade, et al., 2015). With the combination of silver nanoparticles (i.e. 3 nm in size) and graphene thin film (i.e. the amount of 30 μL) deposited onto the silicon solar cell, the device performance increased from 9.95% to 10.84% with increment factor of 8.9%.

In the second design of plasmonic photovoltaic devices as depicted in Figure 1.5(b), metal nanoparticles are incorporated into the absorbing layer. For example, Zarick et al. has demonstrated an improved light absorption in DSSC with embedded silica coated gold core/silver shell nanoparticles in the photoactive layer (Zarick, et al., 2016). The greatest improvement was obtained by incorporating 0.44 wt% of the hybrid bimetallic nanoparticles into the DSSC structure. The photovoltaic cell has achieved a PCE of 7.51% compared to the PCE of the control device of 5.97%. This contributed to an enhancement of 26% in the device performance.

Another promising approach to improve the performance of the solar cells is to introduce periodic metallic nanostructures as depicted in Figure 1.5(c). For

instance, Ferry et al. (2010) demonstrated a 160 nm thick *a*-Si:H solar cell with notable light trapping method consisting of two-dimensional periodic silver nanostructure (Ferry, et al., 2010). After patterning the device with the silver nanoparticles of 250 nm in diameter and a plasmonic scatter pitch of 500 nm, the device exhibited the maximum efficiency of 6.6% and an increase in J_{SC} of 46% had been achieved. In 2014, Kirkeminde et al. has demonstrated that a uniform distribution of gold nanopyramids could be prepared through self-assembled lithography (Kirkeminde, et al., 2012). A 50% increment in the photocurrent was determined with the J_{SC} increasing from 2.7 mA cm^{-2} to 4.1 mA cm^{-2} with the introduction of gold nanopyramids (i.e. 100 nm in side length and 30 nm in height) in the organic photovoltaic device. The PCE was calculated to be 200% larger than that of the device fabricated without the nanostructure. In this case, there was an increase in PCE from 0.36% to 1.1%.

1.3 Scope and Objectives of Study

The main objective of this research work is to determine highly efficient light-trapping approach for the application of high PCE of amorphous silicon solar cell. The first stage of this project will focus primarily on the synthesis, coating and characterization of P(MMA-*co*-AA) polymer nanospheres and the nanospheres embedded with the metallic nanoparticles (i.e. gold nanoparticles and silver nanoparticles). An equally important research area will be to investigate the optical properties of the metallic nanoparticles as well as the encapsulation of such nanoparticles within the nanospheres

To achieve the above research goals, the first objective is to synthesize the P(MMA-*co*-AA) polymer nanospheres with a variety of particle sizes and encapsulation of the metallic nanoparticles via emulsion polymerization technique. The second objective is to determine the particle sizes of the polymer nanospheres by using laser diffraction technique. The third objectives cover the study of the properties of the polymer nanospheres using exhaustive spectroscopic, thermal analyses and X-ray diffraction techniques. The polymer nanopsheres encapsulated with the metallic nanoparticles are characterized through tramission electron microscopic, energy dispersive X-ray and ultraviolet-visible light spectroscopic techniques.

Subsequently, the second stage is to fabricate the self-assembled polymer nanosphere arrays onto the solar cells via the evaporation induced self-assembly method. The surface morphology and topology of the polymer nanosphere arrays are characterized using the scanning electron microscopy and the atomic force microscopy, respectively.

The third stage is to evaluate the electrical power output and omnidirectional light harvesting performance of the solar cells under the illumination of AM 1.5 solar simulator and fluorescent light source, respectively. The most important objective is to study the current density-voltage characteristics of the solar cells under the illumination of AM 1.5 solar simulator.

1.4 Organization of Dissertation

Chapter 1 includes the problem statement and the scope of the study of this research work. Chapter 2 describes the fundamental of the working principle of solar cells as well as the fundamental theory of light trapping mechanism. Chapter 3 illustrates the synthesis and self-assembly of colloidal particles. Chapter 4 covers the details of methodology and instrumentation. Chapter 5 and 6 will present the results and discussion of the experiment outcomes. Finally, the conclusion and recommendations for future research will be presented Chapter 7.

1.5 Summary

This chapter has first introduced the problem statement of this study and followed by the literature review about the studies which have been carried out by other researchers in order to minimize the optical losses of solar cell. The literature review has summarized different nanostructures which have been applied onto the solar cells including nanospheres, nanodome, nanorods, nanowires and nanopillars as well as metallic nanostructures. In the problem statement, the main purpose of this study has been addressed. Although silicon based solar cells occupy more than 70% of the market share presently, commercial solar cells still show power conversion efficiency below its intrinsic limit which is 29%. It has been found that the high refractive index of silicon results in 40% of the incident light lost through surface reflection. Among the nanostructures have been reported, nanospheres are known as the most

applicable solution to overcome this problem due to their simplicity, low cost and scalability. As a result, we have proposed in the scope of study that poly(methyl methacrlate-*co*-acrylic acid) polymer nanosphere array would be deposited onto the solar cell in order to minimize the surface reflection.

CHAPTER 2

PHYSICS OF PHOTOVOLTAIC CELL AND NANOPHOTONIC LIGHT TRAPPINGS

2.1 Historical Development of the Photovoltaic Cell

Solar cell, which is also known as photovoltaic cell, is a *P-N* junction semiconductor device with electrodes contacting at both sides of the device. It converts solar energy to electrical energy in a process called photovoltaic effect which was first discovered by Edmund Becquerel in 1839. He reported the photovoltaic effect after observing a light-driven chemical reaction that has finally generated electric current. Figure 2.1 illustrates the photovoltaic effect in a solar cell. It occurs when sunlight is directing towards the solar cell. In this case, the photons provide sufficient energy to generate free carriers (i.e. electrons and holes) in the *P-N* junction, resulting in a potential difference. The generated photovoltage across the photovoltaic cell will then drive the current to flow in an external circuit across the load as shown in Figure 2.1.

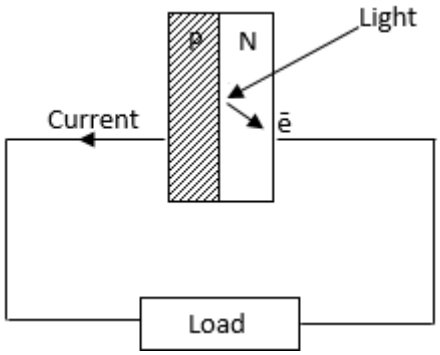

Figure 2.1: The photovoltaic effect that occurs in a solar cell (Nelson, 2005)

To date, there have been several generations of solar cells. In general, it can be divided into three generations. The first generation of solar cell is normally made of silicon wafers, which is known as bulk crystalline silicon (*c*-Si) solar cells. In 1954, Chapin, Fuller and Pearson introduced the first silicon solar cell, which has successfully converted sunlight into electricity but with low power conversion efficiency (PCE) of merely 6%. Currently, more than 90% of the solar cells are manufactured using silicon and this is mainly due to the factors such as low cost, high stability and relatively good device performance (Solanki, 2015). The maximum PCE attained is about 20-25% and the fabrication processes employed are similar to the processes used in the semiconductor industry (Tétreault and Grätzel, 2012). However, almost half of the raw material is lost during the sawing process of the silicon wafer. As a result, a new approach has to be explored in order to minimize the waste. This include the fabrication of the *c*-Si solar cells with thinner silicon wafers.

Meanwhile, the second generation solar cells are fabricated utilizing amorphous silicon (*a*-Si, i.e. with PCE of about 8 to 12%), cadmium telluride (CdTe, i.e. with PCE of about ≈ 12 to 17%) and copper indium gallium selenide (CIGS, i.e. with PCE of abiut 17 to 20%) (Tétreault and Grätzel, 2012). As compared to the conventional bulk *c*-Si solar cells, the second-generation solar cells are fabricated adopting thin-film technologies. This new technique has not only provided benefits such as less material usage, it also reduces energy consumption in manufacturing of the photovoltaic devices due to the low temperature processes (Solanki, 2015). Nevertheless, the use of the second-generation solar cell is limited by a few factors. For instance, the hydrogenated

a-Si suffers from low PCE in contrast to the conventional bulk crystalline silicon solar cells due to the large number of defects. Besides, the raw materials, such as indium and telluride used in the fabrication of the thin film of CdTe and CIGS are poisonous and harmful to the environment. Furthermore, these elements are rare and hence pose a high risk in terms of the materials availability. (Solanki, 2015)

The third generation solar cells are the organic semiconductors (*i.e.* with PCE of about 3% to 8%) and dye-sensitized solar cells (*i.e.* with PCE of about 6 to 13%). The organic-semiconductor-based solar cells can be of low production cost while offering good power conversion efficiencies. This could be due to the low material requirement as well as low temperature processing through solution-based scalable roll-to roll fabrication. (Tétreault and Grätzel, 2012) Therefore, these types of solar cells have the potential to supply low cost electrical power in the future. Nonetheless, the degradation of the organic materials under prolonged sunlight exposure will remain as the biggest challenge of the third generation solar cell (Zhang, et al., 2012).

2.2 Physics of the *P-N* Junction

Semiconductor materials possess band gaps ranging from 0.5 to 3.0 eV (Nelson, 2005). In semiconductors, the fully occupied band is known as valance band and the unoccupied band is called conduction band, in which both bands are separated by an energy band gap. As for the metals, both of the valance and conduction bands are overlapping with each other. The electrons in metals can

move freely under any applied electric field and hence metals are good electric conductors. In order to conduct electricity, the electrons in the semiconductors have to acquire enough energy in order to move to the closest unoccupied energy level. For this reason, the semiconductors at room temperature will have low conductivity due to the facts that most of the electrons will not have sufficient energy to overcome the band gap.

Photovoltaic devices collect solar energy in the form of electrical energy through the generation of free carriers or electron-hole pairs followed by the separation of charge carriers. As photovoltaic devices are illuminated by solar radiation, the photons are absorbed within the semiconductor. The photons with sufficient energy can trigger the excitation of electrons from valance band to conduction band in the semiconductor. Subsequently, the excited electrons are collected through the process called charge separation. (Solanki, 2015)

In order to generate electricity, a *P*-type semiconductor is connected to an *N*-type semiconductor, which produces a built-in electric field to drive the excited electrons in an external circuit. In *P*-type semiconductor, the concentration of hole is substantially higher than the number of electrons; whereas the number of electrons in *N*-type semiconductor is significantly larger than the number of holes. When a photovoltaic semiconductor is exposed to sunlight, the excited electrons tend to flow from *P* side to *N* side. At the meantime, the generated holes move towards the opposite direction. This causes the separation of charge carriers that enter the external circuit and thus converting light energy into electrical energy.

Additional electrons and holes in *P*-*N* semiconductors are introduced through a process known as doping. Figure 2.2 illustrates the bonding models and energy band models in silicon-based *P*-*N* semiconductors after doping. By adding the elements in column III of the periodic table such as aluminum in silicon, additional holes are created in valance band (E_v) of *P*-type semiconductor. The elements in column III are trivalent but the silicon require four additional electrons to form covalent bonding in a stable state. Therefore, the silicon will absorb one electron in order to complete the covalent bond, resulting in an additional energy level known as acceptor level (E_a) to be created. Since the acceptor level is very near to the valance band (*i.e.* small energy gap), the electrons can easily be excited from the valance band to the acceptor level, giving rise to the creation of holes in the valance band. Likewise, the number of electrons in conduction band (E_c) of *N* type semiconductor is increased by introducing the elements in column V such as phosphorus in silicon. The extra one electron contributed by the elements; resuls in the formation of donor energy level (E_d) which is very near to the conduction band. Thus, electrons at the donor energy level are easily excited to the conduction band, creating an electron rich conduction band. (Solanki, 2015)

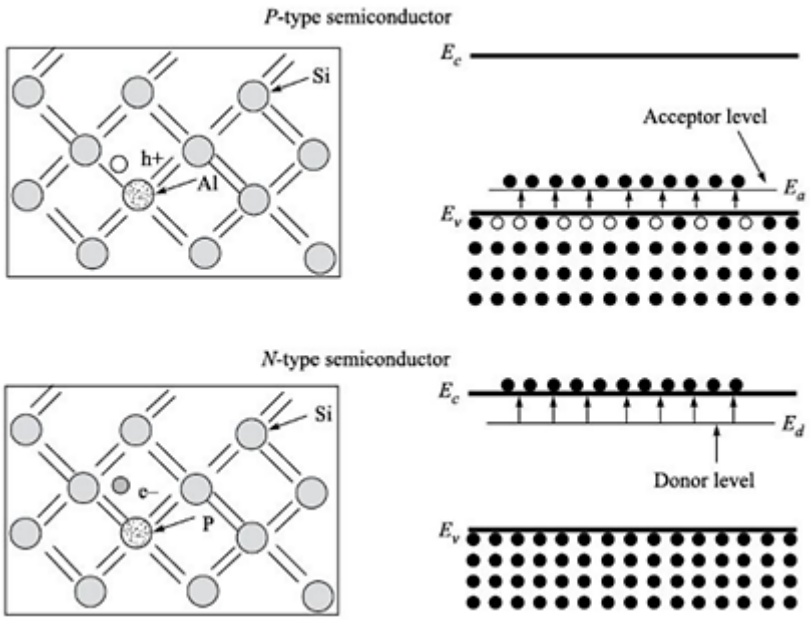

Figure 2.2: The bonding models and energy band models in *P* type and *N* type semiconductors (Solanki, 2015)

2.3 Electrical Characteristics of Photovoltaic Cell

The electrical performance of a photovoltaic cells can be characterized by using a solar simulator. The common electrical characteristics are short circuit current, open circuit voltage, fill factor and power conversion efficiency. Each of these characteristics will be further elaborated in sub-sections 2.3.1, 2.3.2 and 2.3.3, respectively. Figure 2.3 (a) illustrates the setup of a solar simulator system. The electrical output of such system yields the current-voltage (*I-V*) curve as shown in Figure 2.3 (b). The solar simulator is normally equipped with arc lamp (*i.e.* xenon or mercury arc lamp) in order to provide the illumination spectrum that matches with the spectrum of the sun at AM 1.5. An internal sweep circuit in the solar simulator system enables the current and voltage measurements that ultimately yields the *I-V* curve.

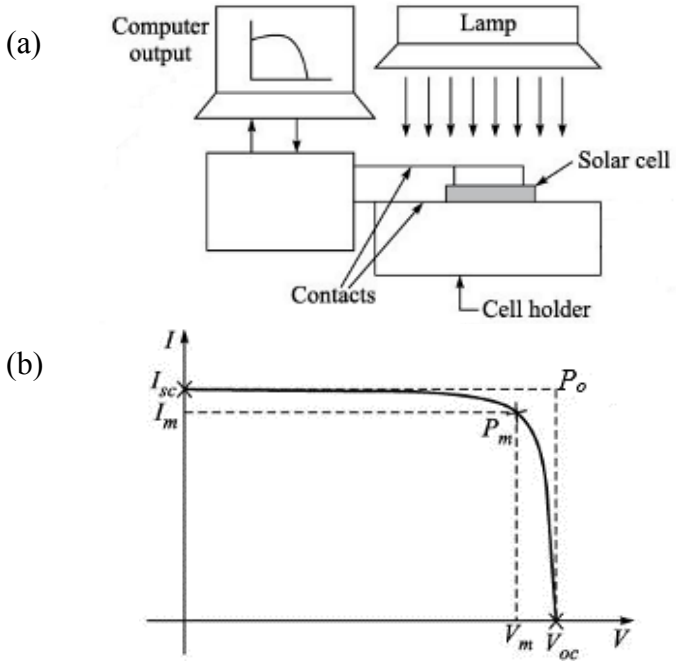

Figure 2.3: (a) Solar simulator system to measure the *I-V* characterization of a photovoltaics cell; (b) A typical *I-V* curve of a solar cell (Solanki, 2015)

2.3.1 Short Circuit Current

Short circuit current (I_{SC}) is the maximum current generated by a solar cell when the terminals of solar cell are connected in series with the ammeter. The I_{SC} is usually expressed in terms of current density (J_{SC}) or mA cm^{-2}. The current flow is also known as photocurrent as the current is generated from the absorbed photon flux. Free carriers are generated when photons are absorbed in the solar cell and subsequently transported to the external circuit. In order to generate the photocurrent, a photon must possess sufficient energy that must be at least equaled or larger than the band gap energy of the material. This indicates that the short circuit current is correlated to the band gap of the material. A material with large band gap will produce less number of electrons in contrast to the material with low band gap. As a result, the short circuit current is larger for a material with smaller band gap. (Solanki, 2015)

2.3.2 Open Circuit Voltage

Open circuit voltage (V_{OC}) is the maximum voltage shown by the solar cell when the terminals of solar cell are connected in parallel with the voltmeter. The unit of V_{OC} is normally mV or V. If the energy of a photon is higher than the band gap, it will be absorbed by the electron and resulting in the excitation of the electron from valance band to conduction band. This increases the potential energy of the electron equivalent to the band gap energy. (Solanki, 2015)

2.3.3 Fill Factor and Power Conversion Efficiency

The photovoltaic cell operates in the range from zero to V_{OC}, in producing the equivalent electrical power. The electrical power delivered is expressed as:

$$\mathrm{P} = \mathrm{IV}$$

A device attains a maximum power at the maximum power point. It occurs when the voltage and the corresponding current are V_m and I_m, respectively as illustrated in Figure 2.3(b). Fill factor (FF) is defined as the ratio of the maximum output power (P_m) of a solar cell to the ideal power (P_o):

$$\mathrm{FF} = \frac{\mathrm{P_m}}{\mathrm{P_o}} = \frac{\mathrm{V_m I_m}}{\mathrm{V_{oc} I_{sc}}}$$

It is related to the resistive losses in the solar cell. The power conversion efficiency (η) of the solar cell is the maximum power (P_m) produced at operating point as a fraction of the incident power by solar radiation (P_{rad}):

$$\eta = \frac{\mathrm{P_m}}{\mathrm{P_{rad}}} = \frac{\mathrm{V_m I_m}}{\mathrm{P_{rad}}} = \frac{\mathrm{V_{oc} I_{sc} FF}}{\mathrm{P_{rad}}}$$

2.4 Light Trapping to Minimize of the Optical Losses of Photovoltaic Cell

Light trapping technique is a photon management strategy, which has been successfully demonstrated for the minimization of optical losses and efficiency enhancement in practical photovoltaic cells. With the development of nanotechnology and the capability of guiding the flow of photons, numerous research works have focused on the alteration and improvement of light absorption at nanoscale, for the enhancement of both short circuit current and open circuit voltage of solar cells (Wang, et al., 2014). Improvement on light trapping can be accomplished by placing surface gratings or introducing additional light scattering layers near the active layer of solar cells. The light trapping effects induced by spherical particles and plasmonic structures are discussed in the following sections.

2.4.1 Light Scattering Effects by Spherical Particles

Light scattering is a usual optical phenomenon that occurs upon the transmission of light through an object. When light shines upon an object, it may either transmit in the forward direction which results in refraction and absorption, or transmit in the reverse direction that gives rise to reflection. Besides, light is dispersed omnidirectionally if the dimension of the object is of the order of the wavelength of the incident light. This kind of optical phenomenon is known as light scattering. The object that results in light scattering is called scatterer or scattering center. Among the theories that have been developed to explain the light scattering process, Rayleigh scattering theory and Mie scattering theory

are normally applied to spherical scatterer for example, droplets and particles. (Zhang, et al., 2012) A spherical particle affects light transport through its scattering modes, which are determined by the particle size of the particle (Lin, et al., 2014). Figure 2.4 illustrates two scattering behaviors, which are Rayleigh scattering and Mie scattering.

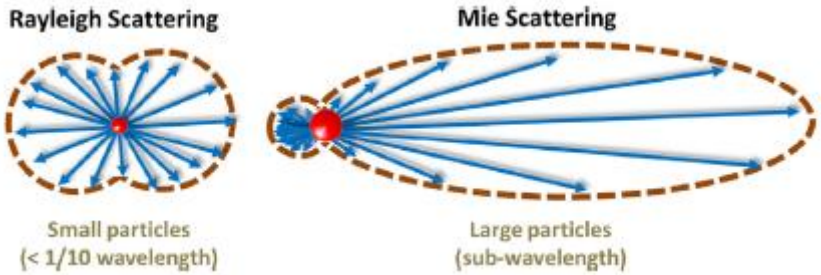

Figure 2.4: Schematic of the differences between Rayleigh scattering and Mie scattering of spherical particles (Lin, et al., 2014)

Lord Rayleigh proposed the theory of scattering by a dielectric particle with a radius much smaller than the wavelength of incident light in 1899. If the radius of spherical particles is much less than the wavelength of incident light (i.e. < 1/10 wavelength), Rayleigh scattering will be predominant. The incident light is scattered omnidirectionally and the intensity of forward and reverse scattering are of the same magnitude in Rayleigh scattering. (Lin, et al., 2014) In 1908, Gustav Mie developed the theory of scattering by a large particle of a size approximately equal to the wavelength. The Mie scattering theory can be applied to both light absorbing and spherical particles. Mie scattering happens as the scattering centers are in sub-wavelength range, in which the incident light is more likely to be scattered forward in contrast to reverse scattering. (Lin, et al., 2014)

2.4.2 Plasmonic Effects by Metallic Structures

When metals are irradiated by electromagnetic radiation, the phenomenon of oscillation of free electrons around the metal ions and the electromagnetic field is called surface plasmon. (Haugan, 2011) The two well-known surface plasmons observed in the excited metal surface are localized surface plasmons and surface plasmon polaritons.

Localized surface plasmons are the collective oscillations of free electrons confined locally by metal nanostructures. Figure 2.5 (a) represents the localized surface plasmons that occur in the metal nanoparticles. When the free electrons are dislocated relative to the fixed positive lattice ion due to the propagation of electromagnetic wave, an attraction force resulting from Coulomb attraction between electrons and lattice ions causes oscillation of the electron cloud corresponding to the lattice ion. (Kelly, et al., 2003) This results in the scattering of the incident light with specific wavelength which is known as the plasmonic resonance wavelength of the metal nanoparticles. The oscillation wavelength is determined by the size and shape of the particles as well as their dielectric environment. Since the excited plasmons are localized and cannot be propagated inside the nanoparticle, this process is called localized surface plasmon resonance. (Chou and Chen, 2014)

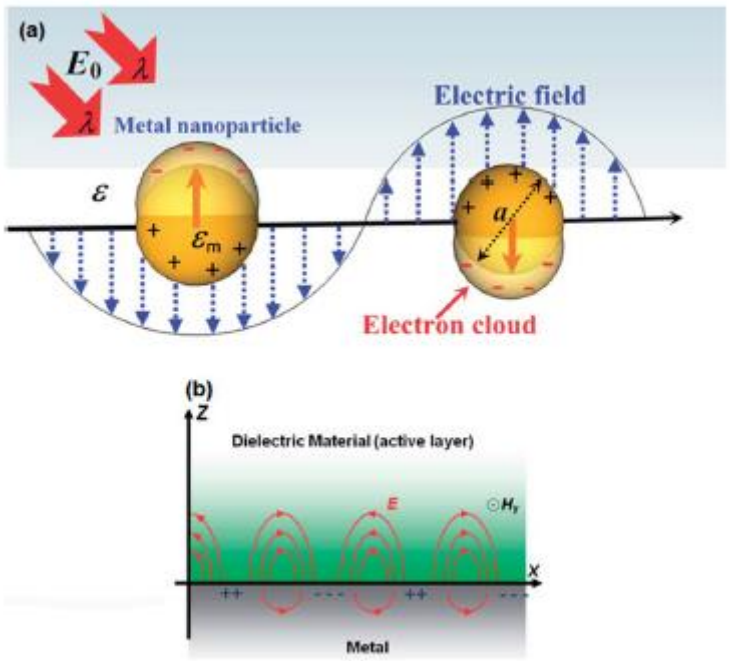

Figure 2.5: (a) An illustration of plasmon oscillation of metal nanoparticles with diameter *a*, showing the dislocation of electron cloud corresponding to the lattice ion triggered by the electric field E_0 of the electromagnetic radiation of wavelength λ; (b) A schematic diagram of surface plasmon polariton triggered at the metal-dielectric interface (Chou and Chen, 2014)

The localized surface plasmon provide the local enhancement of electromagnetic field due to the strong resonance effects, resulting in effective light concentration and the enhancement factor can achieve as high as 100. Nevertheless, the plasmonic near field surrounding a metal nanoparticle declines exponentially with regard to the distance from the nanoparticle's surface. The decay lengths of the electric field are typically of the order of the size of metal nanoparticle. Apart from that, the decay lengths also rely on the dielectric properties of the medium and the metal nanoparticle. (Chou and Chen, 2014)

The second type of excited surface plasmons on metal surface as illustrated in Figure 2.5 (b), which are known as surface plasmon polaritons, are associated

with coherent oscillations of electromagnetic waves at the interface between metal and dielectric layer. The electromagnetic field of a surface plasmon polaritons is limited at the metal surface, in which the electric is enhanced vertically to the surface. (Chou and Chen, 2014) When light is irradiated on a surface with surface plasmon polartions triggered by metal nanoparticles, this result in the bending of light travelling along the metal-dielectric interface or moving in lateral direction inside the interface, which may then be absorbed by the photoactive dielectric material. (Haugan, 2011)

2.5 Summary

In summary, this chapter has provided an introduction about the historical development and working principle of solar cell. The four characteristics of solar cell, which include short circuit current density, open circuit voltage, fill factor and power conversion efficiency, are crucial in determining the light harvesting characteristics of solar cell. These four parameters will be used to evaluate the light harvesting characteristics of the solar cell to be coated with the polymer nanospheres. The light trapping mechanisms of spherical particles, which are Mie scattering and Rayleigh scattering, have also been explained in this chapter. Besides that, this chapter has also introduced the localized surface plasmon happened in the metallic nanostructures. These light trapping mechanisms of spherical particles and metallic nanostructure will be applied in the discussion of Chapter 6.

CHAPTER 3

SYNTHESIS AND SELF-ASSEMBLY OF COLLOIDAL PARTICLES

3.1 Synthesis of Colloidal Particles

Colloidal particles are the basic building blocks for the preparation of colloidal arrays. The most common and widely used colloidal particles are silica particles and polymer spheres. Monodispersed silica particles can be prepared through Stöber process which is first reported by Stöber and Fink in 1968. They obtained uniform sizes of silica particles by hydrolyzing a diluted tetraethylorthosilicate in ethanol at alkaline pH. The sizes of silica colloids can be controlled from 50 nm to 2 μm by adjusting the concentration of reactants. In order to prepare polymer colloids with controlled particle size distribution, heterogeneous polymerization techniques such as the miniemulsion polymerization and the emulsion polymerization process can be applied. The surface chemistry properties of polymer spheres can be modified by incorporating stabilizing fragments such as co-monomers and charged initiators. Moreover, the self-assembled polymer sphere arrays also allow post-modification, such as gradient etching, which can be used as a convenient template for inverse opals. (Freymann, 2013)

3.1.1 Emulsion Polymerization

Emulsion polymerization is a typical preparation method for polymer particles. The emulsion polymerization technique has been widely utilized to produce

polymer latexes with different colloidal and physiochemical properties since Harkins first reported it in 1947. Polymer spheres such as PMMA and PS have been prepared in large amount by using this technique. Figure 3.1 shows the major components in an emulsion polymerization system which consists of monomers, dispersion medium such as water, surfactants or emulsifiers and water-soluble initiators. Surfactant is existed in the aqueous phase as free molecules at very low concentration. When the surfactant concentration exceeds the critical micelle concentration, the excess surfactant molecules will aggregate to form small colloid clusters known as micelle (Odian, 2004). In the system, micelles are formed as the amount of surfactant is above its critical micelle concentration. Monomers are dispersed as monomer droplets stabilized by the surfactant or in the micelles of the surfactant.

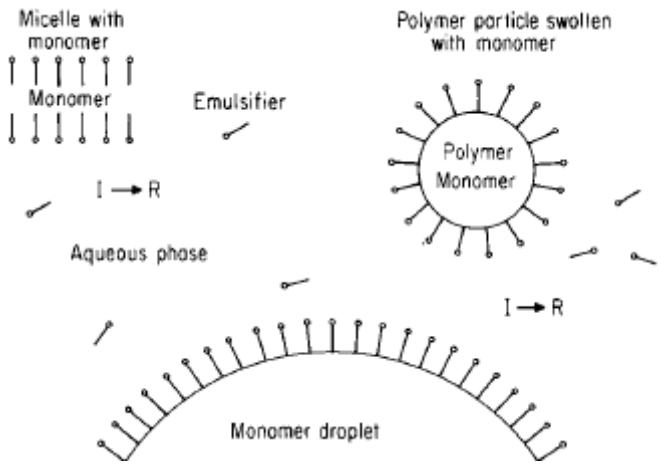

Figure 3.1: Schematic diagram of the compositions of the emulsion polymerization system, in which *I* represents the initiator and *R* is the free radicals generated (Odian, 2004)

When the surfactant concentration is less than the critical micelle concentration, the additional surfactants are adsorbed at the oil/water interface as single ions

creating monolayer as shown in Figure 3.2(a). On the other hand, more surfactants will be adsorbed at the oil/water interface as the concentration of surfactant is increased. Figure 3.2(b) illustrates that the additional surfactants are adsorbed at the interface in the form of micelle aggregates when the surfactant concentration is above the critical micelle concentration. (Rowe, 1965) This causes the increase of stabilized oil/water interfacial area, resulting in the decrease of the particle size of the polymeric spheres.

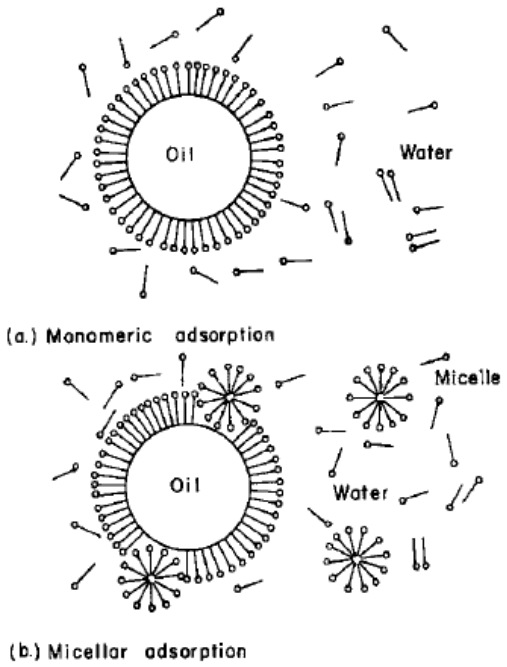

Figure 3.2: Schematic diagrams of surfactants adsorbs at oil/water interface where (a) oil particle stabilized by condensed monolayer; (b) oil particle stabilized by adsorbed surfactant and micellar aggregates (Rowe, 1965)

Goodwin and Ottewill introduced the mechanism for conventional emulsion polymerization process in 1982. Emulsion polymerization starts with the dissociation of the initiators to form free radicals in the aqueous phase where they may find a few monomers to react with the free radicals. This results in the formation of nuclei-oligomers which diffuse into the monomer-rich micelle

environment. The monomers in the micelles are subsequently added to the oligomers and grow into long chain polymer molecule. The growing chain is protected from termination until a second radical diffuses into the micelle. In the meantime, the monomer droplets function as reservoir to supply monomers to the polymerization reaction via diffusion continuously. The polymerization will end at the point when all the monomers have been consumed. (Xia, et al., 2000)

The sizes of polymer spheres can be controlled in the range of between 20 nm and 1 μm by using emulsion polymerization technique. The particle size distribution of polymer particles depends on both the polymerization method and the polymerization recipe. The particle size of polymer spheres can be controlled and adjusted through seeded nucleation in the polymerization process. The use of seed particles enables manipulation of the final particle size and size distribution by altering both seed properties including the number and size of seed particles, and the amount of monomers added during the polymerization process. Even though the duration for particle nucleation is quite short, growth of particle seed at the beginning stage of polymerization is critical in establishing the final polymer particle size, particle size distribution and properties of polymer dispersions. The most significant techniques for effecting polymer dispersions by emulsion polymerization are semi-batch or feed processes. Semi-batch processes offer the advantages to prepare polymer dispersions with controlled particle size distribution, particle morphology and polymer composition depending on the required properties. (Caruso, 2004)

3.1.2 Advantages of Emulsion Polymerization

The emulsion polymerization process has several distinct advantages. The polymerization process can be easily controlled due to the physical state of emulsion system. For example, the use of water as the dispersion phase provides outstanding heat transfer capacity during the process of polymerization. Therefore, the thermal and viscosity problems are negligible in emulsion polymerization (Odian, 2004). Moreover, emulsion polymerization offers a benefit to synthesize high molecular weight polymers at comparatively rapid polymerization rate. This is because separation of free radicals among the isolated monomer-swollen micelle in the polymerization systems prohibits the probability of bimolecular termination of free radicals and chain transfer reactions (Chern, 2008).

3.2 Self-Assembly of Colloidal Particles

3.2.1 Interactions of Colloidal Particles in Aqueous Medium

Colloidal particles in dispersion tend to arrange themselves into ordered or disordered structures. Such arrangement arises from the balance of interactions that exist in the colloidal dispersion, which include van der Waals attraction, electrostatic repulsion and steric repulsion. The combination of these interactions results the interaction potential and the stability condition of colloidal particles. This theory is known as DLVO theory, which was developed by Derjaguin, Landau, Verwey and Overbeek. (Derjaguin and Landau, 1941;

Verwey and Overbeek, 1948) One of the important features of this theory is about the working range of the electrical potential surrounding the particle, as illustrated in Figure 3.3. At the surface of the particles, ionic initiator end groups and ionic repeating units act as the covalently attached permanent charges. Moreover, the adsorbed co-ions such as surfactants also contribute to the charges on the particles. A distinct layer known as Stern layer consists of counter-ions with opposite charges is formed around the adsorbed and covalently bound ions. Due to the thermal motion electrostatic interactions of the ions, a non-uniform diffuse electrical double layer is established surrounding the particles, which consists predominantly of counter-ions with minor amount of co-ions. The shear plane of the particle is positioned within this layer and the potential at the shear plane is defined as zeta-potential. When two electrically charged particles approach to each other, they will face a net repulsion due to the interaction of ions at the diffuse layers. If the net repulsion potential is greater than the kinetic energy of the collision, coagulation of the two particles will not occur. (Schlüter, Hawker and Sakamoto, 2012)

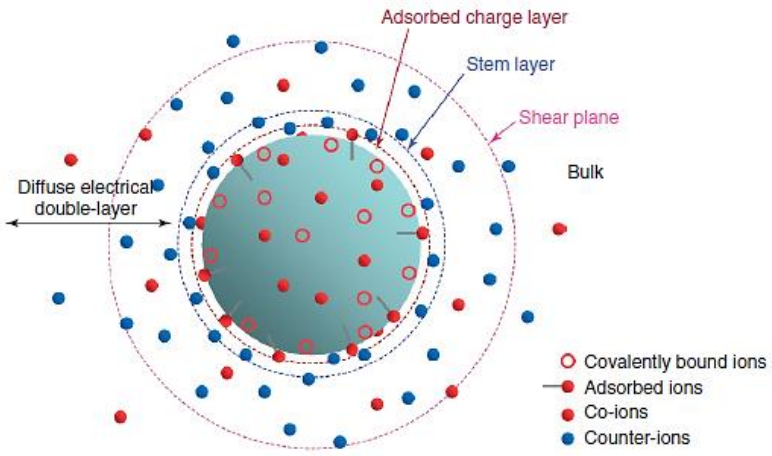

Figure 3.3: Schematic diagram of ionic layers formed surrounding the charged colloidal particles (Schlüter, Hawker and Sakamoto, 2012)

The DLVO theory is the sum of the three potential resulting from the long-range attractive interaction, the steric repulsive interaction and the long-range electrostatic repulsion. Figure 3.4 illustrates the DLVO potential in respect to the distance between two spherical particles. The first minimum (I) occurs at a very close distance to the particle surface is resulted from the strong van der Waals force. The maximum (II) occurs at a distance further away is induced by the electrostatic repulsion between the particles. Lastly, the second minimum (III) occurs at a distance which is even further away. With regard to colloidal stability, coagulation of the particles is related to the first minimum. The particles are irrevocably agglomerated when they achieve this minimum, which can be averted by the energy barrier resulting from electrostatic repulsion. Thus, the stability of a colloidal dispersion is determined by the height of the energy barrier. The secondary minimum is referred to the irreversible flocculation. (Vogel, Weiss and Landfester, 2012)

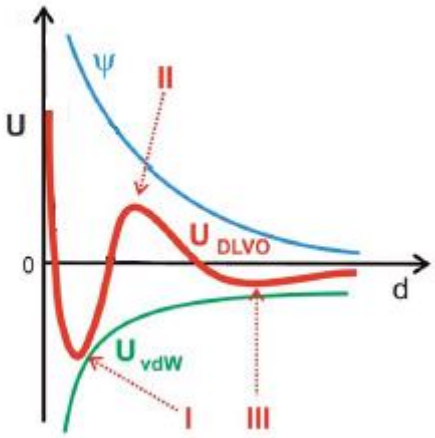

Figure 3.4: Total interaction potential of two spherical particles based on the DLVO theory (Vogel, Weiss and Landfester, 2012)

3.2.2 Evaporation Induced Self-Assembly

Two-dimensional (2D) colloidal arrays can be deposited on a solid substrate by using evaporation induced self-assembly approach. The evaporation induced self-assembly technique was primarily explored by Nagayama and co-workers in 1990s. Figure 3.5 illustrates the evaporation induced self-assembly technique and its mechanism.

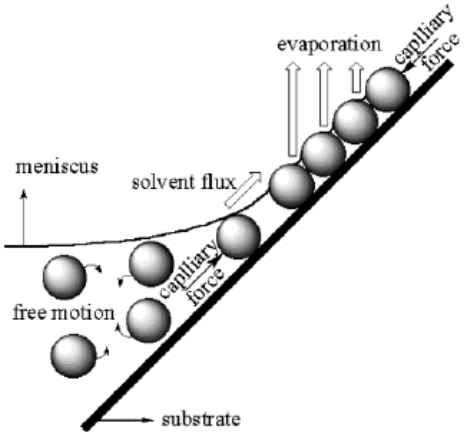

Figure 3.5: Schematic illustration of the evaporation induced self-assembly technique and its mechanism (Cong and Cao, 2003)

During the self-assembly process, two main forces, which are capillary forces and dipolar repulsive forces, have to be considered when colloidal particles are deposited from an aqueous dispersion onto a solid substrate. (Vogel, Weiss and Landfester, 2012) When the water thickness is comparable to the dimensions of colloidal particles upon evaporation, the liquid film around the colloidal particles deforms and capillary forces occur. At the same time, nucleus is formed, which is composed of a few colloidal particles. This enables more particles to move in the direction to the nucleus via a convective transport, and consequently organize surrounding the nucleus owing to the attractive capillary forces. (Xia,

et al., 2000) In addition, dipolar repulsive forces arises among the interface of the particles because of the anisotropic around the particles. (Vogel, Weiss and Landfester, 2012)

The evaporation induced self-assembly technique is relatively simple as compared to the other approaches, such as air-liquid interface self-assembly and directed assembly. Many sources in literature have provided excellent results with this technique. The methods that have been developed based on the principle of evaporation induced self-assembly include vertical deposition and dipping methods, horizontal convective deposition and horizontal evaporation methods. The vertical deposition and dipping methods are further discussed in the following section.

3.2.3 Vertical Deposition and Dipping Methods

To date, the vertical deposition method is the most widely used method to deposit colloidal arrays on solid substrates (Galisteo-López, et al., 2011). In this method, a substrate is vertically dipped into a dispersion and the colloidal arrays are formed by slow evaporation of the dispersion. As illustrated in Figure 3.5, the particles spontaneously self-assemble into mono- or multilayer colloidal arrays in the meniscus formed among the substrate, the dispersion and the air during the evaporation.

This method was demonstrated by Jiang et. al (1999) to develop multilayered colloidal crystals of silica spheres. They reported that the number of layers of

silica sphere arrays deposited on the substrate could be varied from single monolayers to 100 layers by altering the particle volume fraction and the particle size. As reported by Im et al., the thickness of opal films could also be controlled by changing the tilted angle of the substrate placed into the colloidal suspension (Im, Kim and Park, 2003). Instead of varying the concentration of the suspension, they dipped the substrates into the suspension at a tilted angle. When the angle was increased from -10° to 30°, the shape of the contact line became smoother and the thickness of opal films increased. Moreover, Kuai and co-wokers (2004) studied the growth parameters, such as relative humidity, evaporation temperature and final drying condition, in the deposition of high quality polystyrene colloidal crystals. Later, Yoldi et al. and Li et al. demonstrated the effects of solvent in the fabrication of opal film from the polystyrene suspensions (Li and Marlow, 2006; Yoldi, et al., 2008). The properties of solvents, such as the viscosity, surface tension and volatility, showed great influence on both of the surface morphology and microscopic structure of the opal films.

Instead of relying on the evaporation rate, a different way to manipulate the growth rate of colloidal structures is to lift the substrate out from the colloidal suspension with a constant speed using an electric motor. This concept was first proposed by Dimitrov et al. and later by Gu et al. to produce large areas covered with homogeneous monolayers and ordered three-dimensional crystals (Dimitrov and Nagayama, 1996; Gu, Fujishima and Sato, 2002). As the substrate is slowly moved in reversed direction to the crystal growth, a monolayer or multilayer is formed and growing as the substrate is constantly

removed from the suspension. The relationship between the film thickness and the concentration of suspension is given in Equation 3.1 as follows:

$$k = \frac{\beta L j_e \varphi}{0.605 d v 91 - \varphi)} \quad \text{(Eq. 3.1)}$$

where k is the number of layers, β is the ratio of the velocity of the particles in suspension and the fluid velocity, L is the height of the meniscus and j_e is the evaporation rate of the suspension. Moreover, φ is the particle volume fraction, d is the diameter of colloidal particles and v is the growth rate of the film defined by lifting speed (Gu, Fujishima and Sato, 2002). The inherent drawback of the method relying on the evaporation of solvent is that the film thickness tends to increase towards the end of deposition. This is because the concentration of colloidal suspension gradually increases during evaporation, which leads to a higher growth rate of the film and resulting in a thicker layer. Thus, this method is hardly used to produce the opal film with homogeneous thickness. This problem can be solved by lifting the substrate out of the suspension, in which the growth rate is mainly determined by the lifting speed.

3.3 Self-Assembled Colloidal Structures

Colloidal structures with submicrometer length scale can have strong interaction with light; numerous notable optical responses can be designed and adapted based on the types and parameters of their structures (Kim, et al., 2011). Colloidal structures can be classified into two categories according to the arrangement of colloid in the structures, namely photonic crystals and photonic glasses. Figures 3.6 (a) and (b) illustrate the packing characteristic of the photonic crystals and photonic glasses respectively.

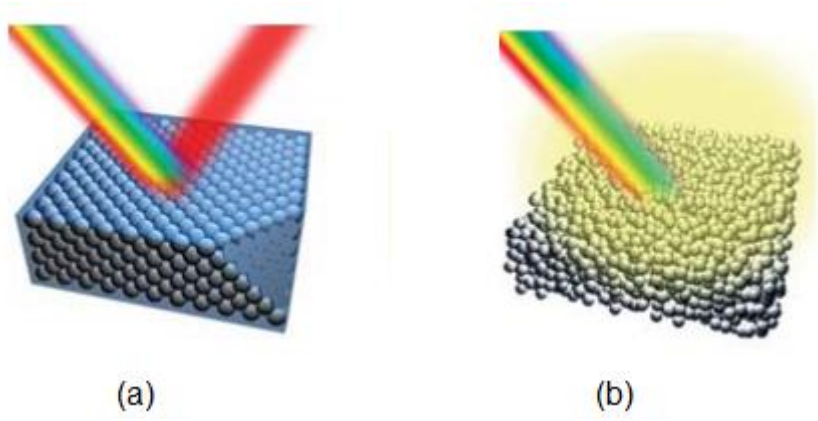

Figure 3.6: (a) Ordered packing and (b) disordered packing of colloidal particles and their interaction with light (Galisteo-López, et al., 2011)

The photonic crystals are defined as an ordered array with periodicity at the scale of the wavelength of light (Freymann, et al., 2013). It can be classified into three categories, which are one-dimensional, two-dimensional and three-dimensional colloidal crystals. One-dimensional (1-D) photonic crystals are one-dimensional chain structure formed by colloids as illustrated in Figure 3.7(a). Lord Rayleigh first studied one-dimensional photonic crystal in 1887, who demonstrated the existence of high reflectivity of light over a distinct wavelength range (Freymann, et al., 2013). To date, the one-dimensional structures which are also known as Bragg mirrors have been used for enhancing the efficiency of solar cells, optimizing the performance of lasers and augmenting the light extraction and color purity of light emitting diodes (Freymann, et al., 2013). Two-dimensional photonic crystal, which consists of a single layer of an ordered arrangement of colloid, is demonstrated in Figure 3.7(b). The two-dimensional (2-D) structures have been explored widely for the use as masks or templates for colloidal lithography, which had been demonstrated to achieve internal total reflection by confining light in a nanoperiodic third direction (Qi, et al., 2004; Cong, et al., 2013). Three-

dimensional structures have a multilayer ordered crystal structure. Three–dimensional (3-D) colloidal crystals are widely employed to develop porous materials or inverse opals with well-ordered periodicity and interconnected pore systems (Cong, et al., 2013). Moreover, the three-dimensional structures have been intensively studied to achieve desired reflectance properties by altering the photonic band gap in the structures (Kim et al., 2011).

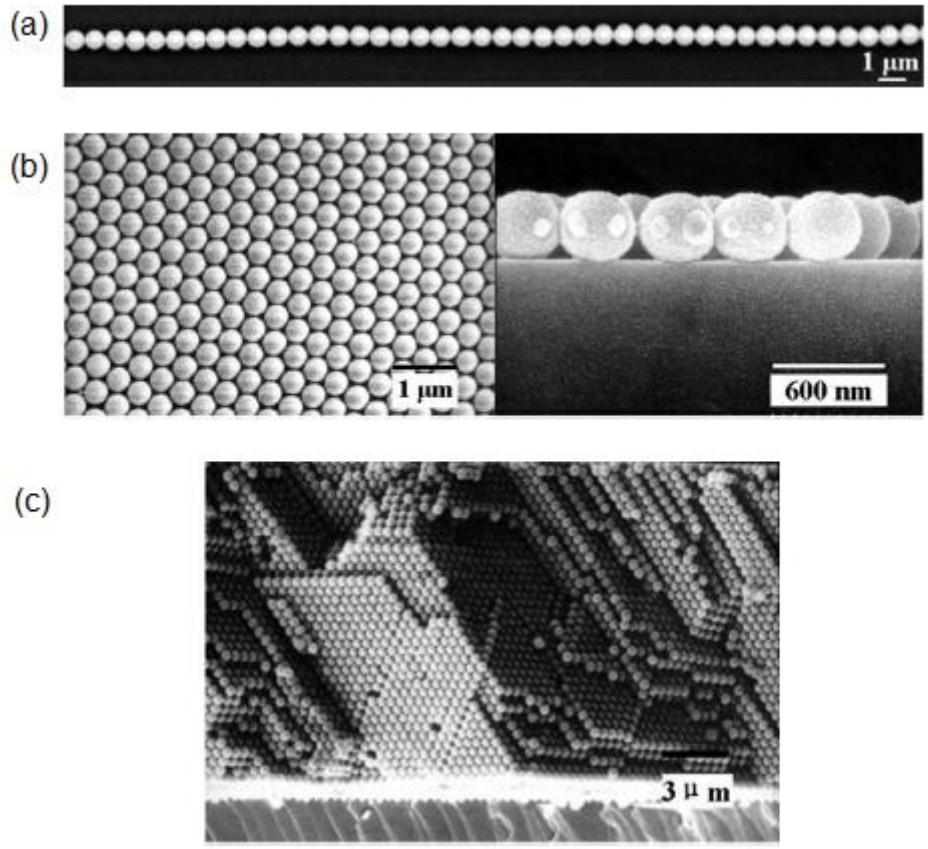

Figure 3.7: Scanning electron microscope images of (a) one-dimensional colloidal crystal, (b) two-dimensional colloidal crystal with cross-section view and (c) three-dimensional colloidal crystal (Tao, Huang and Yang, 2004; Cong and Cao, 2003)

Besides the photonic crystals, the disordered-structure photonic glasses have been investigated as another class of photonic nanostructures that can show unique optical phenomena such as random lasing, long-range intensity

correlations and strong light localization. The photonic glasses have less structural correlation or periodicity, which include topological arrangements with long or short-range correlation but with no full periodicity (Galisteo-López, et al., 2011). Photonic glasses are useful in the manipulation of light diffusion, which can interact strongly with light and hence generate unusual diffusion phenomena including random lasing and angle-independent light localization (Kim, et al., 2011). These photonic nanostructures have been synthesized by monitoring the concentration of calcium chloride in order to destabilize the colloidal particles or by introducing smaller colloid particles (García, Sapienza and López, 2010).

3.4 Summary

This chapter has first given an introduction about the emulsion polymerization technique. The sizes of polymer spheres can be controlled during the emulsion polymerization by adjusting surfactant concentration in the emulsion system. As more surfactant is adsorbed at the oil/water interface, this increases the stability of water interfacial area and hence leading to smaller particle size. After that, this chapter has also explained the working principle of evaporation induced self-assembly technique. The parameters, which include lifting speed and emulsion concentration, may affect the quality of colloidal assembly in the dip coating process. Therefore, these parameters should be carefully controlled and adjusted during the dip coting process in order to obtain a homogenous thin film. The last part of this chapter has introduced the types of colloidal structure including photonic crystal and photonic glass. Photonic crystal can be

categorized further to 1-D, 2-D and 3-D photonic crystal according to their spatial arrangements. Photonic glass has shown a different way in affecting the light transmission compared to photonic crystal. Unique phenomena can be observed between the interactions of photonic glass and light, which include random lasing, long-range intensity correlations and strong light localization.

CHAPTER 4

MATERIALS AND METHODS

4.1 Chemicals

The chemicals used in this project are tabulated in Table 4.1. All chemicals were used as received without further purification.

Table 4.1: List of chemicals

Analytical reagent grade chemical	Source
Acrylic acid	Merck
30% Ammonia solution	Systerm
Gold nanoparticles stabilized by dodecanethiol in toluene, 3-5 nm particle size	Sigma-Aldrich
30% Hydrogen peroxide	Merck
Methyl methacrylate	Daejung
Potassium persulfate	Sigma-Aldrich
Silver nanoparticles stabilized by dodecanethiol in hexane, 3-7 nm particle size	Sigma-Aldrich
Sodium dodecyl sulfate	Systerm
Tetrahydrofuran	Merck

4.2 Instrumentation

The instruments used in this project are listed in Table 4.2.

Table 4.2 List of instruments

Instrument	Brand, Model
Atomic force microscope	Park Systems, XE-70
Dip coater	Tefini, DP1000C
Differential scanning calorimeter	Mettler Toledo, DSC823^e
Energy dispersive X-ray spectrometer	Bruker, XFlash®6-T | 60
Field emission scanning electron microscope	JEOL, JSM-6701F
Fourier transform infrared spectrometer	Perkin Elmer, Spectrum RX I
Multimeter	SEW, ST-3501
Particle size analyzer	Malvern, Mastersizer 2000
Programmable direct circuit electronic load	Array, 3721A
Refractometer	Schmidt & Haensch, AR-12
Thermogravimetric analyzer	Mettler Toledo, TGA/SDTA851^e
Transmission electron microscope	Hitachi, HT-7700
Ultraviolet – visible spectrophotometer	Shimadzu, UV-1700
X-ray diffractometer	Shimadzu, XRD-6000

4.3 Experimental Procedure

4.3.1 Synthesis of P(MMA-*co*-AA) Polymer Nanospheres

Poly(methyl methacrylate-*co*-acrylic acid) nanospheres were synthesized via emulsion polymerization using 95 wt% of methyl methacrylate with 5 wt% of acrylic acid. The polymerization reaction was carried out at the temperature of 75°C using potassium persulfate as the initiator. Sodium dodecyl sulfate (SDS) was used as the surfactant to stabilize the polymer particles in the emulsion. The polymerization was conducted using a five-neck reaction flask. The stirring speed was set at 600 rpm and the reaction time for the polymerization process

was 3 hours. The polymer nanopsheres with various sizes were synthesized by changing the surfactant concentration in the emulsions to 5.3 mM, 10.5 mM, 15.8 mM and 21 mM respectively.

4.3.2 Preparation of Polymer Nanospheres with Embedded Gold Nanoparticles or Silver Nanoparticles

The gold nanoparticles or silver nanoparticles was incorporated into the polymer nanospheres during the polymerization process. The weight percentage of the metal nanoparticles incorporated into the polymer nanospheres was varied in a series of 1.25×10^{-3} wt%, 2.5×10^{-3} wt%, 3.75×10^{-3} wt% and 5×10^{-3} wt%.

4.3.3 Chemical Treatment for Solar Cell Substrate

The method used to treat the surface property of solar cell substrates is a modification of Yoldi's procedure. (Yoldi, et al., 2007) The solar cell substrate was sonicated in a beaker of distilled water for 15 minutes. This cleaning process was repeated with fresh distilled water for another 15 minutes. The substrate was hydrophilized using a mixture of distilled water: 30% ammonia solution: 30% hydrogen peroxide with ratio of 5:1:1, for 30 minutes at 67ºC. Afterwards, the trace amount of chemicals was removed by cleaning the substrate in copious amount of distilled water. Subsequently, the substrate was dried in a vacuum oven at 50 ºC for 30 minutes.

4.3.4 Deposition of Polymer Nanosphere Arrays on Solar Cell Substrate

The self-assembled arrays of polymer nanospheres were fabricated by using a dip coater (Tefini, DP1000C). First, a polymer emulsion with the concentration of 20 mg/ml was prepared by diluting from the emulsion from mother liquor with distilled water in a 100mL of volumetric flask. Afterwards, a solar cell substrate was immersed perpendicularly into the dispersion and drawn up with the speed of 2 μm/s. The humidity and temperature of the environment were measured at around 65% and 25°C, respectively during the experiment.

4.4 Characterization

4.4.1 Total Solids Content

1 g of P(MMA-*co*-AA) emulsion was transferred to aluminum dish and weighed. The sample was then dried in a vacuum oven at 50°C for overnight. After that, the sample was cooled down and the weight was recorded. The processes were repeated until a constant weight was obtained.

4.4.2 Viscometry Measurement and Molecular Weight Determination

The viscosity average molecular weight of P(MMA-*co*-AA) polymer was determined using dilute solution viscometry. A P(MMA-*co*-AA) solution with concentration of 1 g/dL was prepared by adding 0.25 g of P(MMA-*co*-AA) polymer to a 25 mL volumetric flask. The polymer was dissolved in tetrahydrofuran and the solution in the volumetric flask was topped up with

tetrahydrofuran to 25 mL. The flow time of the solvent and the polymer solution was determined by transferring 10 mL of the solvent to an Ubbelohde size OB viscometer. The flow time of the diluted polymer solutions were measured by reducing the concentration of the polymer solution. The polymer solution was diluted consecutively by adding 1mL of solvent each time. The temperature of viscometry water bath was set and maintained at 25°C. The molecular weight of polymer was calculated from the viscosity of polymer solution using the equations as follows:

$$\eta_{rel} = \frac{t}{t_0} \text{ (Eq. 4.1)}$$

where η_{rel} is the relatively viscosity, t is the flow time of polymer solution and t is the flow time of solvent.

$$\eta_{sp} = \eta_{rel} - 1 \text{ (Eq. 4.2)}$$

where η_{sp} refers to the specific viscosity.

$$\eta_{red} = \frac{\eta_{sp}}{c} \text{ (Eq. 4.3)}$$

where η_{red} refers to the reduced viscosity and c represents the concentration of polymer solution.

$$[\eta] = K\bar{M}_v^a \text{ (Eq. 4.4)}$$

where $[\eta]$ is the intrinsic viscosity and $\bar{M}_v$ is the viscosity average molecular weight. The Mark-Houwink constant K and a are 7.5×10^{-5} dL/g and 0.72 respectively (American Polymer Standards Corporation, 2018).

4.4.3 Refractometry

The index of refraction of the P(MMA-*co*-AA) polymer was determined by using an Abbe type refractometer (AR-12, Schmidt & Haensch) at the temperature of 25°C and the wavelength of 589 nm. The polymer film was prepared by dissolving 0.2g of the polymer in 10 mL of chloroform and casting on a Teflon mold. The polymer film was kept in the desiccator with a relative humidity of 50% overnight before the measurement.

4.4.4 Particle Size Analysis

The particle size analysis of the polymer nanospheres was performed using a laser diffraction particle size analyzer (Malvern, Mastersizer 2000). Distilled water was used to dilute the P(MMA-*co*-AA) polymer dispersions. The refractive indexes of water and the polymer were fixed at 1.33 and 1.49 respectively.

4.4.5 Fourier Transform Infrared Spectroscopy

Fourier transform infrared (FTIR) spectroscopy was used to determine the functional groups which presents in the monomer molecules and the polymer chains. FTIR analysis of the monomers used in the emulsion polymerization was conducted using a FTIR spectrometer (Perkin Elmer, Spectrum RX I) equipped with zinc selenide (ZnSe) horizontal attenuated total reflectance accessory. The FTIR spectrum of the solid polymer was obtained using the

potassium bromide (KBr) pellet technique. The pellet was prepared by grinding the solid sample with KBr salt using a mortar and pestle, and then pressed into pellet form with a hydraulic press.

4.4.6 Differential Scanning Calorimetry

The glass transition temperature (T_g) of the P(MMA-*co*-AA) polymer was determined using a differential scanning calorimeter (Mettler Toledo, DSC823^e) under nitrogen atmosphere. About 5 mg of the sample was weighed into a 40 µL aluminum crucible. Then, the sample in the crucible was encapsulated by pressing it with an aluminum lid by using a sealing press. The sample was first heated from 25 to 150ºC with the heating rate of 10ºC/min. Then, the sample was subsequently cooled to 25ºC with the cooling rate of 50 ºC/min. After that, a second round of heating was carried out by heating the sample from 25 to 170ºC at a heating rate of 10 ºC/min. The nitrogen flow rate was set at 20 mL/min.

4.4.7 Thermogravimetric Analysis

The thermal decomposition behavior and the composition content of the polymer was studied using a thermogravimetric analyzer (Mettler Toledo, TGA/SDTA851^e). An amount of 5 mg of sample was placed into a 70 µL alumina crucible. Heating was started from 25 to 700ºC with the heating rate of 20ºC/min and the analysis was conducted in a nitrogen atmosphere. The nitrogen flow rate was set at 20 mL/min.

4.4.8 X-Ray Diffraction Analysis

The crystallinity in the P(MMA-*co*-AA) polymer was studied using X-ray diffraction (XRD) technique. XRD analysis was performed using an X-ray diffractometer (Shimadzu, XRD-6000). The analysis was conducted in a continuous scan mode using copper target at the voltage of 40 KV and the current of 30 mA. The sample was scanned at the speed of 2°/min in the range of 10-60°.

4.4.9 Field Emission Scanning Electron Microscopy

The surface morphology of the polymer nanospheres coated onto a glass substrate was studied by using a field emission scanning electron microscope (JEOL, JSM-6701F) at an accelerating voltage of 2 or 4 KV. The sample was sputtered with a thin layer of platinum before analysis.

4.4.10 Atomic Force Microscopy

An atomic force microscope (Park Systems, XE-70) was used to investigate the surface topology of the sample. The sample was characterized in a non-contact mode. The scan rate was set to 1 Hz with scan size of 4 μm^2.

4.4.11 Transmission Electron Microscopy and Energy Dispersive X-Ray Spectroscopy

The encapsulation of metal nanoparticles into the polymer nanopsheres was determined using a transmission electron microscope (Hitachi, HT-7700) equipped with an energy dispersive X-ray (EDX) spectrometer (Bruker, XFlash®6-T | 60) at an accelerating voltage of 120 KV. The electron microscope was used to identify the metal nanoparticles embedded in the polymer nanospheres and the EDX spectrometer was used to analyze the elements presented in the sample. The sample was prepared by sonicating the polymer dispersion in an ultrasound sonicator for 10 minutes. Then, the polymer dispersion was spread on a lacey copper grid and the sample was dried in an oven at 45 °C for 5 minutes.

4.4.12 Ultraviolet-Visible Spectrophotometry

The analysis was carried out by using an ultraviolet-visible (UV-Vis) spectrophotometer (Shimadzu, UV-1700). The spectrum was acquired in the UV-Vis range of 300-800 nm. In UV-Vis absorption analysis, the sample was prepared by dissolving the polymer nanospheres or dispersing the metallic nanoparticles in acetone or hexane. In the UV-Vis transmission analysis, the sample was prepared by coating a monolayer of nanospheres on the soda lime glass substrate.

4.5 Electrical Measurement

The output power of the solar cell (Sanyo, AM8701CAR) placed under a cool daylight fluorescent lamp (Philips, Tornado) with the intensity of 10 mW/cm^2, was determined using a multimeter (SEW, ST-3501). The dimensions of the solar cell are 58 mm in length and 55 mm in width with thickness of 1.3 mm. The schematic diagram of the configuration of the amorphous silicon solar cell structure is shown in Figure 4.1.

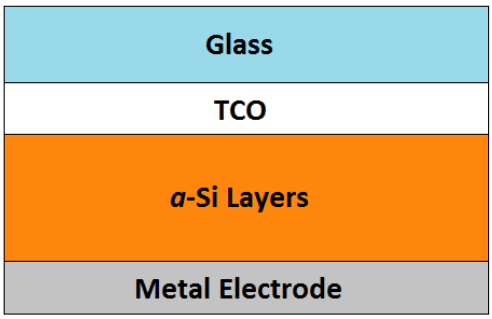

Figure 4.1: Schematic diagram of the structure design of the amorphous silicon solar cell

The distance between fluorescent lamp and solar cell was set at 5 cm. Furthermore, different output powers were measured by tilting the solar cell from 0-90º. The experimental setup is shown in Figure 4.2. The current density-voltage (*J-V*) measurement of the solar cell was conducted using a programmable direct-current electronic load (Array, 3721A) under the illumination of an AM 1.5 solar simulator with the intensity of 100 mW cm^{-2}. The light exposure area in the both experiments was set to 9 cm^2.

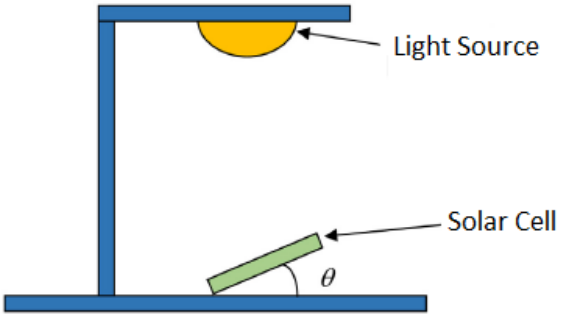

Figure 4.2: Schematic diagram of the experimental setup of measuring the power generated by solar cell tilted at different angles of θ

4.6 Summary

In summary, this chapter has introduced the methods used for the preparation and characterization of the polymer nanospheres and the nanospheres embedded with gold or silver nanoparticles. The characterization includes total solids content, refractometry, particle size analysis, Fourier transform infrared analysis, differential scanning calorimetric analysis, thermogravimetric analysis, X-ray diffraction analysis, atomic for microscopy, field-emission scanning electron microscopy, transmission electron microscopy, energy dispersive X-ray analysis and UV-Vis spectrophotometry. Furthermore, this chapter has also presented the technique used to deposit polymer nanosphere array onto solar cell and followed by its characterization. The last part of this chapter has explained the experiment design used for the electrical measurement of solar cell.

CHAPTER 5

SYNTHESIS AND CHARACTERIZATION OF P(MMA-*CO*-AA) POLYMER NANOSPHERES AND NANOSPHERES EMBEDDED WITH METALLIC NANOPARTICLES COATED ON SOLAR CELL

5.1 Physical Properties of P(MMA-*co*-AA) Polymer

The poly(methyl methacrylate-*co*-acrylic acid), P(MMA-*co*-AA), polymer emulsions were obtained as milky white liquid. The total solids content and the percentage of conversion of the polymer emulsions with different concentration of sodium dodecyl sulfate (SDS) used are tabulated in Table 5.1. The table indicates that the total solids content of the polymer emulsions is around 18-19%. The theoretical total solids content of the polymer dispersions is 21%. The results show high monomer conversion of around 87-92% in the polymerization process and hence high percentage yield of the polymer. The viscosity-average molecular weight of P(MMA-*co*-AA) polymer determined using diluted solution viscometry is 811430 g/mol. The calculation for viscosity-average molecular weight has been attached in the Appendix A. Viscosity-average molecular weight is usually used as close estimation of weight-average molecular weight. This is because they are commonly quite close with percentage difference within 10-20% (Odian, 2004). Therefore, the estimated weight-average molecular weight of P(MMA-*co*-AA) polymer is around 1×10^6 g/mol. In addition, the P(MMA-*co*-AA) polymer exhibits a refractive index of 1.494 at 25°C.

Table 5.1: Total solids content and monomer conversion of the polymer emulsions with different surfactant concentration

Concentration of SDS Used (mM)	Total Solids Content (%)	Monomer Conversion (%)
5.3	18.3	87.0
10.5	19.0	90.7
15.8	19.6	93.2
21.0	19.4	92.2

In the P(MMA-*co*-AA) polymer, the methyl methacrylate components were used to obtain a matrix with high optical transparency to visible and ultraviolet light . Moreover, the introduction of acrylic acid segments into the polymer chain might enhance the wetting properties of the polymer nanospheres. (Lee et al., 2018) This could improve the adhesion of the polymer nanopsheres to the solar cell substrate. Consequently, the unique combination of both optical and mechanical properties demonstrated by this polyacrylate polymer would give an outstanding benefit for the polymer to be produced as the polymer-based light trapping nanopaheres (Lee et al., 2018).

5.2 Characterization of P(MMA-*co*-AA) Polymer Nanospheres

The P(MMA-*co*-AA) polymer nanospheres with various sizes prepared through altering the concentration of SDS in the emulsion polymerization process will be discussed in the this section. The structural information of P(MMA-*co*-AA) polymer chains will be discussed in infrared spectroscopic study. In addition, the thermal stability of the polymer nanospheres over a wide temperature range will be discussed under thermogravimetry and differential scanning calorimetry sections. Lastly, the structural order of P(MMA-*co*-AA) polymer acquired through X-ray diffraction technique will be reported and explained.

5.2.1 Particle Size Measurement

The particle sizes of the P(MMA-*co*-AA) polymer nanospheres were measured using laser diffraction technique. The mean particle sizes of the polymer nanospheres were calculated based on the De Brouckere mean or volume weighted mean. Figure 5.1 illustrates that different particle sizes (i.e. 156 nm, 122 nm, 101 nm and 97 nm) could be obtained by altering the concentration of SDS. Moreover, a quadratic relationship between the function of the surfactant concentration and the mean particle size was observed in the figure. The mean particle size of the polymer nanospheres decreases from 156 nm to 97 nm as the concentration of SDS is increased from 5.3 mM to 21 mM.

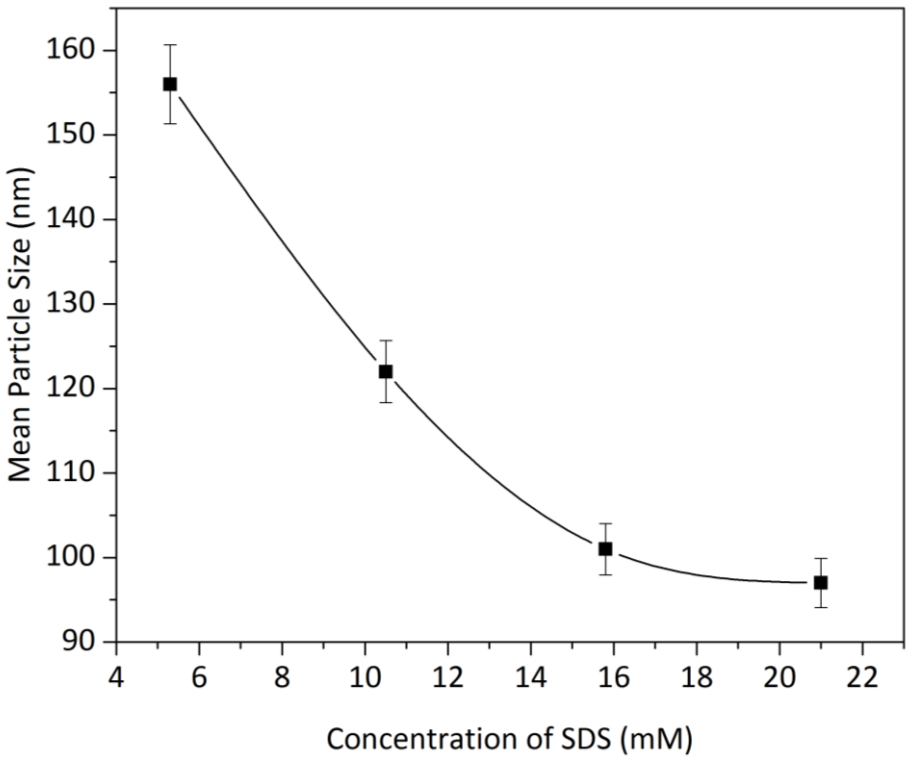

Figure 5.1: Mean particle sizes of the P(MMA-*co*-AA) polymer nanospheres as a function of the SDS concentration

Nevertheless, the particle size has started to achieve a plateau as the surfactant concentration in the emulsion system surpasses the amount of 15.8 mM. In fact, Rowe has reported a similar pattern that increasing the concentration of surfactant would cause a decrease in the particle size (Rowe, 1965). This is because increasing surfactant concentration will result in a greater adsorption of surfactant at the water interface. This increases the stability of water interfacial area and hence leading to smaller particle size (Rowe, 1965).

Table 5.2 shows the mean particle sizes (i.e. 156 nm, 122 nm, 101 nm and 97 nm) and the particle-size distribution of the nanospheres with different surfactant concentration. As mentioned previously, increasing surfactant concentration in the emulsion system could result in the nanospheres with smaller size. Furthermore, increasing surfactant concentration will also lead to the increase in the polydispersity of nanospheres. When the concentration of SDS increasing from 5.3 mM to 21 mM, a significant increase in the span and hence the polydispersity of the particle-size distribution was observed.

Table 5.2: The mean particle sizes and particle-size distribution of the polymer nanospheres obtained by varying the concentration of SDS

Concentration of SDS used (mM)	Mean Particle Size (nm)	Particle Size Distribution (nm)			
		D_{10}	D_{50}	D_{90}	Span
5.3	156	138	156	175	0.234
10.5	122	85	120	163	0.651
15.8	101	66	96	141	0.786
21.0	97	62	93	138	0.819

Besides that, the increase of polydispersity will cause a broader particle-size distribution. In Figure 5.2, The sizes of polymer nanospheres with surfactant

concentration of 5.3 mM are more uniformly distributed as compared to the nanospheres with other surfactant concentration. The particle-size distribution was characterised by a sharp peak and narrow distributed particle sizes. The polymer nanospheres with surfactant concentration of 21 mM possess the widest range of particle-size distribution from 46 nm to 182 nm. Consequently, the surfactant concentration plays an important role in determining the particle size and polydispersity of nanospheres.

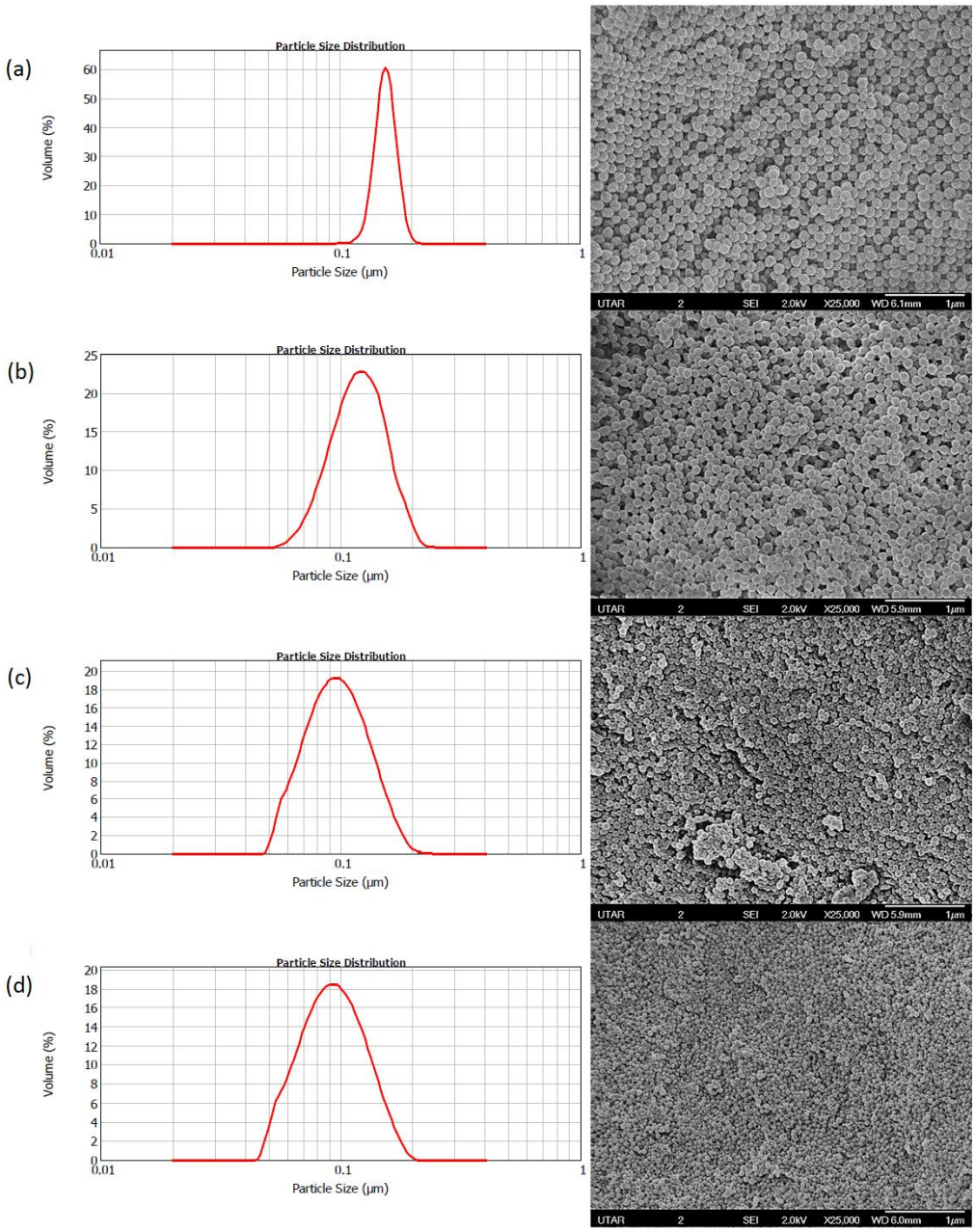

Figure 5.2: Particle-size distribution and scanning electron microscope images of the P(MMA-*co*-AA) polymer nanospheres with surfactant concentration of (a) 5.3 mM, (b) 10.5 mM, (c) 15.8 mM and (d) 21 mM

5.2.2 Fourier Transform Infrared Analysis

The Fourier transform infrared (FTIR) analysis was performed on the P(MMA-*co*-AA) polymer, the methyl methacrylate and acrylic acid monomers. The FTIR spectrum of the polymer and monomers were acquired in the range of

4000-600 cm^{-1}. The FTIR spectrum of the polymer, the methyl methacrylate and acrylic acid monomers are illustrated in Figure 5.3. The Table 5.3 shows the wavenumber and its corresponding vibration mode for the functional groups in the polymer and monomers.

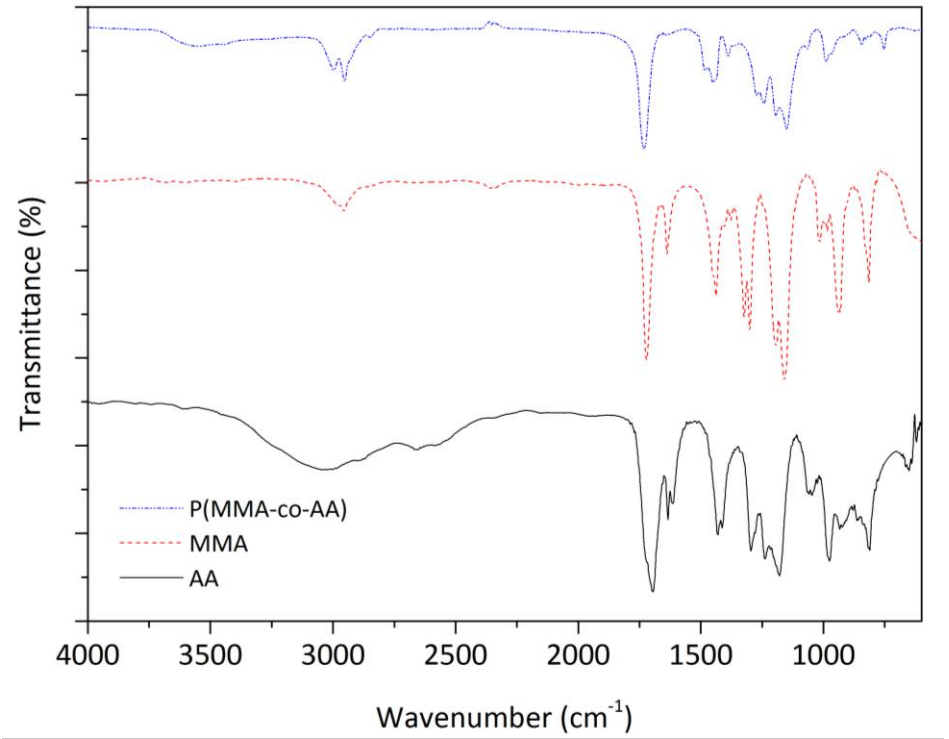

Figure 5.3: FTIR spectrum of the P(MMA-*co*-AA) polymer, the methyl methacrylate and acrylic acid monomers

In the FTIR spectrum of the P(MMA-*co*-AA) polymer , the broad band shown at the region between 3700 cm^{-1} and 3478 cm^{-1} was assigned to the stretching mode of the water absorbed by the polymer. The absorption peak at 2996 cm^{-1}, which partially overlaps with the sp^3 C-H absorption at 2996 cm^{-1}, is due to the O-H stretch of the carboxylic acid moiety in the polymer chains.

By interpreting the FTIR spectrum of the two monomers, they exhibit a broad O-H absorption at 3013 cm^{-1} and a sp^3 C-H absorption at 2954 cm^{-1}, respectively.

Therefore, the O-H and sp^3 C-H absorption are contributed by the acrylic acid and methyl methacrylate components in the P(MMA-*co*-AA) polymer chains respectively.

Table 5.3: FTIR spectrum interpretation of the P(MMA-*co*-AA) polymer, the methyl methacrylate and acrylic acid monomers

	Wavenumber (cm^{-1})	Vibration Mode
P(MMA-*co*-AA)	3700-3478	O-H stretch (water)
	2996	O-H stretch (carboxylic acid)
	2955	sp^3 C-H stretch
	1733	C=O stretch
	1241	C-O stretch
Methyl methacrylate	2954	sp^3 C-H stretch
	1719	C=O stretch
	1635	C=C stretch
	1299	C-O stretch
Acrylic acid	3013	O-H stretch (carboxylic acid)
	1696	C=O stretch
	1635	C=C stretch
	1298	C-O stretch

Furthermore, the strong absorption peak at 1733 cm^{-1} in the FTIR spectrum of the P(MMA-*co*-AA) polymer is contributed by the C=O stretching vibration from both of the methyl methacrylate and acrylic acid repeating units in the polymer chains. The carbonyl moieties of the polymer chains vibrate at slightly higher wavenumber than that of the monomers. The absorption peak observed at 1241 cm^{-1} in the FTIR spectrum of P(MMA-*co*-AA) are resulted from the C-O stretching vibrations of the two repeating units in the polymer chains. In contrast, the C-O stretch of the P(MMA-*co*-AA) polymer shows a higher shift in wavenumber than that of the monomers. The shift in the wavenumber of these functional groups could be due to the different chemical environment in the

monomers and the polymer chains. The disappearance of the C=C stretch at 1635 cm^{-1} in the FTIR spectrum of P(MMA-*co*-AA) polymer was observed as compared to the spectrum of the monomers. This shows that the copolymerization process has been achieved by breaking of double bonds in the methyl methacrylate and acrylic acid monomers (Mohy, et al., 2017).

5.2.3 Differential Scanning Calorimetry

The glass transition temperature (T_g) of P(MMA-*co*-AA) polymer with different surfactant concentration was studied through the differential calorimetry technique. Figure 5.4 shows the differential scanning calorimetry (DSC) thermograms of the P(MMA-*co*-AA) polymer nanospheres. The observed T_g from the thermograms are presented in Table 5.4. The T_g is defined as the mid-point on the thermal curve corresponding to half of the heat flow difference between the extrapolated onset and extrapolated end-set when a polymer transforms from a glassy state to a rubbery state (ASTM E1356-91, 1991). When the polymer is heated to a certain temperature, the polymer chains achieve larger mobility and hence the polymer becomes soft and elastomeric. As shown in Table 5.4, the polymer nanospheres have a T_g value in the range of 111-115°C. In comparison, the P(MMA-*co*-AA) copolymer has a higher average T_g value than the poly(methyl methacrylate) homopolymer which shows a T_g at 108°C (Porter and Blum, 2000). The increase of T_g could be caused by the introduction of acrylic acid segments into the polymer chains. The carboxylic acid group of the acrylic acid leads to higher secondary attractive forces among the polymer chains. Thus, this limits the free rotation of the polymer chains during glass

transition process. The T_g values reveal that the polymer nanospheres coated on the solar cell will not deform due to high temperature after a prolonged exposure to sunlight.

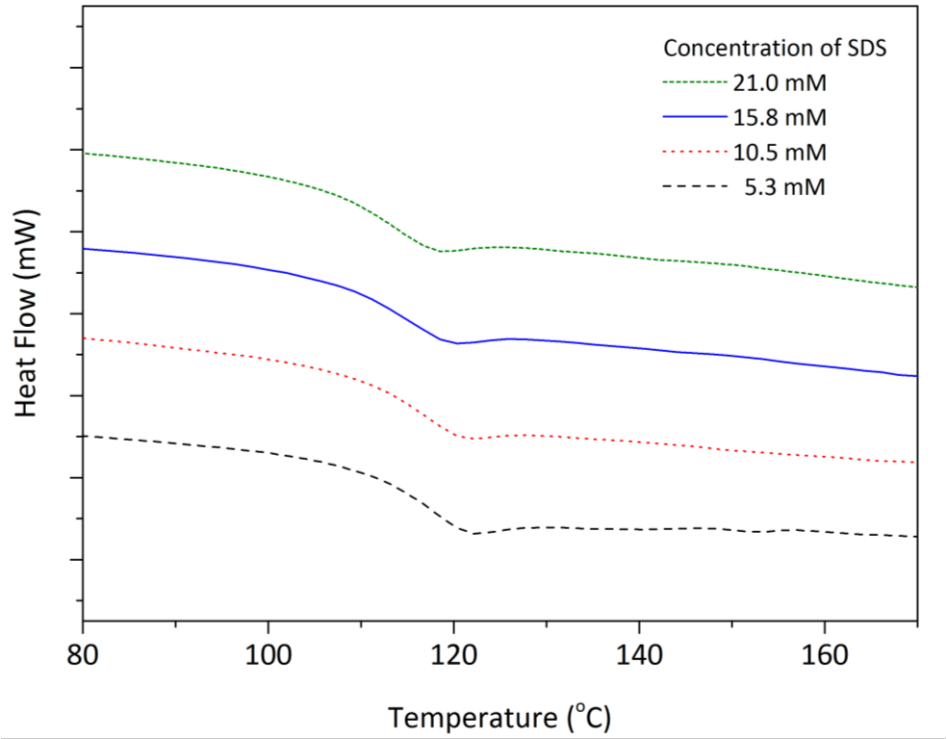

Figure 5.4: DSC thermograms of the polymer nanospheres synthesized using different concentration of SDS

Besides that, increasing SDS concentration could affect the glass transition temperature of polymer. Figure 5.4 illustrates the T_g shifted to the left with gradually increase of SDS concentration. Table 5.4 shows the T_g values of the polymer decreasing from 115.19°C to 110.86°C with increasing SDS concentration from 5.3 mM to 21 mM. The decrease of T_g could be due to the plasticizing effect induced by the anionic SDS surfactant which consists of hydrophobic hydrocarbon tail attached to a sulfate group. The hydrophobic tail which acts as a plasticizer between the polymer chains, causing the decrease in T_g value. Higher amount of the surfactant will increase the fluidity of the

polymer chains and hence the energy barrier for the polymer to transform from glassy state into rubbery state decreases, resulting in the decrease of T_g.

Table 5.4: Glass transition temperature of the P(MMA-*co*-AA) nanospheres synthesized using various concentration of SDS

Concentration of SDS Used (mM)	Glass Transition Temperature (°C)
5.3	115.19
10.5	114.87
15.8	111.66
21.0	110.86

5.2.4 Thermogravimetric Analysis

Thermogravimetric analysis (TGA) and Differential thermogravimetry (DTG) were used to investigate the thermal stability of P(MMA-*co*-AA) polymer. The TGA and DTG thermograms of the P(MMA-*co*-AA) polymer is illustrated in Figure 5.5. A 2% weight loss observed below 100°C in the TGA thermogram is caused by the release of water bound to the polymer chains (El-Zaher, Melegy and Guirguis, 2014). In fact, the PMMA is rather hygroscopic, which can absorb about 2 wt% of water moisture (Kobayashi and Müllen, 2015). Therefore, the methyl methacrylate segments in the polymer chains could contribute the water content.

The thermal decomposition of P(MMA-*co*-AA) polymer is a two-stage process. The first stage of decomposition begun at 150°C in the TGA thermogram was assigned to the breakdown of the carboxylic acid group of acrylic acid repeating units in the polymer chains. The dehydration and the subsequent decarboxylation of the carboxylic acid group were involved in the

decomposition process (McNeill and Sadeghi, 1990). A 3% weight loss observed in the TGA curve at the mid-point of 190°C is resulted from the release of carbon dioxide and water during the decomposition process.

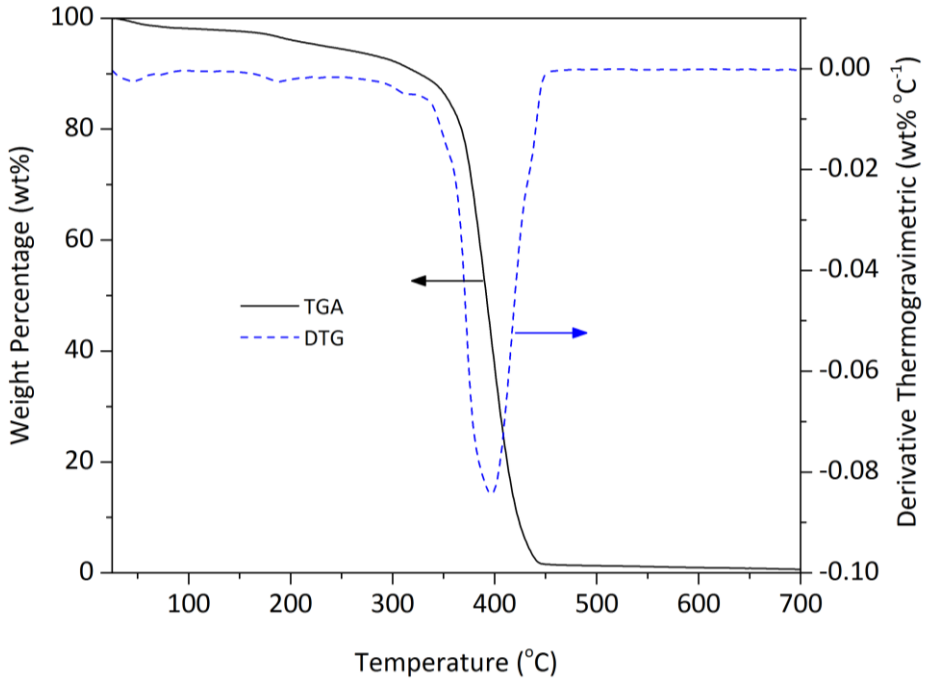

Figure 5.5: TGA and DTG thermogram of the P(MMA-*co*-AA) polymer

In the second stage of decomposition, 93% of weight loss happened at the mid-point temperature of 395°C beside an onset temperature at 252°C. This weight loss was assigned to the chain scission of the polymer chains (Grassie, 1956). In addition, a corresponding sharp endothermic peak at 395°C was observed in the DTG curve. The synthesized polymer was found to have higher decomposition temperature in the thermal degradation of the polymer chains as compared to that of poly(methyl methacrylate) happened at 343-348°C (McNeill and Sadeghi, 1990). The presence of the acrylic acid components in the polymer chains might could enhance the interaction among the polymeric

chains. This results in increasing thermal stability of the polymer chains. (Shanti, et al., 2016) In the end, 96 wt% of the polymer was thermally degraded at 500°C with an approximate 2% of residues left.

5.2.5 X-ray Diffraction Analysis

Figure 5.2 shows the diffactrogram of the P(MMA-*co*-AA) polymer, which is characterised by an intense and broad peak at the angle of 2θ = 14.80° as well as other three signals at 2θ = 34.79°, 38.69° and 44.95°. The diffactrogram provides the information about the crystallinity or structural order of P(MMA-*co*-AA) polymer. The presence of broad peak at 2θ = 14.80° indicates that the P(MMA-*co*-AA) polymer is amorphous in nature. According to Bragg's law, the diffraction peak is sharp and showing a distinct value of the diffraction angle for a crystalline material (Todica, et al., 2014). However, the diffraction peak is broad and consists of individual lines in an amorphous system such as polymeric materials (Todica, et al., 2014). According to the results reported by Mohy et al., three characteristic peaks were observed at 2θ = 14.8°, 38° and 44° in the diffactrogram of poly(methyl methacrylate) polymer (Mohy, et al., 2017). Thus, the peaks at 2θ = 38.69° and 44.95° could be contributed by the methyl methacrylate segments in the polymer chains. Besides that, the diffactrogram of the poly(acrylic acid) is characterised by a relatively strong and broad peak at 2θ = 17.2° and a signal at 2θ = 35° (Todica, et al., 2014). Therefore, the peak appeared at 2θ = 34.79° in the diffactrogram could be attributed to the acrylic acid components in the polymer chains.

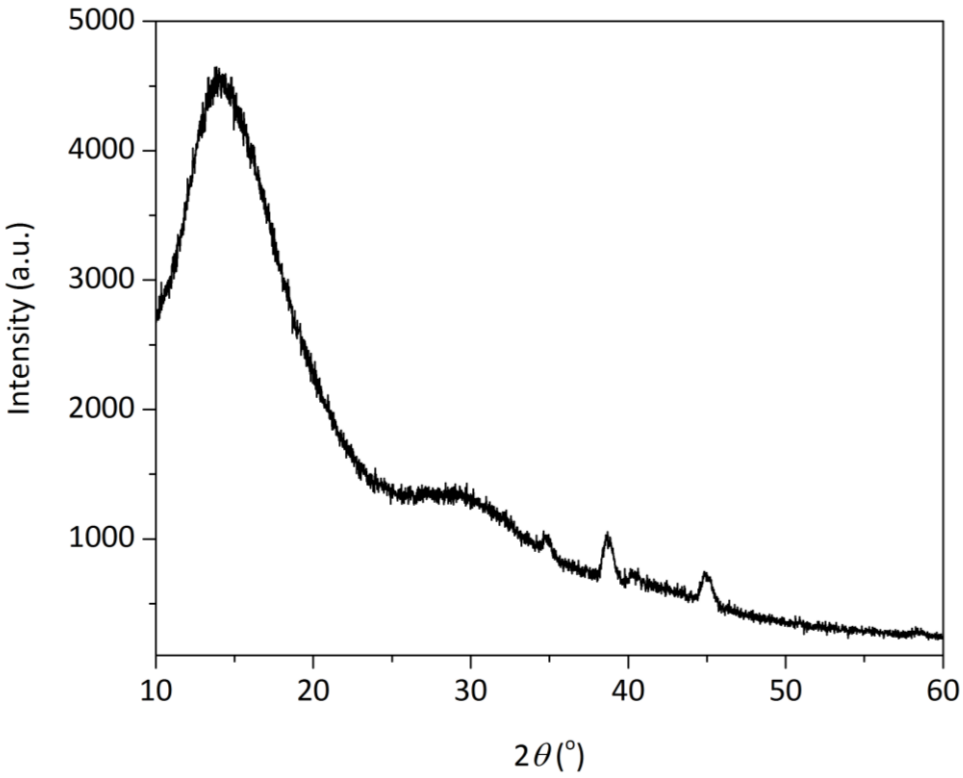

Figure 5.6: XRD diffactrogram of the P(MMA-*co*-AA) polymer

5.3 Development of P(MMA-*co*-AA) Polymer Nanosphere Arrays on Solar Cell Substrate

In this study, the P(MMA-*co*-AA) nanosphere arrays were developed on soda-lime glass substrate by using the dip-coating technique. In order to obtain a good quality self-assembled structure, it is very important to ensure that the glass surface is clean and having good contact with water. Therefore, the substrate was went through chemical treatment prior to the coating process. This treatment effectively removes the organic and inorganic contaminants adsorbed on the glass surface. Moreover, this treatment also improves the wettability of glass substrate by water due to the adsorption of hydrophilic radical on glass surface during the cleaning process (Haugan, 2011).

In the coating process, a clean substrate was dipped perpendicularly into the polymer emulsion and subsequently drawn up with a constant speed of 2 μm/s. As the substrate was drawn from the polymer emulsion, a meniscus region was formed on the glass surface due to the capillary force. The self-assembly process involves the transfer and accumulation of nanospheres in the meniscus to the interface formed among air, emulsion and substrate (Liu, et al., 2006). The concentration of the polymer emulsion was varied from 5 to 20 mg/mL in order to obtain a coating layer with full covering by the polymer nanospheres. Figure 5.7 (a) to (d) show the field emission scanning electron microscope (FESEM) images of the self-assembled nanostructure using different emulsion concentration. Larger area of the nanosphere array was observed with increasing emulsion concentration. In fact, the self-assembly of nanospheres can be affected by the number of nanospheres transferred in the meniscus to the interface during solvent evaporation.

Figure 5.7(a) to (c) show the FESEM images of the polymer nanosphere array prepared using the emulsion concentration of 5 mg/mL, 10 mg/mL and 15 mg/mL. At the concentration of 5 mg/mL, a few small areas of aggregated nanospheres were formed on the substrate due to the low concentration of nanospheres available in the emulsion. Figure 5(c) illustrates that there is an increase in the area and packing density of nanosphere array as the concentration increased to 15 mg/mL. This is because more nanospheres are transferred in the meniscus to the interface during the self-assembly process. Figure 5(d) demonstrates that the substrate with full covering of nanosphere array was obtained with the emulsion concentration of 20 mg/mL. However,

further increasing the emulsion concentration could lead to the formation of multilayer nanosphere array. In Figure 5.8, a multilayer self-assembled structure was observed with the emulsion concentration of 25 mg/mL.

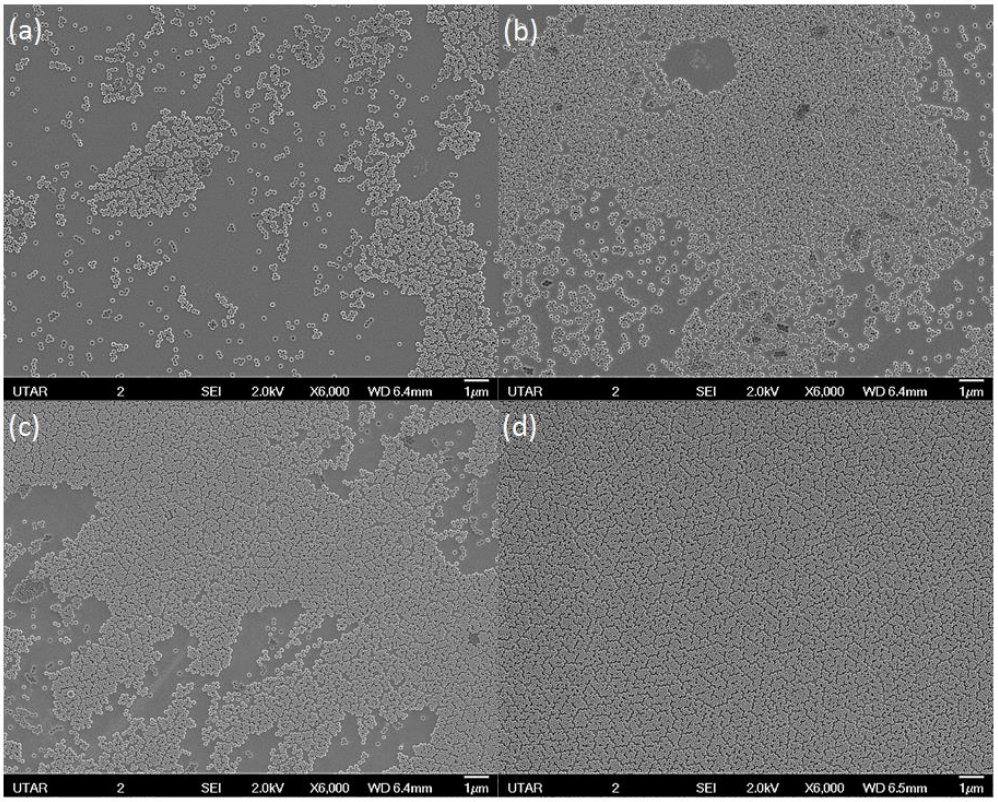

Figure 5.7: FESEM images of the self-assembled array prepared using 156 nm P(MMA-*co*-AA) nanospheres with various concentration of (a) 5 mg/mL, (b) 10 mg/mL, (c) 15 mg/mL and (d) 20 mg/mL

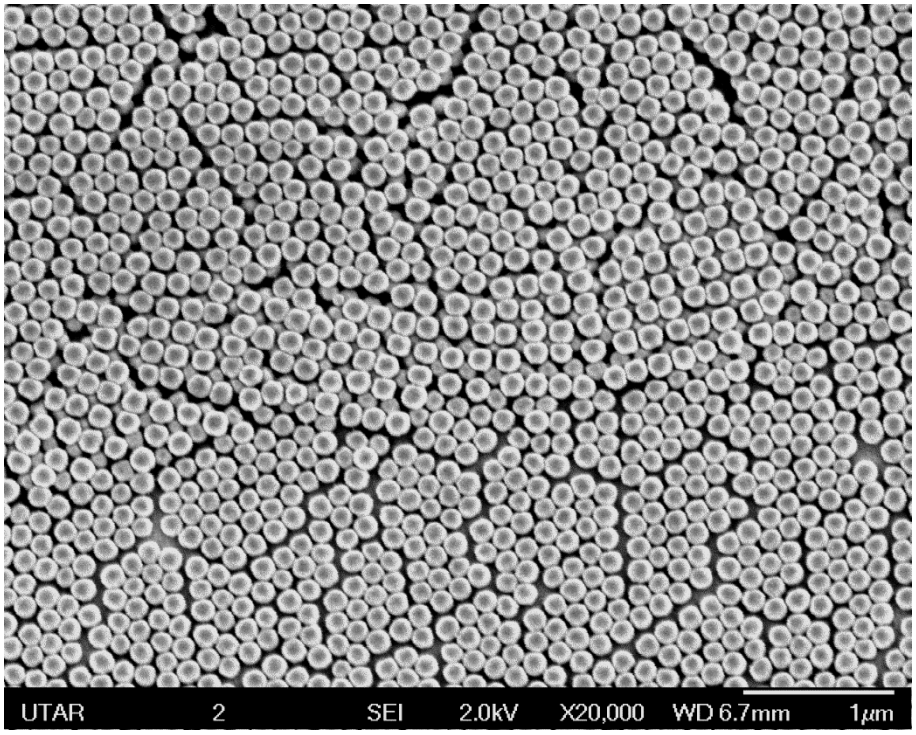

Figure 5.8: FESEM image of the 156 nm P(MMA-*co*-AA) nanosphere thin film fabricated using the emulsion concentration of 25 mg/mL

The polymer nanospheres with other sizes of 122 nm, 101 nm and 97 nm were deposited onto the glass substrate by using the same conditions mentioned previously. Figure 5.9 (a) and (b) illustrates the close-packed nanosphere arrays with average size of 156 nm and 122 nm, respectively. Both of the FESEM images show the ordered packing of self-assembled nanosphere array. Figure 5.9 (c) shows the non-ordered arrangement of self-assembled nanostructure. The non-ordered arrangement of self-assembled array could be due to the polydispersity of the nanospheres (Jiang, et al., 1999). In Figure 5.9 (d), the defects and voids observed in the FESEM image of the nanostructure could be resulted from the excessive amount of surfactant in the emulsion. The excessive amount of the surfactant prevents the agglomeration of the polymer nanospheres in the self-assembly process due to the electrostatic repulsion.

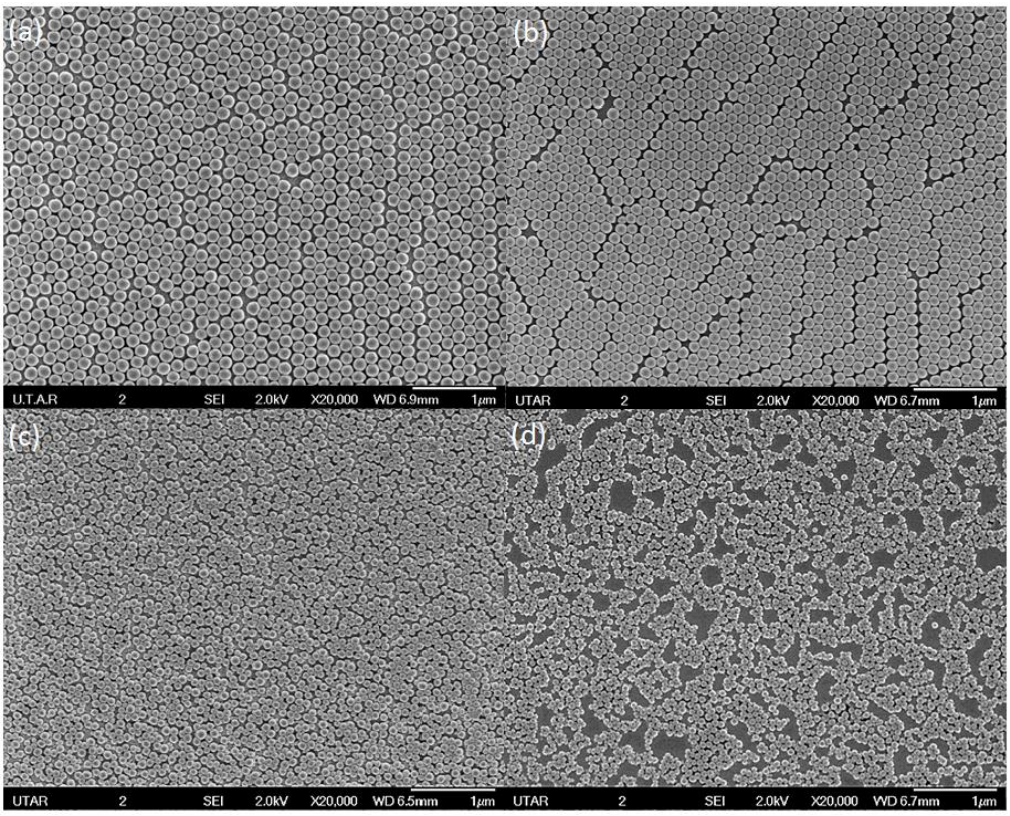

Figure 5.9: FESEM images of the self-assembled layer consist of the polymer nanospheres with average size of (a) 156 nm, (b) 122 nm, (c) 101 nm and (d) 97 nm

The nanostructure fabricated using the emulsion concentration of 20 mg/mL was believed to exhibit monolayer thickness. As shown in Figure 5.9(a) and (b), the nanosphere array with average particle size of 156 nm and 122 nm exhibit the similar surface morphology. Figure 5.10(a) demonstrates the monolayer of such nanostructure. The nanosphere array with average size of 101 nm was found to be with partial double layer as shown in Figure 5.10 (b).

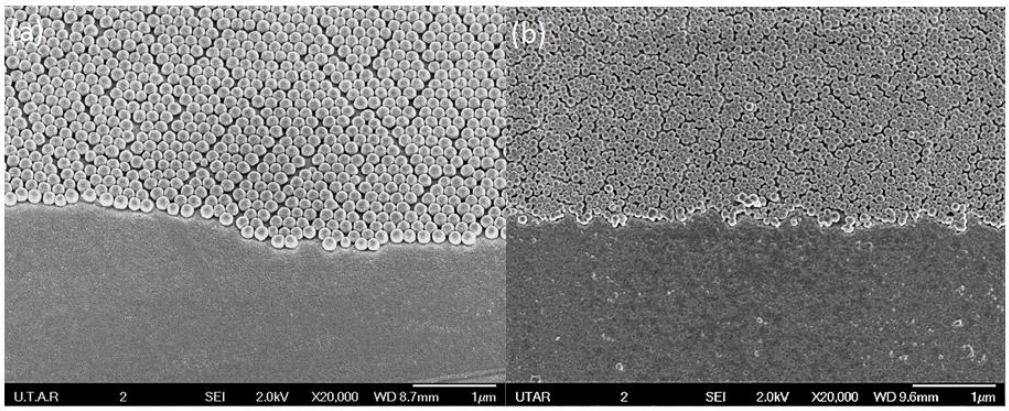

Figure 5.10: Tilted FESEM images of the nanosphere array with average size of (a) 156 nm and (b) 101 nm

Figure 5.11 presents the atomic force microscope (AFM) images of the polymer nanosphere array with different particle sizes. Hexagonal close-packed nanostructure (i.e. with average size of 156 nm) was noticed in the AFM image of Figure 5.11 (a), in which the sphere touching six others in one layer. In Figure 5.11 (b) and (c), closed-packed pattern was found in the AFM images of the nanosphere array with average size of 122 nm and 101 nm.

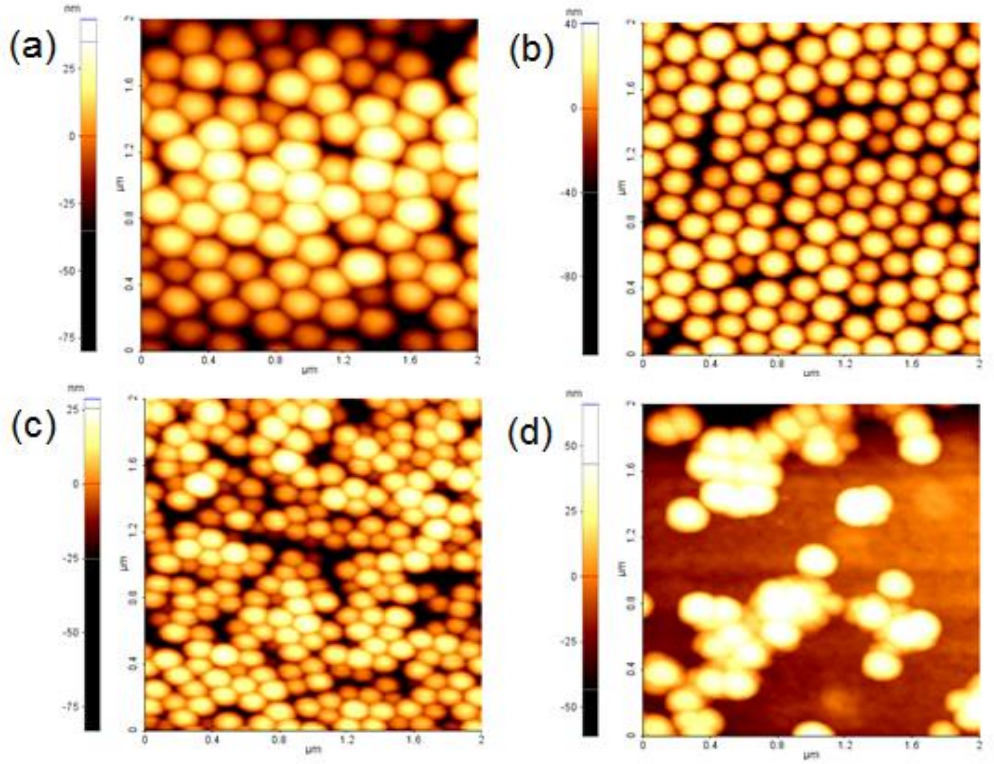

Figure 5.11: Top view of AFM images of the polymer nanosphere array with average size of (a) 156 nm, (b) 122 nm, (c) 101 nm and (d) 97 nm

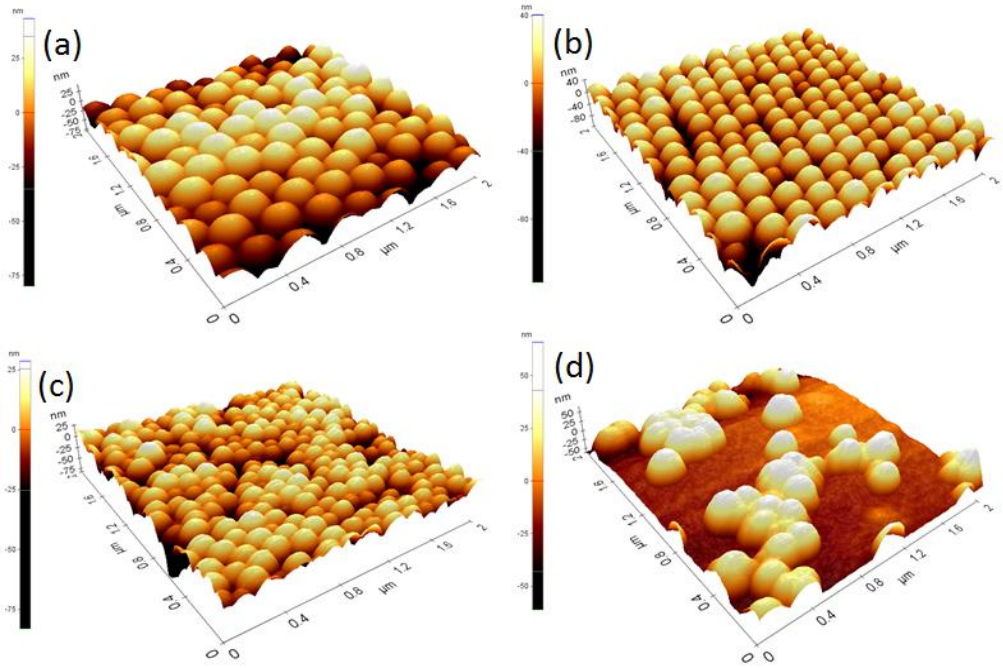

Figure 5.12: Side view of AFM images of the polymer nanosphere array with average size of (a) 156 nm, (b) 122 nm, (c) 101 nm and (d) 97 nm

Figure 5.12(a) to (d) show the topology of the polymer nanosphere arrays with average size of 156 nm, 122 nm, 101 nm and 97 nm. The self-assembled arrays were observed generally to exhibit dome-shape topology. Figure 5.13 shows the line profile of the nanosphere array with different particle sizes measured using AFM. Figure 5.13(a) indicates that the thin film possesses a maximum thickness of 193 nm with the nanospheres of average size of 156 nm. As observed in Figure 5.13(b) and (c), the maximum thickness of the thin films is 164 nm and 92 nm with the nanospheres of 122 nm and 101 nm average sizes, respectively.

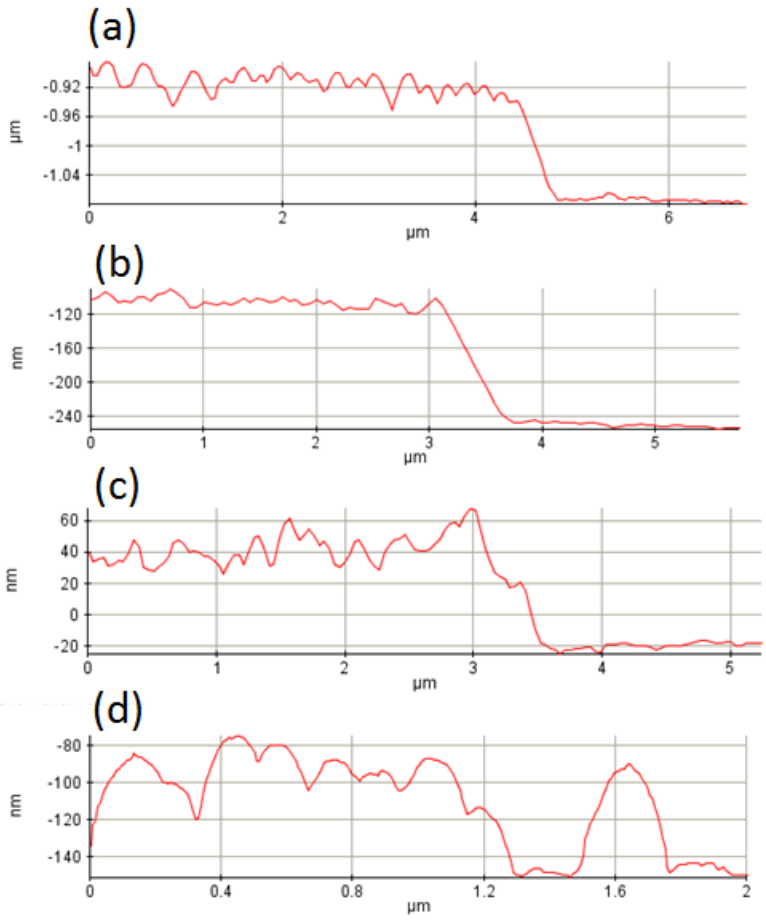

Figure 5.13: Line profile of the P(MMA-*co*-AA) nanosphere array with average size of (a) 156 nm, (b) 122 nm, (c) 101 nm and (d) 97 nm

5.4 Characterization of P(MMA-*co*-AA) Polymer Nanospheres Encapsulated with Metallic Nanoparticles

The light trapping efficiency of the polymer nanospheres with average size of 101 nm could be enhanced by incorporating metallic nanoparticles into the nanospheres. Further discussion about the light trapping efficiency of the nanosphere array with average size of 101 nm will be presented in the Chapter 6. The polymer nanospheres embedded with the metallic nanoparticles were characterized using transmission electron microscope (TEM) coupled with energy dispersive X-ray (EDX) detector.

5.4.1 P(MMA-*co*-AA) Polymer Nanospheres Embedded with Gold Nanoparticles

The presence of gold nanoparticles in the polymer nanospheres was observed using the TEM. Besides that, the gold element was identified using EDX technique. The TEM image in Figure 5.14(a) shows the distribution of the gold nanoparticles inside the polymer nanospheres. The particle size measurement of the gold nanoparticles was provided in Figure 5.14(b). The size of the gold nanoparticles is 3-5 nm. Figure 5.15 shows the result of the elemental analysis of the polymer nanospheres embedded with gold nanoparticles. The existence of the gold (Au) element in the nanospheres was confirmed through the Au signal appeared in the EDX spectrum. The copper peak observed in the spectrum is resulted from the copper grid used in preparing the sample for EDX analysis.

(a)

(b)

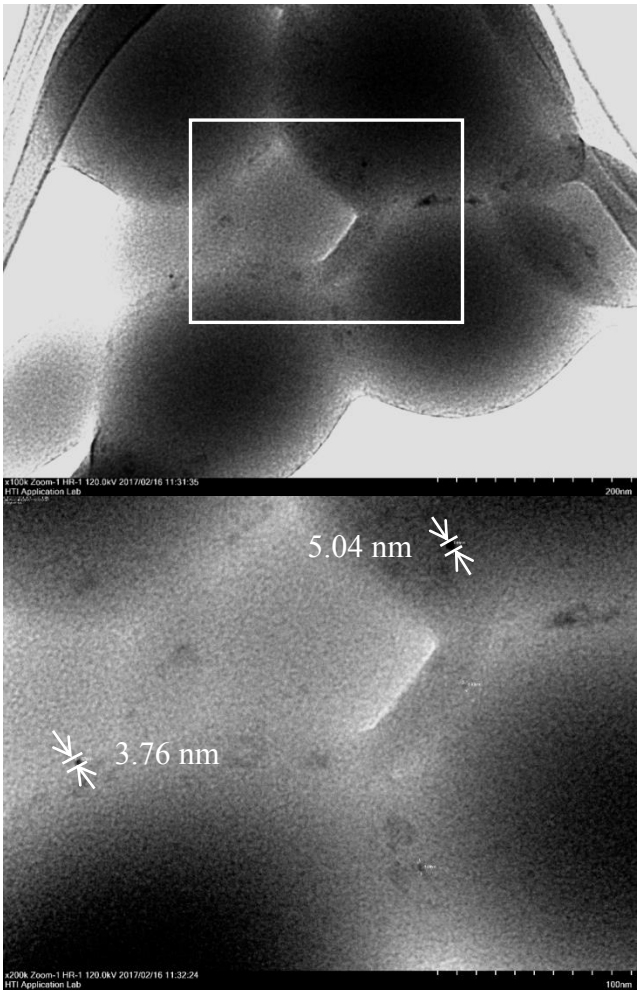

Figure 5.14: (a) TEM image of the polymer nanospheres incorporated with the gold nanoparticles; (b) Magnified image of the part highlighted in TEM image and the particle size measurement of gold nanoparticles

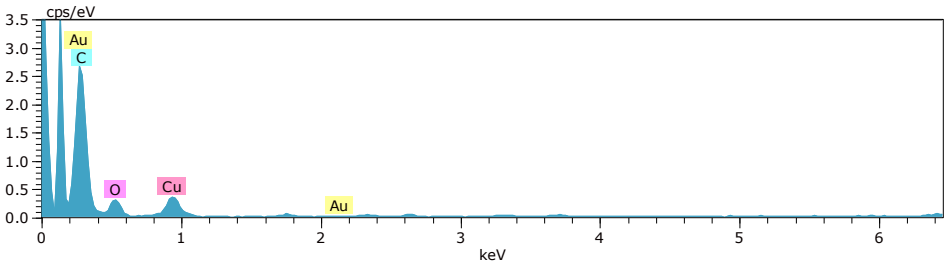

Figure 5.15: EDX spectrum of the polymer nanospheres embedded with gold nanoparticles

5.4.2 P(MMA-*co*-AA) Polymer Nanospheres Encapsulated with Silver Nanoparticles

Figure 5.15 (a) demonstrates the TEM image of fused polymer nanospheres encapsulated with silver nanoparticles. The TEM image in Figure 5.15 (b) shows that the silver nanoparticles exhibit the particle size of 5-7 nm. In Figure 5.16, the EDX spectrum shows the presence of the silver (Ag) element in the fused nanospheres. The potassium element observed in the spectrum could be due to the potassium persulfate used in the polymerization process. The carbon and oxygen elements observed in the spectrum are contributed by the P(MMA-*co*-AA) polymer chains.

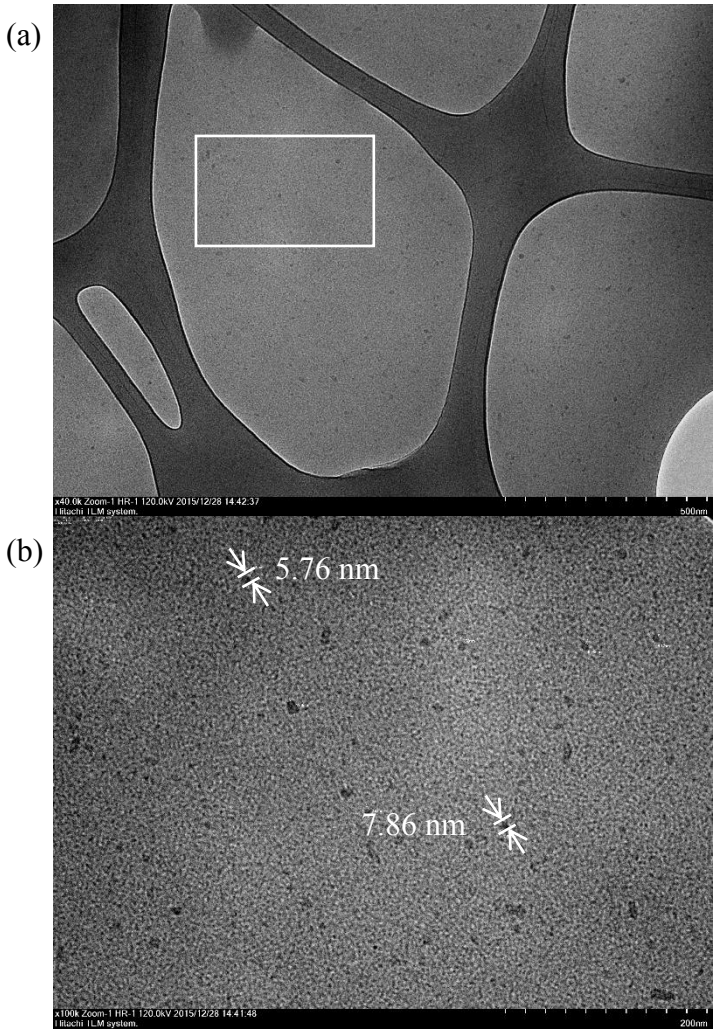

Figure 5.16: (a) TEM image of fused polymer nanospheres with silver nanoparticles; (b) Magnified image of the part highlighted in the TEM image and the particle size measurement of silver nanoparticles

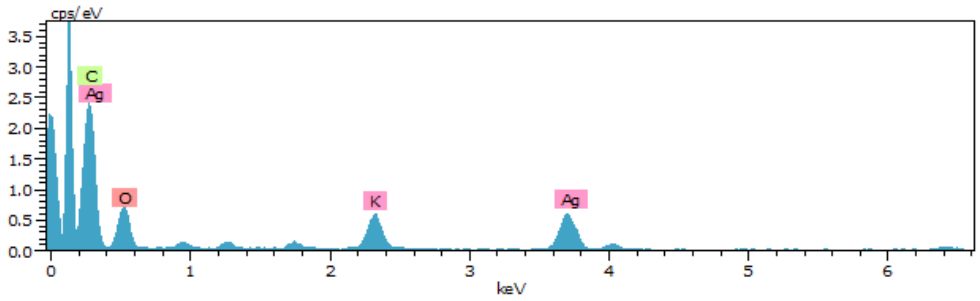

Figure 5.17: EDX spectrum of the fused polymer nanospheres with silver nanoparticles

5.5 Summary

In summary, P(MMA-*co*-AA) polymer nanospheres with different particle sizes ranging from 97 nm to 156 nm were synthesized and coated on the amorphous silicon solar cell substrate. The solar cell sized 58 mm×55 mm required about 5.5 hours to complete the coating process with lifting speed of 2 μm/s. By using the emulsion concentration of 20 mg/mL, homogeneous polymer nanosphere arrays with average particle size of 101 nm, 122 nm and 157 nm were successfully fabricated on the solar cell substrate. However, the polymer nanospheres with average size of 97 nm were unable to form a homogeneous array due to the strong electrical repulsion induced by the excessive amount of surfactant. The nanosphere array with average size of 122 nm and 156 nm were believed to have monolayer thickness while the array with average size of 101 nm was observed having partial double layer. The high thermal stability of the polymer nanospheres, which is the T_g at around 110-115°C and the main T_d at 395°C, has provided the advantage for the nanospheres coated on the solar cell. Therefore, the nanosphere arrays are able to withstand long-term sunlight exposure without deforming. Furthermore, the gold or silver nanoparticles with sizes ranged from 3-7 nm were successfully incorporated into the polymer nanospheres during emulsion polymerization process as verified by the TEM and EDX analysis. The light harvesting performance of solar cells coated with the nanospheres with and without embedment of the metallic nanoparticles will be discussed in Chapter 6.

CHAPTER 6

ELECRICAL AND OPTICAL STUDIES ON SOLAR CELL COATED WITH P(MMA-*CO*-AA) POLYMER NANOSPHERES WITH AND WITHOUT ENCAPSULATION OF METALLIC NANOPARTICLES

6.1 Electrical Studies on Solar Cell Coated with P(MMA-*co*-AA) Polymer Nanospheres with and without Encapsulation of Metallic Nanoparticles

In this section, the electrical properties, such as the omnidirectional light harvesting and the current-voltage characteristics of the solar cells coated with the polymer nanospheres with and without the encapsulation of the metallic nanoparticles, will be studied. The electrical power produced by the solar cells under the illumination of the AM 1.5 solar simulator will be discussed. The omnidirectional light harvesting performance of the solar cells will be evaluated under the condition of fluorescent light. Furthermore, the current density-voltage curve of the solar cells will be used to evaluate the photoelectric conversion performance of the solar cells under the AM 1.5 solar spectrum.

6.1.1 Electrical Studies on Solar Cell Coated with P(MMA-*co*-AA) Polymer Nanospheres without Embedment of Metallic Nanoparticles

The polymer nanospheres were coated onto the surface of the *a*-Si photovoltaic cells by using dip-coating technique. The schematic diagram of the nanosphere layers deposited on the surface of the photovoltaic cells is shown in Figure 6.1. In this study, the nanospheres with particle sizes ranging from 97 nm to 156 nm (i.e. 97 nm, 101 nm, 122 nm and 156 nm) were deposited onto the amorphous

silicon solar cells to investigate such range of size in enhancing the performance of the solar cells. In fact, various particle sizes range from 0 to 50 nm and 150 nm to 1 μm have been studied (Akimov, et al., 2010; Chang, et al., 2009; Lin, et al., 2014; Wang and Leu, 2015; Yang, et al., 2015).

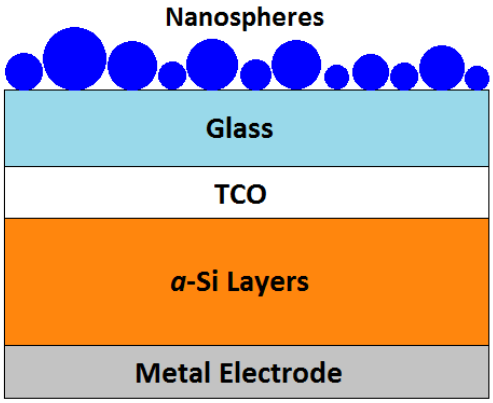

Figure 6.1: A schematic diagram of the P(MMA-*co*-AA) polymer nanospheres deposited on the photovoltaic cell. The nanospheres are represented by the blue circles

Figure 6.2 shows the electrical power produced by the photovoltaic cells deposited with the nanospheres of 97 nm, 101 nm, 122 nm and 156 nm as contrasted with the reference device. The figure shows that the photovoltaic cells coated with the nanospheres of 101 nm average particle size giving the maximum electrical power output as compared to the photovoltaic cells coated with the nanospheres of other sizes. The electrical power produced by the photovoltaic cell coated with the nanospheres with an average size of 101 nm indicates that at least 1.7 times of increment (i.e. from 2.0 mW to 3.5 mW) could be attained relatively to the uncoated sample.

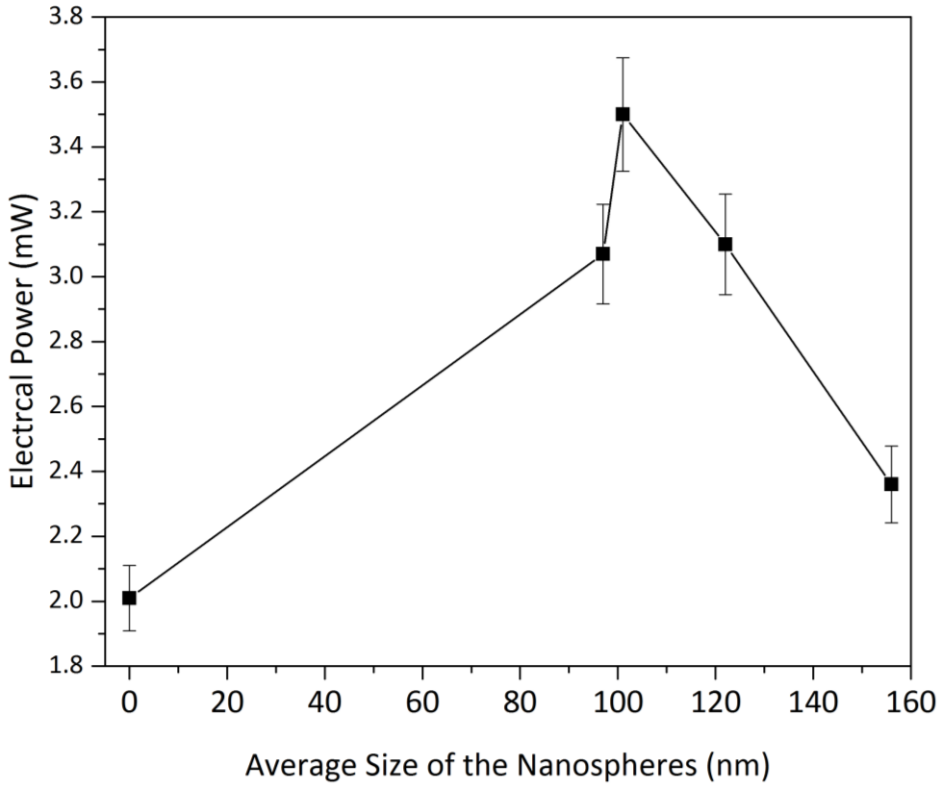

Figure 6.2: The electrical power produced by the photovoltaic cells under the illumination of an AM 1.5 solar simulator as a function of the average size of the polymer nanospheres

The increase of the electrical power could be due to the scattering effects induced by the nanospheres which include Mie scattering and Rayleigh scattering. This may reduce the surface reflection and hence improve the light harvesting efficiency of the solar cells. The Mie scattering takes place as the nanospheres with diameters relatively to the wavelength of the incident light, while the nanospheres with sizes less than one-tenth of the wavelength will undergo Rayleigh scattering (Lin et al., 2014). The experimental results in Figure 6.2 show that the solar cells coated with the nanospheres with the average size of 101 nm have the highest electrical power output. In this case, the Rayleigh scattering serves as the main mechanism for the light absorption of the solar cells deposited with the nanospheres. The increase of the electrical power

output could be attributed to the generation of high free carrier generation resulting from the Rayleigh scattering (Lee, et al., 2017). The nanospheres scatter the incident light and thus improving the light harvesting efficiency of the solar cells. As illustrated under Section 5.3, the nanostructures which comprised of the polymer nanospheres with an average particle size of 101 nm shows the closed pack and disordered arrangement in the FESEM image of Figure 5.9(c). The closed pack arrangement of the nanostructures could result in the multiple scattering of the incoming light, leading to the high power conversion efficiency. (Lin et al., 2014) In addition, the closed pack nanostructures can also work as an intermediate refractive index preventing the sudden change of the refractive index when light travels from the air to the amorphous silicon layer. In fact, it was found that the P(MMA-*co*-AA) polymer the refractive index of 1.494 at 25°C while that of the soda lime glass is 1.524 (Dandekar, 1998). Therefore, the nanosphere coating can reduce the Fresnel reflection resulted from abrupt transition of the refractive indexes from air to glass. As a result, it facilitates the transport of light across the interface to the photoactive layer of the solar cell.

Besides, the non-ordered structure owing to the disordered packing of the self-assembled nanospheres could be a factor in the improvement of light harvesting efficiency of the solar cell. This disordered structure can act as short-range ordered structure or photonic glass in interacting with the incident light (Kim et al., 2011). The unusual optical phenomena such as strong light localization and angle-independent optical scattering could be resulted from the strong interaction between the incoming light and the nanostructures (Kim et al., 2011).

In comparison, the solar cells coated with the nanospheres of 97 nm average size exhibit lower electric power output than that of 101 nm average size. As demonstrated in Figure 5.9(d), the nanostructure, which consists of the nanospheres with average size of 97 nm, are less homogeneous and closely pack than the nanostructure composed of the nanospheres with an average size of 101 nm. Therefore, the nanospheres with the average size of 101 nm are not able to form a more effective intermediate layer than that of 97 nm average size.

On the other hand, the solar cell with the deposition of bigger nanospheres (i.e. particle size of 122 nm) also showed a relatively high electrical power as contrasted with the uncoated solar cell. However, the electrical power produced by the solar cell is relatively smaller than the solar cell deposited with the nanospheres of 101 nm average size. For nanospheres with larger sizes, the nansopheres experiences less Rayleigh scattering in the light trapping process. Nevertheless, the close-packed and homogeneity features of the nanosphere arrays can work as a middle layer with graded refractive index between the active layer and the air.

The current density-voltage (*J-V*) characteristics of the solar cells were simulated under the illumination of AM 1.5 solar simulator. Figure 6.3 represents the *J-V* curve of the uncoated solar cell and the solar cells employing polymer nanospheres with different diameters. The detail photovoltaic parameters of the solar cells are listed in Table 6.1. The solar cell without coated with nanospheres exhibits a J_{SC} of 7 mA cm^{-2}. After coating with the nanospheres of 101 nm average size, the J_{SC} has been increased from 7 mA cm^{-}

^{2} to 9 mA cm^{-2}, which indicates an enhancement of incident light absorption in the photoactive layer. The enhanced J_{SC} results in the augmentation of photoelectric conversion efficacy from 2% to 3.14%, which corresponds to an improvement factor of 57%. Moreover, the results also show a noticeable improvement in the relative increment in the photoelectric conversion efficiency consistent with other published works (Chang, et al., 2009; Akimov, et al., 2010; Lin, et al., 2014; Wang, Gao and Leu, 2016).

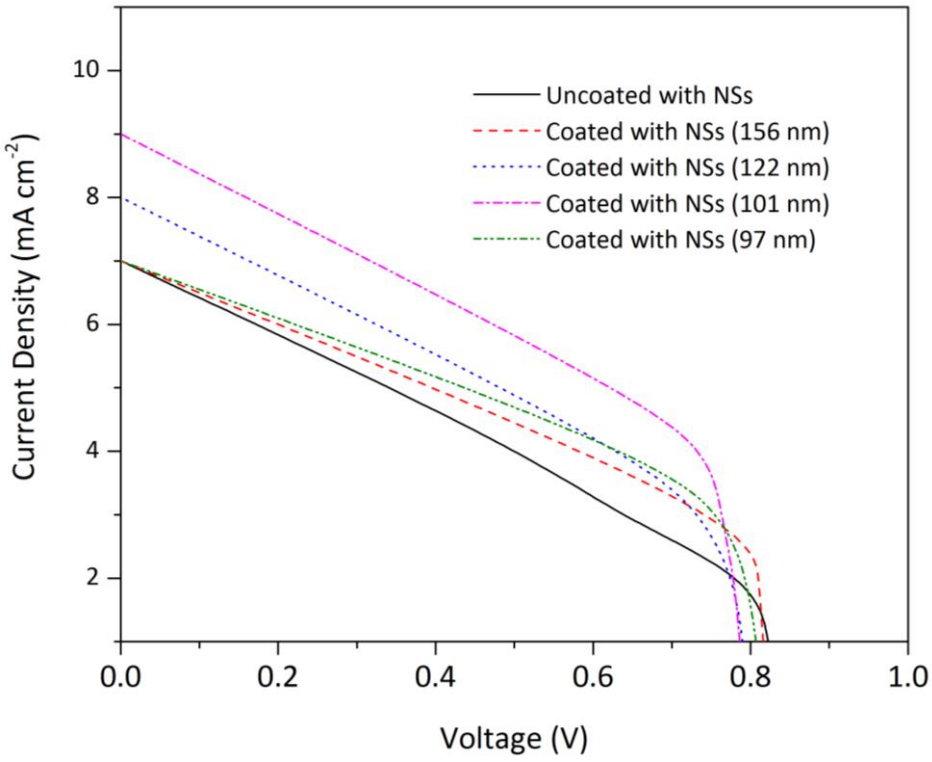

Figure 6.3: Current density versus voltage characteristics of the photovoltaic cells coated with the polymer nanospheres of different particle sizes (i.e. 156 nm, 122 nm, 101 nm and 97 nm) and uncoated photovoltaic cell under the illumination of an AM 1.5 solar simulator

Table 6.1: Photovoltaic parameters of the photovoltaic cells coated with the nanospheres (NSs) of various particle sizes (i.e. 156 nm, 122 nm, 101 nm and 97 nm) measured under AM 1.5 illumination

Device	J_{SC} (mA cm^{-2})	V_{OC} (V)	*FF* (%)	PCE (%)
Uncoated	7	0.82	34	2
Coated with NSs of 156 nm size	7	0.81	41	2.39
Coated with NSs of 122 nm size	8	0.78	41	2.60
Coated with NSs of 101 nm size	9	0.78	44	3.14
Coated with NSs of 97 nm size	7	0.80	47	2.66

In order to determine the omnidirectional light harvesting capability of polymer nanospheres, the exposure angle of solar cell to the light source was altered as stated by the experimental design shown in Section 4.5. The electrical power of the solar cells was measured under the fluorescent illumination. In Figure 6.4, comparable trend was noticed in the electrical power produced by the solar cells with the deposition of nanospheres as compared to Figure 6.2. The solar cell deposited with the nanospheres of 101 nm average size was found to produce the largest electrical power despite the change of exposure angles of the solar cells. Comparable trends can also be perceived for the solar cells at various angles. The omnidirectional light harvesting characteristics of the nanospheres could be attributed to the spherical geometry of the nanospheres that intrinsically accepts light from wide incidence angles (Grandidier, et al., 2011).

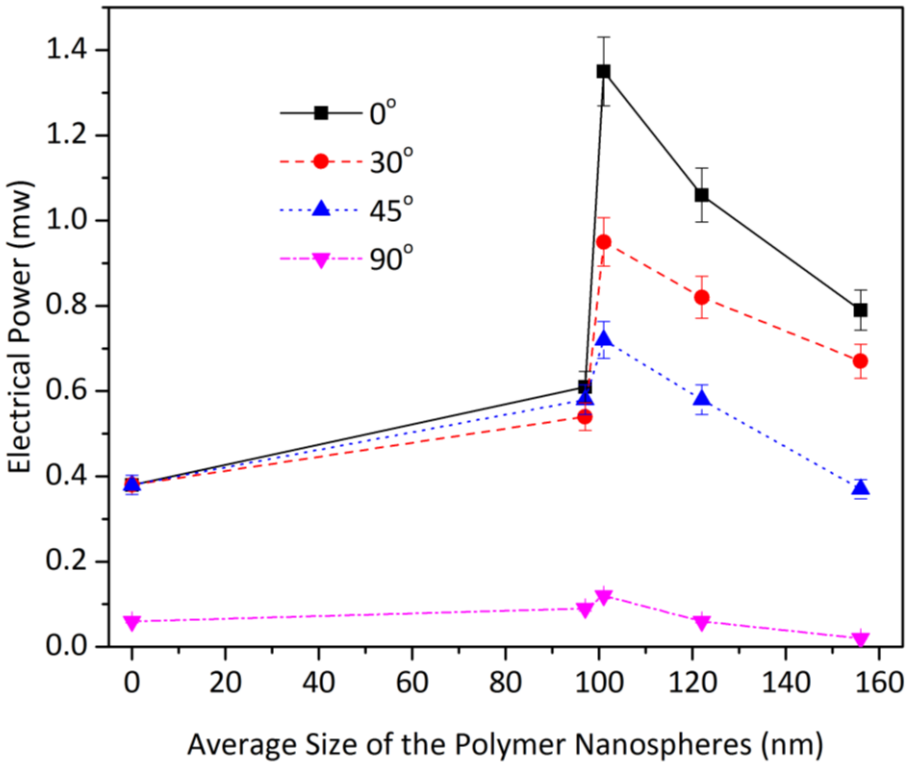

Figure 6.4: The electrical power produced by the photovoltaic cells with different tilted angles of 0°, 30°, 45° and 90° to the fluorescent light source as a function of the average size of the polymer nanospheres

6.1.2 Electrical Studies on Solar Cell Coated with P(MMA-*co*-AA) Polymer Nanospheres Encapsulated with Metallic Nanoparticles

Owing to the plasmonic light trapping of metallic nanoparticles, which give rise to the improvement of light absorption of solar cells, gold nanoparticles (i.e. with particle sizes of 3-5 nm) or silver nanoparticles (i.e. with particle sizes of 3-7 nm) were introduced into the polymer nanospheres. In fact, electromagnetic waves can excite the oscillation of the conduction electrons of the metal nanoparticles. As the frequency of the electromagnetic waves matches the oscillation frequency of the electrons clouds of metallic nanoparticles, localized surface plasmon resonance (LSPR) will be triggered in the metallic nanoparticles. This results in the scattering of the incident light by the metallic nanoparticles into the photoactive layer (Lee et al., 2017). Consequently, this

increases the number of free carriers generated in the active layer. (Mirin and Halas, 2009; Nasser, et al., 2013)

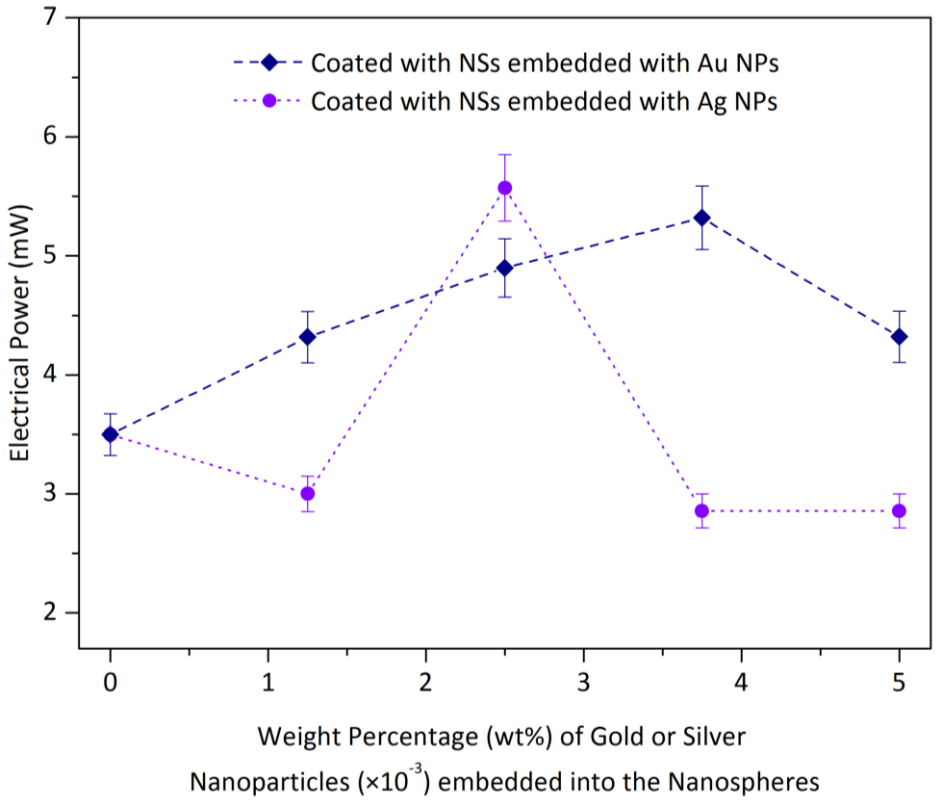

Figure 6.5: The electrical power produced by the photovoltaic cells, which have been coated with the nanospheres (NSs) incorporated with gold nanoparticles (Au NPs) or silver nanoparticles (Ag NPs), under the illumination of an AM 1.5 solar simulator as a function of the weight percentage of the metallic nanoparticles incorporated into the nanospheres

The electrical power generated by the solar cells coated with the nanospheres, which had been embedded with particular amount of gold nanoparticles (i.e. 1.25×10^{-3} to 5×10^{-3} wt%), was measured using the experimental design shown in Section 4.5. In Figure 6.5, the largest value of electrical power of the solar cell was achieved when the nanospheres with an average size of 101 nm was incorporated with 3.75×10^{-3} wt% of gold nanoparticles. The electrical power has increased from 3.5 mW to 5.3 mW compared with the solar cell coated with

the nanospheres without encapsulation of gold nanoparticles, corresponding to an increment of 1.5 times. The experimental results show that the performance of the solar cell can be further improved by incorporating metallic nanoparticles into the nanospheres.

Figure 6.5 also illustrates that the solar cell coated with the nanospheres encapsulated with 2.5×10^{-3} wt% of silver nanoparticles has led to the greatest electrical power output as compared with the rest of the solar cells coated with the nanospheres with different amount of silver nanoparticles. A decrease in the electrical power has been observed when the weight percentage of the silver nanoparticles is higher than 2.5×10^{-3} wt%. The highest increment in the electrical power of about 1.6 times (i.e. from 3.5 mW to 5.6 mW) has been attained compared to the solar cell coated with the polymer nanospheres without embedment. Similar trend was observed from the solar cells coated with the nanospheres which had been incorporated with gold nanoparticles. The results showed that the amount of the metallic nanoparticles encapsulated into the nanospheres is important in obtaining optimum scattering cross-section of the nanoparticles. In comparison, the solar cell coated with polymer nanospheres encapsulated with silver nanoparticles has attained higher electrical power output than that with gold nanoparticles.

Even though both of the metallic nanoparticles exhibit superior light trapping ability, it can give rise to an opposing effect to the performance of solar cell when the amount of the metallic nanoparticles has surpassed the threshold value. The reduction in electrical power could be attributed to the optical loss induced

by the excessive amount of metallic nanoparticles. According to Derkacs et al, a decrease in the enhancement ratio of the transmission of the visible light due to electromagnetic reflection can be perceived as the concentration of gold nanoparticles beyond a particular amount (Derkacs, et al., 2006).

The *J-V* curves of the solar cells coated with the gold nanoparticles and silver nanoparticles measured under AM 1.5 illumination at incident intensity of 100 mA cm^{-2} are demonstrated in Figure 6.6. The photovoltaic parameters of the solar cells calculated based on the *J-V* curves are tabulated in Table 6.2. It can be observed that short circuit current density of the solar cells is improved from 9 mA cm^{-2} to 11 mA cm^{-2} with the embedment of 3.75×10^{-3} wt% gold nanoparticles into the nanospheres, which corresponds to a relatively enhancement of 22% comparing to the solar cell deposited with the blank nanospheres. The increase of the current density is due to the LSPR effect induced by the gold nanoparticles, which enhances the light harvesting ability of the active layer through creating strong near field electromagnetic field and far-field propagating wave (Qiao, et al., 2011). Consequently, this leads to an increase in the efficiency of the solar cells from 3.14% to 5.32%, which corresponds to a relative enhancement of 69% comparing to the solar cell laminated with the nanospheres without encapsulation.

In addition, the solar cell deposited with the nanospheres incorporated with 2.5×10^{-3} wt% silver nanoparticles also exhibits high short circuit current of 12 mA cm^{-2}, resulting in outstanding power conversion efficiency (i.e. 5.57%). This corresponds to a relative increment of 77% in the efficiency if compared to the

solar cell coated with the nanospheres without silver nanoparticles. The high current density and efficiency resulted from silver nanoparticles are contributed by its strong resonance and thus larger scattering cross-section (Nasser, et al., 2013).

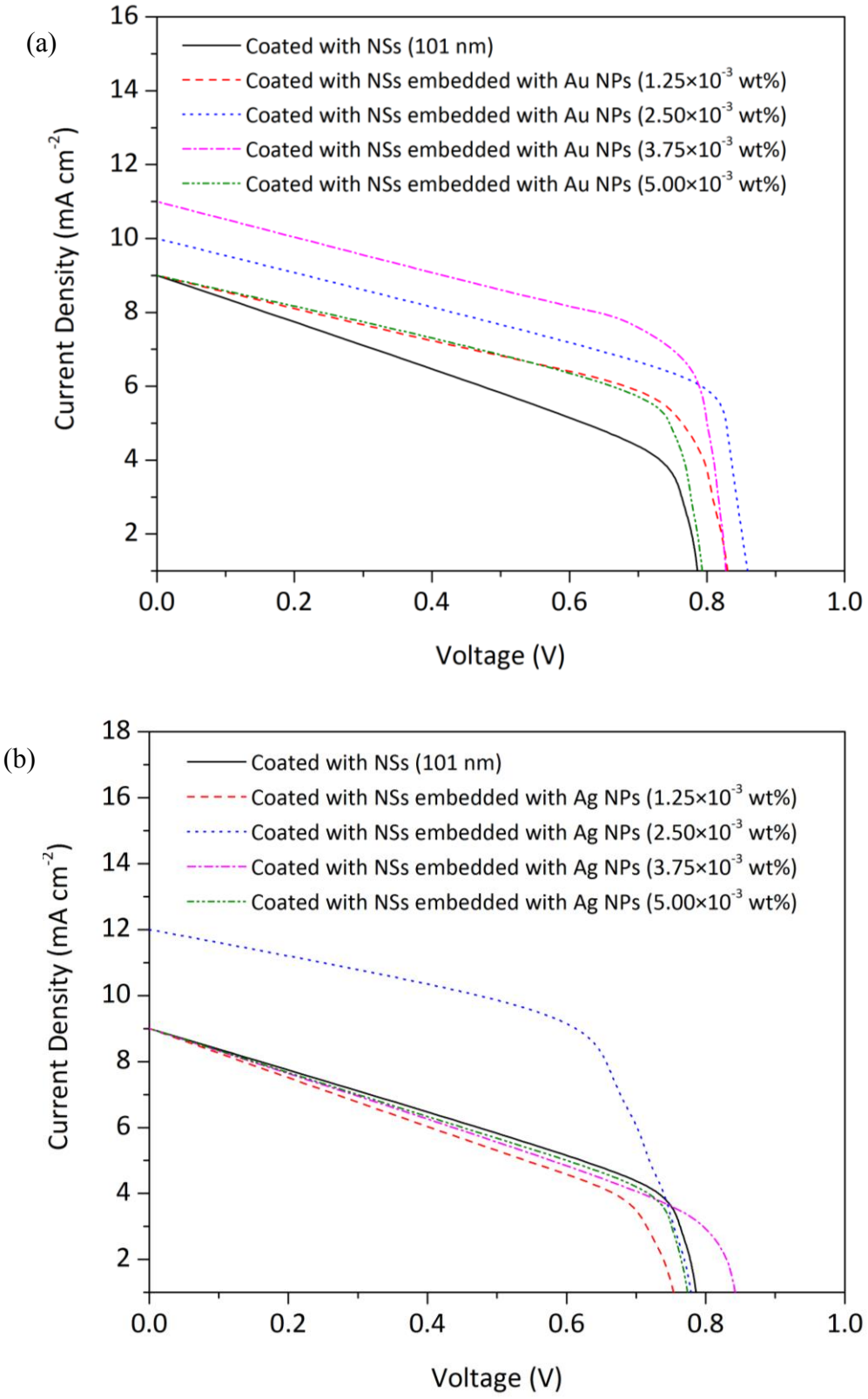

Figure 6.6: Current density versus voltage characteristic of the photovoltaic cells coated with the nanospheres (NSs) embedded with (a) gold nanoparticles (Au NPs) and (b) silver nanoparticles (Ag NPs) of different weight percentages (i.e. 1.25×10^{-3} wt%, 2.5×10^{-3} wt%, 3.75×10^{-3} wt% and 5×10^{-3} wt%) and nanospheres without embedment under the AM 1.5 illumination

Table 6.2: Photovoltaic parameters of the photovoltaic cells coated with the polymer nanospheres (NSs) of 101 nm average size and the nanospheres embedded with metallic nanoparticles which are (a) gold nanoparticles (Au NPs) and (b) silver nanoparticles (Ag NPs) measured under AM 1.5 illumination

Device	J_{SC} (mA cm^{-2})	V_{OC} (V)	*FF* (%)	PCE (%)
Coated with NSs	9	0.78	44	3.14
(a)				
Coated with NSs embedded with Au NPs (1.25×10^{-3} wt%)	9	0.82	57	4.31
Coated with NSs embedded with Au NPs (2.5×10^{-3} wt%)	10	0.85	57	4.91
Coated with NSs embedded with Au NPs (3.75×10^{-3} wt%)	11	0.82	58	5.32
Coated with NSs embedded with Au NPs (5×10^{-3} wt%)	9	0.73	56	4.32
(b)				
Coated with NSs embedded with Ag NPs (1.25×10^{-3} wt%)	9	0.75	40	2.75
Coated with NSs embedded with Ag NPs (2.5×10^{-3} wt%)	12	0.77	59	5.57
Coated with NSs embedded with Ag NPs (3.75×10^{-3} wt%)	9	0.84	38	2.93
Coated with NSs embedded with Ag NPs (5×10^{-3} wt%)	9	0.77	43	3.02

Figure 6.7 illustrates that the nanospheres encapsulated with the metallic nanoparticles exhibit the omnidirectional light harvesting ability. It can be observed that the highest electrical power output has been measured in the solar cells coated with the nanospheres encapsulated with 3.75×10^{-3} wt% of gold nanoparticles and 2.5×10^{-3} wt% of silver nanoparticles, respectively, in spite of the exposure angles of the solar cell.

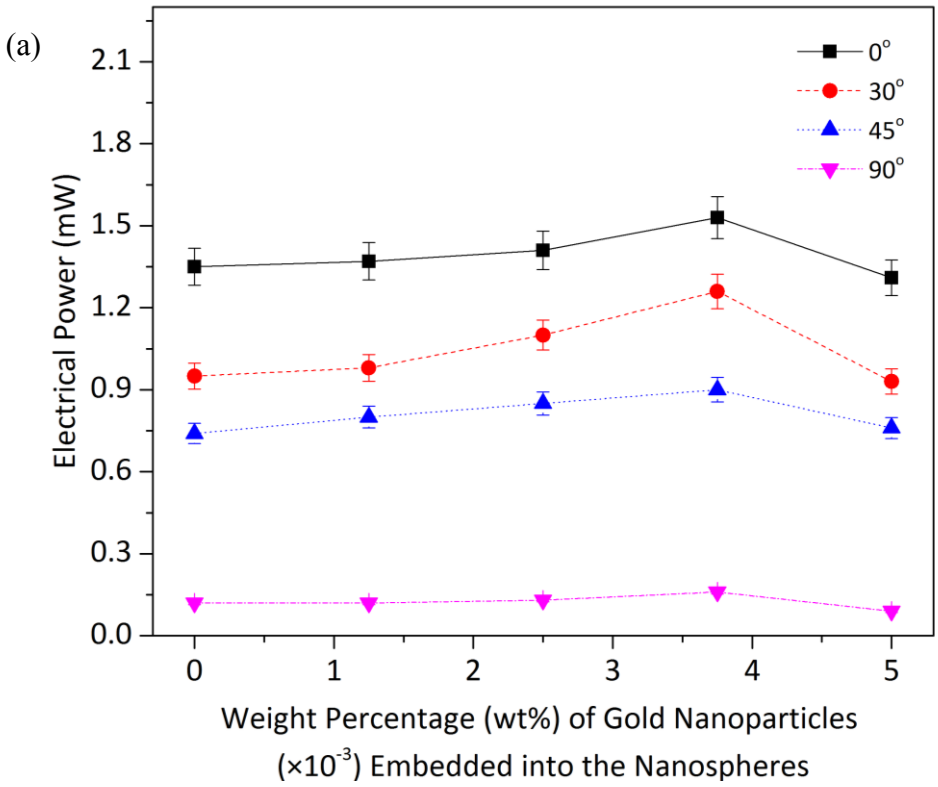

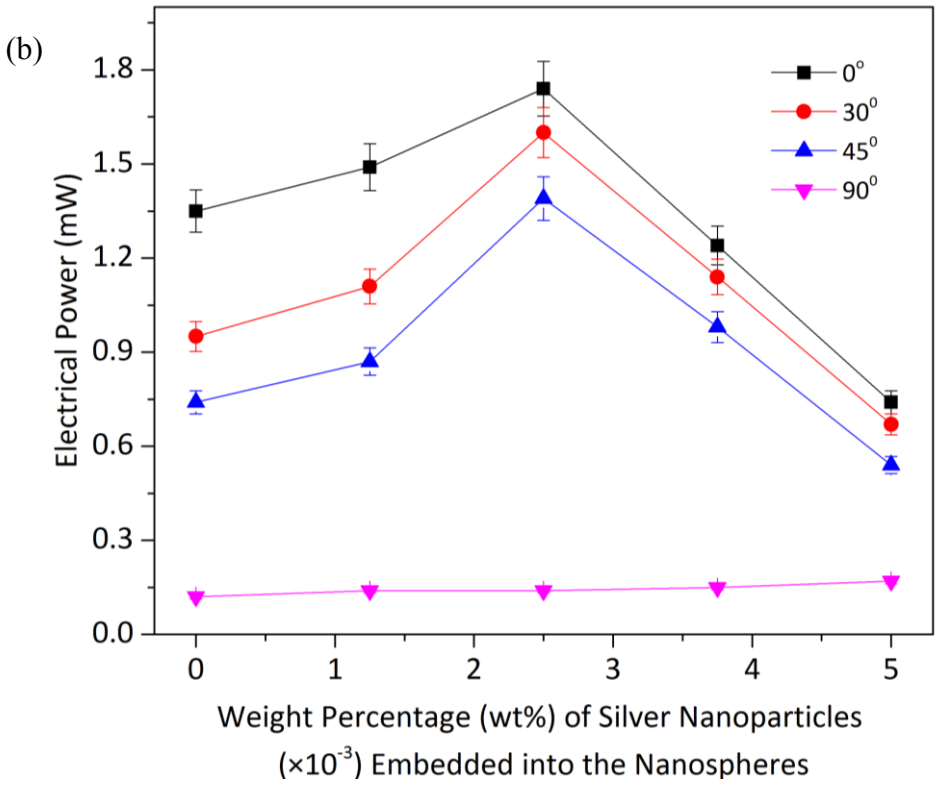

Figure 6.7: The electrical power produced by the photovoltaic cells, which were coated with the nanospheres encapsulated with (a) gold nanoparticles and (b) silver nanoparticles, with different tilted angles of 0°, 30°, 45° and 90° to the fluorescent light source as a function of the weight percentage of gold nanosparticles incorporated into the nanospheres

6.2 Optical Studies on P(MMA-*co*-AA) Polymer Nanospheres with and without Encapsulation of Metallic Nanoparticles

Owing to the improved performance in the solar cells coated with the polymer nanospheres (i.e. 101 nm average size) with and without the incorporation of metallic nanoparticles (i.e. 3.75×10^{-3} wt% gold nanoparticles or 2.5×10^{-3} wt% silver nanoprticles), the optical properties of the nanospheres with and without the embedment of gold or silver nanoparticles were studied and explored further. The ultraviolet-visible (UV-Vis) absorption spectra of the metallic nanoparticles and the blank polymer are shown in Figure 6.8. The UV-Vis spectra show the gold and silver nanoparticles having a plasmon resonance peak at 525 nm and 425 nm. In fact, Qiao et al. and Yoon et al. have reported that the gold nanoprticles and silver nanoparticles with similar sizes exhibit the plasmon resonance peaks at 506 nm at 412 nm respectively (Yoon, et al., 2010; Qiao, et al., 2011). It can be known that the LPSR effect of the metallic nanoparticles will be initiated by the electromagnetic radiation at respective wavelength. The resulted LPSR effect can generate strong near-field electromagnetic wave, which will give rise to the improvement of light absorption of the solar cells. Besides that, the intensity of plasmon resonance peak of silver nanoparticles has been observed to be higher than that of gold nanoparticles, resulting in stronger LPSR effect of the silver nanoparticles as compared to the gold nanoparticles.

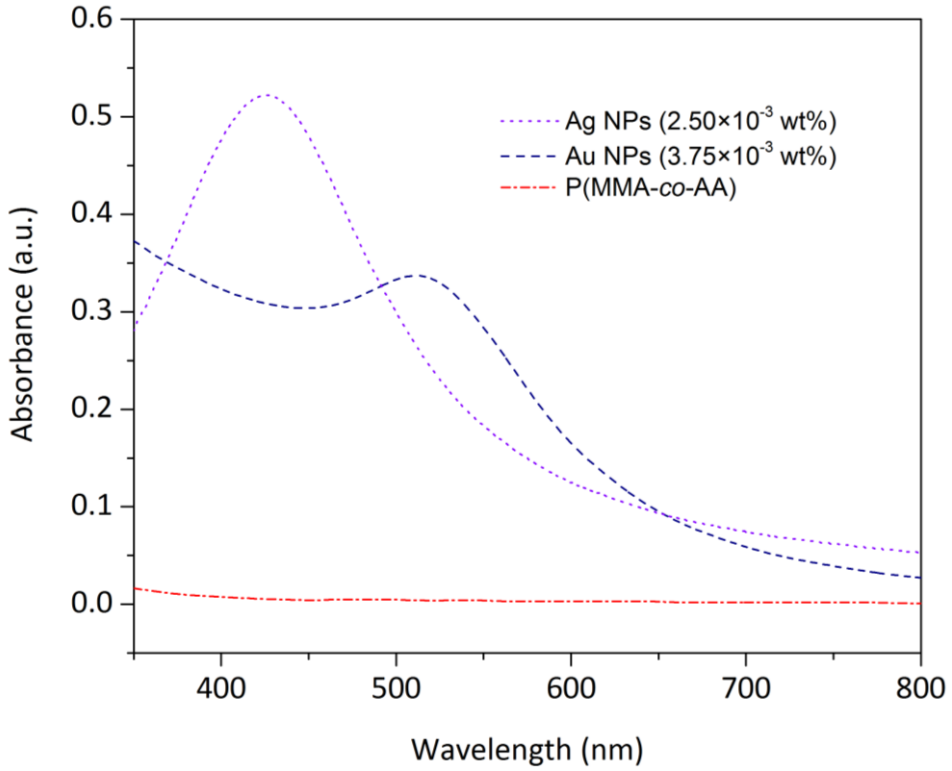

Figure 6.8: Ultraviolet-visible absorption spectra of silver nanosparticles (i.e. 2.5×10^{-3} wt%; Ag NPs), gold nanoparticles (i.e. 3.75×10^{-3} wt%; Au NPs) and the polymer without embedment

In the meantime, Figure 6.9 demonstrated the UV-Vis transmission spectra of the glass substrate coated with the nanospheres without embedment and the nanospheres embedded with metallic nanoparticle (i.e. gold nanoparticles and silver nanoparticles). It is clear from the figure that the nanospheres with the incorporation of silver nanoparticles has attained highest transmittance above 90%, while the transmittance of the nanopsheres with the embedment of gold nanoparticles is almost 90%.

In contrast, the substrate deposited with the nanospheres without metallic nanoparticles exhibits the lower transmittance of about 85%. Instead, the uncoated substrate appears to have the lowest transmittance of abut 80%. The sample with the incorporation of silver nanoparticles exhibits higher

transmittance than that of gold nanoparticles. This could be due to the stronger LSPR effect induced by the silver nanoparticles and hence higher light trapping efficiency.

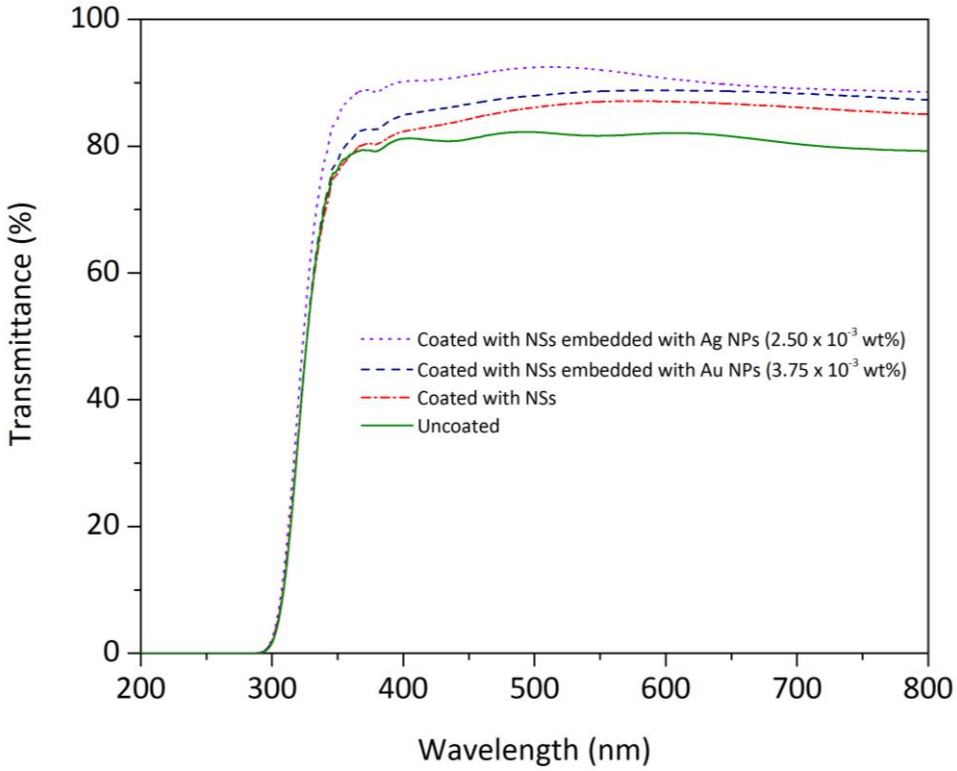

Figure 6.9: Ultraviolet-visible transmission spectra of the polymer nanospheres (NSs) encapsulated with silver nanosparticles (i.e. 2.5×10^{-3} wt%) and gold nanoparticles (i.e. 3.75×10^{-3} wt%), the polymer nanospheres without embedment and uncoated soda lime glass

6.3 Relative Enhancement in Power Conversion Efficiency of Solar Cell Coated with Polymer Nanospheres with and without Incorporation of Metallic Nanoparticles

The *J-V* curves of the solar cells coated with the polymer nanospheres without embedment and the nanospheres with the embedment of silver or gold nanoparticles are plot in Figure 6.10. The detailed photovoltaic parameters are summarized in Table 6.3. The figure illustrates that solar cell coated with the nanospheres encapsulated with silver nanoparticles has the highest short circuit

current density of 12 mA cm^{-2}, while the solar cell coated with the nanospheres embedded with gold nanoparticles shows the second short circuit current density of 11 mA cm^{-2}. The higher current density could be due to the stronger LSPR effect contributed by the silver nanoparticles. As more light are transferred to the absorbing layer, this increases the probability of exciton generation and dissociation and thus larger current density (Qiao, et al., 2011). In addition, the power conversion efficiency of the uncoated solar cell is only 2%. A relative improvement of 57% has been attained as the solar cell were coated with the polymer nanospheres. The solar cells can achieve a noticeable improvement with the relative enhancement of 166% and 179% as the nanosphere embedded with gold and silver nanoparticles, respectively.

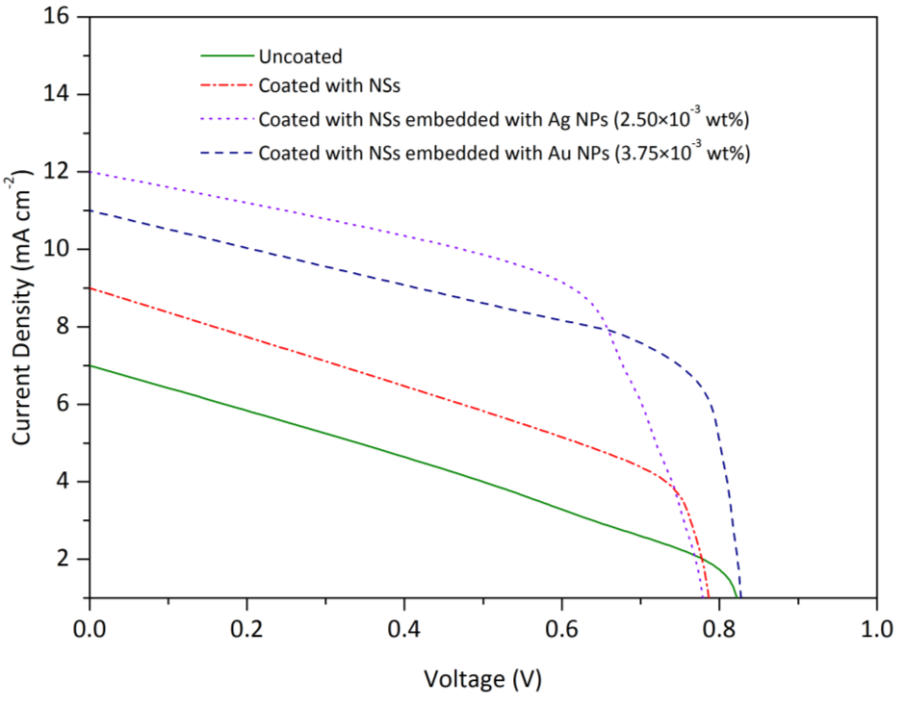

Figure 6.10: Current density against voltage characteristic of the photovoltaic cells coated with the polymer nanospheres incorporated with silver nanoparticles (i.e. 2.5×10^{-3} wt%), gold nanoparticles (i.e. 3.75×10^{-3} wt%), nanospheres without embedment and uncoated photovoltaic cell under the illumination of an AM 1.5 solar simulator

Table 6.3: Photovoltaic parameters of the uncoated and coted photovoltaic cells embedded with gold nanoparticles (Au NPs) or silver nanoparticles (Ag NPs) under the illumination of an AM 1.5 solar simulator

Device	J_{SC} (mA cm^{-2})	V_{OC} (V)	FF (%)	PCE (%)	Relative Enhancement (%)
Uncoated	7	0.82	34	2	-
Coatedwith nanospheres	9	0.78	44	3.14	57
Coated with nanosphees embedded with Au NPs (3.75×10^{-3} wt%)	11	0.82	58	5.32	166
Coated with nanospheres embedded with Ag NPs (2.5×10^{-3} wt%)	12	0.77	59	5.57	179

6.4 Summary

In summary, current density-voltage measurement was carried out in order to study the solar cells deposited with the polymer nanospheres with average size ranged from 97 nm to 156 nm. The polymer nanospheres include the nanospheres with and without encapsulation of gold or silver nanoparticles. The solar cell coated polymer nanospheres with 101 nm average size has shown the most outstanding light harvesting characteristics. The power conversion efficiency measured from the solar cell coated with such nanospheres (i.e. 3.14%) indicates that there is a relative enhancement of 57% compared to the uncoated solar cell with the efficiency of 2%. With the incorporation of 3.75×10^{-3} wt% of gold nanoparticles and 2.5×10^{-3} wt% of silver nanoparticles into the nanopaheres, the power conversion efficiency of solar cells have achieved 5.32% and 5.57% respectively. These correspond to a further enhancement of 166% and 179% in the efficiency of the solar cell compared to the reference solar cell.

CHAPTER 7

CONCLUSIONS AND FUTURE RESEARCH

The conclusions will be divided into three main sections which includes the preparation of the polymer nanospheres with and without embedment, the fabrication of self-assembled nanospheres on solar cell substrate and the improvement of the performance of treated solar cells. Furthermore, recommendations for the current work and suggestions for the future studies will be provided in order to improve the quality of the current work.

7.1 Conclusions

7.1.1 P(MMA-*co*-AA) Polymer Nanospheres and Nanospheres Encapsulated with Metallic Nanoparticles Coated on Solar Cell

Poly(methyl methacrylate-*co*-acrylic acid) polymer dispersions with high solid content (i.e. 18-19%) were prepared through the emulsion polymerization technique. The polymer exhibits viscosity-average molecular weight of 811430 g/mol and refractive index of 1.494. The Fourier transform infrared spectra have shown that the polymer chains consist of methyl methacrylate and acrylic acid segments. The particle sizes of the nanospheres could be controlled by adjusting the surfactant concentration used in the polymerization process. The nanospheres with mean particle size of 156, 122, 101 and 97 nm were obtained with the surfactant concentration of 5.3, 10.5, 15.8 and 21 mM used in the polymerization process, respectively.

The polymer with good thermal stability was synthesized using the emulsion polymerization technique. The polymer exhibits high glass transition temperature (i.e. around 110-115°C) as well as decomposition temperature (i.e. the first decomposition stage of decomposition happens at 150°C with subsequent major decomposition of the polymer chains at 395°C). In addition, the amount of surfactant not only controlled the particle sizes of the nanospheres but also affected their glass transition temperature. The glass transition temperature of the polymer was decreased from 115°C to 110°C as the concentration of surfacing was increased from 5.3 mM to 21 mM. The X-ray diffraction results have also indicated that the P(MMA-*co*-AA) polymer exhibits amorphous structural order. The transmission electron microscope images and energy dispersive X-ray spectra have shown that the metallic nanoparticles (i.e. gold nanoparticles or silver nanoparticles) were successfully incorporated into the polymer nanospheres through the emulsion polymerization technique.

The polymer nanosphere arrays were developed on the solar cell substrate using dip coating technique. The results have indicated that the concentration of polymer dispersion could greatly influence the self-assembly of the polymer nanospheres. The substrate with homogeneous polymer nanosphere array could be achieved with the emulsion concentration of 20 mg/mL and the lifting speed of 2 μm/s. However, multilayer nanosphere array was observed when increasing the emulsion concentration to 25 mg/mL. The nanostructure composed of the polymer nanospheres with 101 nm average size exhibits a random packing structure. The voids and defects observed in the FESEM and AFM images of

the nanosphere array developed using the polymer nanospheres with average size of 97 nm could be properly resulted from the excessive surfactant in emulsion.

7.1.2 Enhancement in Power Conversion Efficiency of Solar Cell

Among the polymer nanospheres with average of average size of 156 nm, 122 nm, 101 nm and 97 nm, the results have shown that the solar cell deposited with the polymer nanospheres of 101 nm average size achieved the largest optical efficiency of 3.14%. As compared to the reference device with the efficiency of 2%, this gives rise to a relative enhancement of 57%. By incorporating 3.75×10^{-3} wt% of gold nanoparticles and 2.5×10^{-3} wt% of silver nanoparticles into the nanospheres, the solar cell has showed additional increment in PCE from 2% to 5.32% and 5.57%, respectively. These correspond to a relative enhancement 166% for gold nanoparticles and 179% for silver nanoparticles. In addition, omnidirectional characteristic was observed for the solar cell coated with the polymer nanospheres. The gold nanoparticles and silver nanoparticles exhibit the LSPR property within the absorption range of the solar cell at 525 nm and 425 nm, respectively. The ultraviolet-visible transmission spectra have demonstrated that the transmittance of light increased from 80% to 90% with the deposition of polymer nanospheres with average size of 101 nm and the nanospheres embedded with the metallic nanoparticles onto the solar cell.

7.2 Recommendations and Future Research

More studies can be carried out in order to provide comprehensive support to our research outcomes, such as quantum efficiency measurement and specular reflectance spectroscopic studies. The quantum efficiency test is used to obtain the performance of the solar cell for different wavelength of light. This is useful in studying the enhancement of photocurrent caused by the light scattering of the polymer nanospheres and the plasmonic light trapping of the metallic nanoparticles. Moreover, the reflectance spectrum of the solar cell can be used to investigate the omnidirectional antireflection performance of the nanosphere arrays deposited on the solar cell.

In order to improve the durability of the treated solar cell, the adhesion of polymer nanospheres can be improved through chemical curing technique. For example, trimethoxyvinlysilane can be copolymerized with the polymer chains, which acts as a curing agent bonding to the glass surface through thermal treatment. This allows the integrity of the nanostructure coated on solar cell able to withstand varied weather conditions and hence maintaining its light trapping efficiency in a prolong time. The dip coating method utilized in this study was required five hours to complete the fabrication process due to its slow drawing rate. Therefore, a new method can be developed to shorten the fabrication process of the polymer thin film. Spin-coating technique can be used as an alternative method to fabricate the nanostructure onto solar cell due to its high spin speed and hence shorter deposition time.

Beside of gold nanoparticles and silver nanoparticles, copper nanoparticles can also become a candidate used for the light trapping in solar cells. This is because the copper nanoparticles possess LSPR band within the absorption range of the solar cell at 600 nm. Hence, the nanospheres embedded with copper nanoparticles are expected to deliver a comparable augmentation of light absorption in the solar cell with the gold nanoparticles and silver nanoparticles. The reported polymer nanosphere array also has potential to be applied in manufacturing other optoelectronic devices such as light-emitting diodes and optical fiber due to its excellent light manipulation properties.

REFERENCES

Akimov, Y.A., Koh, W.S., Sian, S.Y. and Ren, S., 2010. Nanoparticle-enhanced thin film solar cells: metallic or dielectric nanoparticles?. *Applied Physics Letters*, 96(7), pp. 1-3

American Polymer Standards Corporation, 2018. *Mark-Houwink Parameters for Polymers*. [online] Available at: < http://www.ampolymer.com/Mark-Houwink.html> [Accessed 21 December 2018]

ASTM E1356-91, 1991. *Standard test method for glass transition temperatures by differential scanning calorimetry or differential thermal analysis*. West Conshohocken: ASTM International.

Baek, S.W., Noh, J., Lee, C.H., Kim, B.S., Seo, M.K. and Lee, J.Y., 2013. Plasmonic forward scattering effect in organic solar cells: a powerful optical engineering method. *Scientific Reports*, 3, pp. 1-7.

Caruso, F., 2004. *Colloids and colloidal assemblies: synthesis, modification, organization and utilization of colloid partticles*. Weinheim: Wiley-VCH.

Chang, T.H. Wu, P.H., Chen, S.H. Chan, C.H., Lee, C.C., Chen, C.C. and Su, Y.K., 2009. Efficiency enhancement in GaAs solar cells using self-assembled microspheres. *Optics Express*, 17(8), pp. 6519-6524.

Chao, Y.C., Zhan, F.M. and Li, H.D., 2014. Indium-tin-oxide nanorods for efficient light trapping in polymer solar cells. *RSC Advances*, 4(58), pp. 30881-30886.

Chern, C.S., 2008. *Applications of emulsion polymerization.* New Jersey: Wiley.

Chou, C.H. and Chen, F.C., 2014. Plasmonic nanostructures for light trapping in organic photovoltaic devices. *Nanoscale*, 6(15), pp. 8444-8458.

Cong, H. and Cao, W., 2003. Colloidal crystallization induced by capillary force. *Langmuir*, 19(20), pp. 8177-8181.

Cong, H., Yu, B., Tang, J., Li, Z. and Liu, X., 2013. Current status and future developments in preparation and application of cooloidal crystals. *Chemical Society Reviews*, 42(19), pp. 7774-7800.

Dabirian, A., Byranvand, M.M., Naqavi, A., Kharat, A.N. and Taghavinia, N., 2016. Self-assembled monolayer of wavelength-scale score-shell particle for low-loss plasmonic and broadband light trapping in solar cells. *ACS Applied Materials & Interfaces*, 8(1), pp. 247-255.

Dandekar, D.P., 1998. Index of refraction and mechanical behavior of soda lime glass under shock and release wave propagations. *Journal of Applied Physics*, 84(12), pp. 6614-6622.

Derjaguin, B. and Landau, L., 1941. Theory of the stability of strongly charged lyophobic sols and of the adhesion of strongly charged particles in solution of electrolytes. *Acta Physicochim*. *URSS*, 14, pp. 633-662.

Derkacs, D., Lim, S.H., Matheu, P., Mar, W. and Yu, E.T., 2006. Improved performance of amorphous silicon solar cells via scattering from surface plasmon polaritons in nearby metallic nanoparticles. *Applied Physics Letters*, 89(9), pp. 1-3.

Dimitrov, A.S. and Nagayama, K., 1996. Continuous convective assembling of fine particles into two-dimensional arrays on solid surfaces. *Langmuir*, 13(5), pp. 1303-1311.

El-Zaher, N.A., Melegy, M.S., Guirguis, O.W., 2014. Thermal and structural analyses of PMMA/TiO_2 nanoparticles composites. *Natural Science*, 6(11), pp. 859-870.

Fan, Z. Razavi, H. Do, J., Moriwaki, A., Ergen, O., Chueh, Y.L., Leu, P.W., Ho, J.C., Takahashi, T., Reichertz. L.A., Neale, S., Yu, K., Wu, M., Ager, J.W. and Javey, A., 2009. Three-dimensional nanopillar-array photovoltaics on low-cost flexible substrates. *Nature Materials*, 8(8), pp. 648-653.

Fan, G., Zhu, H., Wang, K., Wei, J., Li, X., Shu, Q., Guo, N. and Wu, D., 2011. Graphene/silicon nanowire Schottky junction for enhanced light harvesting. *ACS Applied Materials & Interfces*, 3(3), pp. 721-725.

Fang, C.Y., Liu, Y.L., Lee, Y.C., Chen, H.L., Wan, D.H. and Yu, C.C., 2013. Nanoparticle stacks with graded refractive indices enhance the omnidirectional light harvesting of solar cells and the light extraction of light-emitting diodes. *Advanced Functional Materials*, 23(11), pp. 1412-1421.

Ferry, V.E., Verschuuren, M.A., Li, H.B.T., Verhagen, E., Walters, R.J., Schropp, R.E.I., Atwater, H.A., Polman, A., 2010. Light trapping in ultrathin plasmonic solar cells. *Optics Express*, (18)S2, pp. A237-A245.

Freymann, G., Kitaev, V., Lotsch, B.V. and Ozin, G.A., 2013. Bottom-up assembly of photonic crystals. *Chemical Society Reviews*, 42(7), pp. 2528-2554.

Galisteo-López, J.F., Ibisate, M., Sapienza, R., Froufe-Pérez, L.S., Blanco, A. and López, C., 2011. Self-assembled photonic structures. *Advanced Materials*, 23(1), pp. 30-69.

García, P.D., Sapienza, R. and López, C., 2010. Photonic glasses: a step beyond white paint. *Advanced Materials*, 22(1), pp. 12-19.

Garnett, E. and Yang, P., 2010. Light trapping in silicon nanowire solar cells. *Nano Letters*, 10(3), pp. 1082-1087.

Gjessing, J., 2011. *Photonic crystals for light trapping in solar cells*. PhD. University of Oslo.

Grandidier, J., Callahan, D.M., Munday, J.N. and Atwater, H.A., 2011. Light absorption enhancement in thin-film solar cells using whispering gallery modes in dielectric nanospheres. *Advanced Materials*, 23(10), pp. 1272-1276.

Grandidier, J., Callahan, D.M., Munday, J.N. and Atwater, H.A., 2012. Gallium arsenide solar cell absorption enhancement using whispering gallery modes of dielectric nanospheres. *IEEE Journal of Photovoltaics*, 2(2), pp. 123-128.

Grandidier, J., Weitekamp, R.A, Deceglie, M., Callahan, D.M., Battaglia, C., Bukowsky, C.R., Balif, C., Grubbs, R.H. and Atwater, H.A., 2013. Solar cell efficiency enhancement via light trapping in printable resonant dielectric nanosphere arrays. *Physica Status Solidi A*, 210 (2), pp. 255-260.

Grassie, N., 1956. Chemistry of high polymer degradation processes. New York: Interscience.

Gu, Z.Z., Fujishima, A. and Sato, O., 2002. Fabrication of high-quality opal films with controllable thickness. *Chemistry of Materials*, 14(2), pp. 760-765.

Haugan, E., 2011. *Colloidal crystals as templates for light harvesting structures in solar cells.* MSc. Norwegian University of Science and Technology.

He, L., Jiang, C., Rusli, Lai, D. and Wang, H., 2011. Highly efficient Si-nanorods/organic hybrid core-sheath heterojunction solar cells. *Applied Physics Letters*, 99(2), pp. 1-3.

Hsiao, Y.S., Charan, S., Wu, F.Y, Chien, F.C., Chu, C.W., Chen, P. and Chen, F.C., 2012. Improving the light trapping efficiency of plasmonic polymer solar cells through photon management. *The Journal of Physical Chemistry C*, 116(39), pp. 20731-20737.

Im, S.H., Kim, M.H. and Park, O.O., 2003. Thickness control of colloidal crystals with a substrate dipped at a tilted angle into a colloidal suspension. *Chemistry of Materials*, 15(9), pp. 1797-1802.

Jiang, P., Bertone, F., Hwang, K.S. and Colvin, V.L., 1999. Single-crystal colloidal multilayers of controlled thickness. *Chemistry of Materials*, 11(8), pp. 2132-2140.

Kanade, P., Yadav, P., Kumar, M. and Tripathi, B, 2015. Plasmon-induced photon management by Ag nanoparticle-coupled graphene thin-film: light trapping for photovoltaics. *Plasmonics*, 10(1), pp. 157-164.

Kelly, K.L., Coronado, E., Zhao, L.L. and Schatz, G.C., 2003. The optical properties of metal nanoparticles: the influence of size, shape, and dielectric environment. *The Journal of Physical Chemistry B*, 107(3), pp. 668-677.

Kim, S.H., Lee, S.Y., Yang, S.M. and Yi, G.R., 2011. Self-assembled colloidal structures for photonics. NPG Asia Materials, 3(1), pp. 25-33.

Kim, S.S., Na, S.K., Jo, J., Kim, D.Y. and Nah, Y.C., 2008. Plasmon enhanced performance of organic solar cells using electrodeposited Ag nanoparticles. *Applied Physics Letters*, 93(7), pp. 073307.

Kirkeminde, A., Retsch, M., Wang, Q., Xu, G., Hui, R., Wu, J. and Ren, S., 2012. Surface-passivated plasmonic nano-pyramids for bulk heterojunction solar cell photocurrent enhancement. *Nanoscale*, 4(15), pp. 4421-4425.

Kobayashi, S. and Müllen, K., 2015. Encyclopedia of polymeric nanomaterials. Berlin: Springer-Verlag.

Kuai, S.L., Hu, X.F., Haché, A. and Truong, V.V., 2004. High-quality colloidal photonic crystals obtained by optimizing growth parameters in a vertical deposition technique. *Journal of Crystal Growth*, 267(1-2), pp. 317-324.

Lee, C.L., Goh, W.S., Chee, S.Y. and Yik, L.K., 2018. Augmentation of power conversion efficiency of amorphous silicon solar cell employing poly(methyl methacrylate-*co*-acrylic acid) nanospheres encapsulated with gold nanoparticles. *Journal of Materials Science*, 53(7), pp. 5183-5193.

Lee, C.L., Goh, W.S., Chee, S.Y. and Yik, L.K, 2017. Enhancement of light harvesting efficiency of silicon solar cell utilizing arrays of poly(methyl methacrylate-*co*-acrylic acid) nano-spheres and nano-spheres with embedded silver nano-particles. *Photonics and Nanostructures – Fundamentals and Applications*, 23, pp. 36-44.

Lee, Y.J., Ruby, D.S., Peters, D.W., McKenzie, B.B. and Hsu, J.W.P., 2008. ZnO nanostructures as efficient antireflection layers in solar cells. *Nano Letters*, 8(5), pp. 1501-1505.

Li, H.L. and Marlow, F., 2006. Solvent effects in colloidal crystal deposition. *Chemistry of Materials*, 18(7), pp. 1803-1810.

Lin, G.J., Wang, H.P., Lien, D.H., Fu, P.H., Chang, H.C. Ho, C.H., Lin, C.A., Lai, K.Y. and He, J.H., 2014. A broadband and omnidirectional light-harvesting scheme employing nanospheres on Si solar cells. *Nano Energy*, 6, pp. 36-43.

Liu, Z., Ya, J., Xin, Y., Ma, J. and Zhou, C., 2006. Assembly of polystyrene colloidal crystal templates by a dip-drawing method. *Journal of Crystal Growth*, 2917(1), pp. 223-227.

Marco, L.D., Manca, M., Giannuzzi, R., Malara, F., Melcarne, G., Ciccarella, G., Zama, I., Cingolani, R. and Gigli, G., 2010. Novel preparation method of TiO_2-nanorod-based photoelectrodes for dye-sensitized solar cells with improved light-harvesting efficiency. *The Journal of Physical Chemistry C*, 114(9), pp. 4228-4236.

McNeill, I.C. and Sadeghi, S.M.T., 1990. Thermal stability and degradation mechanisms of poly(acrylic acid) and its salts: part 1-poly(acrylic acid). *Polymer Degradation and Stability*, 29(2), pp. 233-246.
Mirin, N.A., Halas, N.J., 2009. Light-bending nanoparticles. *Nano Letters*, 9(3), pp. 1255-1259.

Mohy, E.M.S., Elaassar, M.R., Elzatahry, A.A. and Al-Sabah, M.M.B., 2017. Poly(acrylonitrile-co-methyl methacrylate) nanoparticles: I. Preparation and characterization. *Arabian Journal of Chemistry*, 10(8), pp. 1153-1166.

Nasser, H., Saleh, Z.M., Özkol, E., Günoven, M., Bek, A., Turan, R., 2013. Fabrication of Ag nanoparticles embedded in Al:ZnO as potential light-trapping plasmonic interface for thin film solar cells. *Plasmonics*, 8(3), pp. 1485-1492.

Nelson, J., 2005. *The physics of solar cells*. London: Imperial College Press.

Odian, G., 2004. *Principles of polymerization*. 4th ed. New York: Wiley Interscience.

Pillai, S., Catchpole, K.R., Trupke, T. and Green, M.A., 2007. Surface plasmon enhanced silicon solar cells. *Journal of Applied Physics*, 101(9), pp. 1-8.

Porter, C.E. and Blum, F.D., 2000. Thermal characterization of PMMA thin films using modulated differential scanning calorimetry. *Macromolecules*, 33(19), pp. 7016-7020.

Pu, X., Liu, J., Liang, J., Xia, Y., Feng, W., Wang Y. and Yu, X., 2014. Effective CdS/ZnO nanorod arrays as antireflection coatings for light trapping in c-Si solar cells. *RSC Advances*, 4(44), pp. 23149-23154.

Qi, M., Lidorikis, E., Rakich, P.T., Johnson, S.G., Joannopoulos, J.D. Ippen, E.P. and Smith, H.I., 2004. A three-dimensional optical photonic crystal with designed point defects. *Nature*, 429, pp. 538-542.

Qiao, L., Wang, D., Zuo, L., Ye, Y., Qian, J., Chen, H. and He, S., 2011. Localised surface plasmon resonance enhanced organic solar cell with gold nanospheres. *Applied Energy*, 88(3), pp. 848-852.

Rowe, E.L., 1965. Effect of emulsifier concentration and type on the particle size distribution of emulsions. *Journal of Pharmaceutical Sciences*, 54(2), pp. 260-264.

Schlüter, D.A., Hawker, C.J. and Sakamoto, J., 2012. *Synthesis of polymers: new structures and methods*. Weinheim: Wiley-VCH.

Shanti, R., Bella, F., Salim, Y.S., Chee, S.Y., Ramesh, S. and Ramesh, K., 2016. Poly(methyl methacrylate-*co*-butyl acrylate-*co*-acrylic acid): physico-chemical characterization and targeted dye sensitized solar cell application. *Materials & Design*, 108, pp. 560-569.

Solanki, C.S., 2015. *Solar photovoltaics: fundamentals, technologies and applications*. 3rd ed. Delhi: PHI Learning.

Tang, Z., Tress, W. and Inganäs, O., 2014. Light trapping in thin film organic solar cells. *Materials Today*, 17(8), pp. 390-396.

Tao, A.R., Huang, J. and Yang, P., 2008. Langmuir-Blodgettry of nanocrystals and nanowires. *Accounts of Chemical Research*, 41(12), pp. 1662-1673.

Temple, T.L., Mahanama, G.D.K., Reehal, H.S. and Bagnall, D.M., 2009. Influence of localized surface plasmon excitation in silver nanoparticles on the performance of silicon solar cells. *Solar Energy Materials & Solar Cells*, 93(11), pp. 1978-1985.

Tétreault, N. and Grätzel, M., 2012. Novel nanostructures for next generation dye-sensitized solar cells. *Eenergy & Environmental Science*, 5(9), pp. 8506-8516.

Todica, M., Stefan, T., Simon, S., Balasz, I. and Daraban, L., 2014. UV-Vis and XRD investigation of graphite-doped poly(acrylic) acid membranes. *Turkish Journal of Physics*, 38, pp. 261-267.

Tsai, M.A., Tseng, P.C., Chen, H.C., Kuo, H.C. and Yu, P., 2011. Enhanced conversion efficiency of a crystalline silicon solar cell with frustum nanorod arrays. pp. 389-396.

Verwey, E.W. and Overbeek, J.T.G., 1948. *Theory of the stability of lyophobic colloids*. Amsterdam: Elsevier.

Vogel, N., Weiss, C.K. and Landfester, K., 2012. From soft to hard: the generation of functional and complex colloidal monolayers for nanolithography. *Soft Matter*, 8(15), pp. 4044-4061.

Wang, B., Gao, T. and Leu, P.W., 2016. Broadband light absorption enhancement in ultrathin film crystalline silicon solar cells with high index of refraction nanosphere arrays. *Nano Energy*, 19, pp. 471-475.

Wang, B. and Leu, P.W., 2015. High index of refraction nanosphere coatings for light trapping in crystalline silicon thin film solar cells. *Nano Energy*, 13, pp. 226-232.

Wang, K.X., Yu, Z., Liu, V., Raman, A., Cui, Y. and Fan, S., 2014. Light trapping in photonic crystals. *Energy & Environmental Science*, 7(8), pp. 2725-2738.

Xia, Y., Gates, B., Yin, Y. and Lu, Y., 2000. Monodispersed colloidal spheres: old materials with new aplications. *Advanced Materials*, 12(10), pp. 693-713.

Yang, X., Zhou, S., Wang, D., He, J., Zhou, J., Li, X., Gao, P. and Ye, J., 2015. Light trapping enhancement in a thin film with 2D conformal periodic hexagonal arrays. *Nanoscale Research Letters*, 10, pp. 1-9.

Yoldi, M., Arcos, C., Paulke, B., Sirera, R., González-Viñas, W and Görnitz, E., 2008. On the parameters influencing the deposition of polystyrene colloidal crystals. *Materials Science and Egnineering C*, 28(7), pp. 1038-1043.

Yoon, W.J., Jung, K.Y., Liu, J., Duraisamy, T., Revur, R., Teixeira, F.L., Sengupta, S. and Berger, P.R., 2010. Plasmon-enhanced optical absorption and photocurrent in organic bulk heterojunction photovoltaic devices using self-assembled layer of silver nanoparticles. *Solar Energy Materials and Solar Cells*, 94(2), pp. 128-132.

Zhu, J., Hsu, C.M., Yu, Z., Fan, S. and Cui, Y., 2010. Nanodome solar cells with efficient light management and self-cleaning. *Nano Letters*, 10(6), pp. 1979-1984.

Zarick, H.F., Erwin, W.R., Boulesba, A., Hurd, O.K., Webb, J.A., Puretzky, A.A., Geohegan, D.B., Bardhan, R., 2016. Improving light harvesting in dye-sensitized solar cells using hybrid bimetallic nanostructures. *ACS Photonics*, 3(3), pp. 385-394

Zhang, Q., Myers, D., Lan, J., Jenekhe, S.A. and Cao, G., 2012. Applications of light scattering in dye-sensitized solar cells. *Physical Chemistry Chemical Physics*, 14(43), pp. 14982-14998.

APPENDIX A

Table 1: Flow time measurement of poly(methyl methacrylate-*co*-acrylic acid) polymer in tetrahydrofuran at 25°C

Concentration (g/dL)	Flow time (s)			Average time (s)
	1	2	3	
0	148.0	149.1	149.2	148.0
0.529	225.8	225.7	225.3	225.6
0.559	228.0	227.9	227.7	227.8
0.592	231.8	230.2	230.2	230.7
0.629	233.0	232.9	232.8	232.9
0.671	236.3	236.3	236.1	236.2

Table 2: Relative, specific and reduced viscosities for poly(methyl methacrylate-*co*-acrylic acid) polymer in tetrahydrofuran at 25°C.

Concentration (g/dL)	η_{rel}	η_{sp}	η_{red} (dL/g)
0.529	1.5165	0.5165	0.9749
0.559	1.5317	0.5317	0.9507
0.592	1.5510	0.5510	0.9304
0.629	1.5654	0.5654	0.8985
0.671	1.5878	0.5878	0.8759

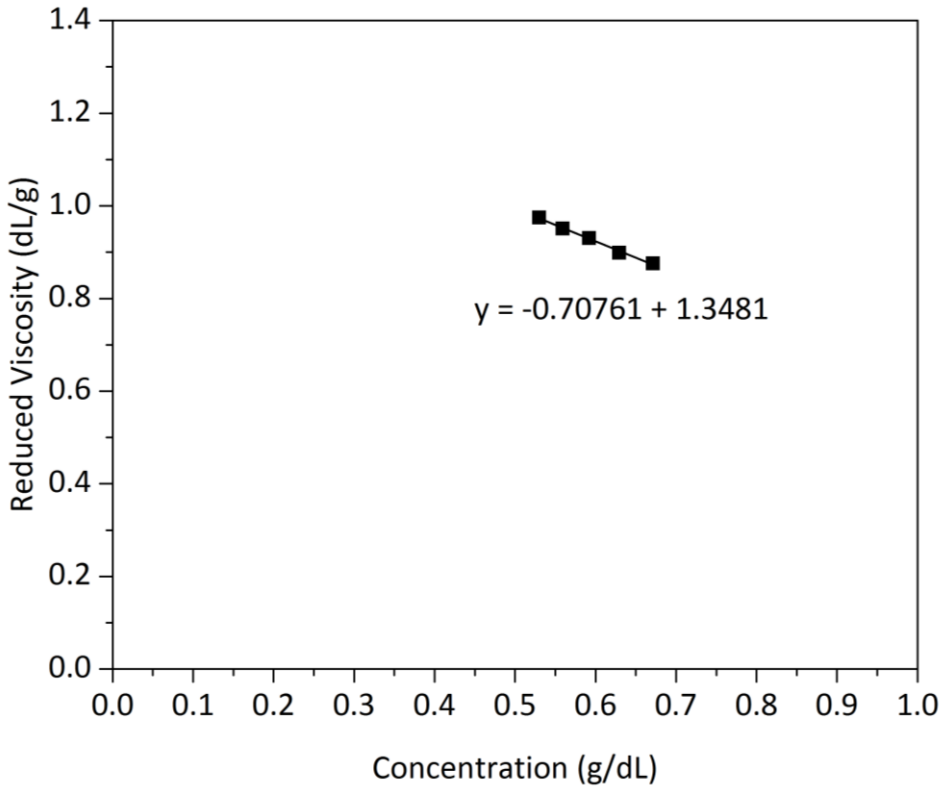

Figure 1: Reduced viscosity versus concentration of poly(methyl methacrylate-*co*-acrylic acid) polymer in tetrahydrofuran at 25°C

Calculation of Viscosity-Average Molecular Weight of Polymer

$$[\eta] = K\bar{M}_v^a$$

$$\text{where } [\eta] = 1.3481 \text{ dL/g}, K = 7.5 \times 10^{-5} \text{ dL/g and } a = 0.72$$

$$1.3481 = (7.5 \times 10^{-5})\bar{M}_v^{0.72}$$

$$\log 1.3481 = \log 7.5 \times 10^{-5} + 0.72 \log \bar{M}_v$$

$$\log \bar{M}_v = \frac{\log 1.3481 - \log(7.5 \times 10^{-5})}{0.72}$$

$$\log \bar{M}_v = 5.9092$$

$$\bar{M}_v = 5.9092 = 811430 \text{ g/mol}$$

LIST OF PUBLICATIONS

Lee, C.L., Goh, W.S., Chee, S.Y. and Yik, L.K., 2018. Augmentation of power conversion efficiency of amorphous silicon solar cell employing poly(methyl methacrylate-*co*-acrylic acid) nanospheres encapsulated with gold nanoparticles. *Journal of Materials Science*, 53(7), pp. 5183-5193.

Lee, C.L., Goh, W.S., Chee, S.Y. and Yik, L.K, 2017. Enhancement of light harvesting efficiency of silicon solar cell utilizing arrays of poly(methyl methacrylate-*co*-acrylic acid) nano-spheres and nano-spheres with embedded silver nano-particles. *Photonics and Nanostructures – Fundamentals and Applications*, 23, pp. 36-44.